

High Fidelity Monte Carlo Based Reactor Physics Calculations

Zur Erlangung des akademischen Grades

Doktor der Ingenieurwissenschaften (Dr.-Ing.)

der Fakultät für Maschinenbau
Karlsruher Institut für Technologie (KIT)

genehmigte

Dissertation

von

M. Sc. Aleksandar Stoyanov Ivanov

aus Sofia, Bulgarien

Hauptreferent:	Prof. Dr.-Ing. Robert Stieglitz Karlsruher Institut für Technologie
Korreferent:	Prof. Dr. Kostadin N. Ivanov The Pennsylvania State University
Tag der mündlichen Prüfung:	12 Februar, 2015

И ѿны ѻвцы ѿмамъ, ꙗже не сѣтъ ѿ двора сего̀, и тыѡ ми
подобаетъ привести: и гласъ мой о̀услышатъ, и вѣдетъ еди́но
стадо (и) еди́нъ па́стырь.

На моите родители Лиляна и Стоян.

*На светлата памет на моя свако
Стефан Димитров Чакъров.*

Contents

Acknowledgments	12
Abstract	14
List of Publications	17
1 Introduction	19
1.1 State of the art	19
1.2 Thesis objective	21
1.3 Organization of the Dissertation	24
2 The nuclear reactor core	28
3 Monte Carlo solution of the neutron transport equation	30
3.1 The collision density equations	30
3.2 Fission source convergence	36
3.3 Nonanalog Monte Carlo transport	38
3.4 Monte Carlo and deterministic transport	41
3.5 Boundary conditions	45
4 Temperature dependence of the nuclear cross sections	47
4.1 Temperature dependence of the single differential nuclear data	47
4.2 Thermal neutron scattering	53
4.3 Implementation of a new methodology for correcting the temperature dependence of the thermal scattering data.	58

5	The Wielandt acceleration method	64
5.1	Wielandt shift acceleration of the Monte Carlo power iteration	64
5.2	Testing the performance of the Wielandt method	68
6	Accelerated flux tallying in MCNP	76
6.1	Fission heat and flux estimators in MCNP	77
6.2	Data locality and bin structure optimization	78
6.3	Implementation in MCNP and performance testing	80
7	Implementation of the fission matrix technique in MCNP and higher order eigen-pair analysis	83
7.1	The fission matrix technique in Monte Carlo criticality calculations	83
7.2	Numerical analysis of sparse eigenproblems	85
7.3	Practical implementation and numerical computation of higher mode eigenstates	90
7.4	The Wielandt acceleration and its effect on the Monte Carlo power iteration . .	94
8	Reducing the variance of the Monte Carlo criticality calculations	97
8.1	The Global Variance Reduction Technique	98
8.2	The Uniform Fission Site method	101
8.3	Numerical performance of the variance reduction techniques	102
9	Coupled Monte Carlo - thermal hydraulics calculations	107
9.1	Fundamentals of the stochastic approximation method	107
9.2	The internal coupling between Monte Carlo transport and thermal hydraulics .	112
10	Application of the internal coupling scheme to the quarter core PWR UOX-MOX benchmark problem	116
10.1	Validation of the geometry modeling with the benchmark reference solutions .	116
10.2	Simulation of the PWR MOX-UO ₂ benchmark with the internal coupling MCNP - SUBCHANFLOW	122
11	Monte Carlo based depletion calculations	132
11.1	Fuel depletion calculations	133
11.2	Xenon buildup and oscillations	137
11.3	The coupling between MCNP and KORIGEN	140
11.4	Practical analysis of the stochastic implicit Euler method	142

11.5 Monte Carlo estimation of the equilibrium ^{135}Xe concentration	144
11.6 Numerical results	147
Conclusions and outlook	151
List of symbols	154
List of Figures	159
List of Tables	162

Acknowledgments

I am grateful to the many people whose help and support that have made this thesis possible. First and foremost, I would like to express my special appreciation and thanks to my advisors Prof. Dr.-Ing. Robert Stieglitz and Prof Dr. Kostadin Ivanov. Their continued support led me in the right direction.

I am especially grateful to my senior colleagues that have taken the time to teach me the ropes. I would like to thank Dr. Cornelis Broeders who has provided me with great support and advice throughout the later stage of my doctoral research. I also learned a lot from Prof. Dr. Eduard Hoogenboom, who was always willing to give me advice and answer my questions. I would like to thank my group leader at the KIT Dr. Victor Sanchez for providing the exciting working environment I had during my research at KIT.

My special thanks goes to the Steinbruch computing centre - SCC and the Jülich supercomputing centre - JSC . I would like to thank them for their support and for providing the supercomputing infrastructure needed to run my calculations.

I would like to thank the nuclear safety program at KIT for funding my doctoral research.

Finally I would like to thank my family for their love and support.

Declaration of Authorship

I, Aleksandar Stoyanov Ivanov, declare that the work presented in this thesis is my own. I hereby confirm that where I have consulted the published work of others, this is always clearly attributed, where I have quoted from the work of others, the source is always given. I declare that I observed the statutes of the Karlsruhe Institute of Technology (formerly University of Karlsruhe) to ensure good scientific practice in its current version.

Eidesstattliche Erklärung

Hiermit erkläre ich, Aleksandar Stoyanov Ivanov, dass ich die vorliegende Arbeit selbstständig angefertigt und keine anderen als die angegebenen Quellen und Hilfsmittel benutzt sowie die wörtlich und inhaltlich übernommenen Stellen als solche kenntlich gemacht und die Satzung des Karlsruher Instituts für Technologie (vormals Universität Karlsruhe (TH)) zur Sicherung guter wissenschaftlicher Praxis in der jeweils gültigen Fassung beachtet habe.

Date:

Signed:

Abstract

The complicated heterogeneous nuclear reactor core geometries and fuel loading patterns of the future nuclear reactors pose serious challenges to the currently used standard computational tools. In the recent years there has been an increasing level of interest in the use of Monte Carlo methods for performing high accuracy three dimensional nuclear reactor calculations. As such they can provide reference solutions for the deterministic tools. The Monte Carlo method provides the most accurate solution of the neutron transport problem. The ability to efficiently utilize high performance computer architectures and the precise physics models used by Monte Carlo codes, enable the accurate simulation of real reactor problems. In reactor analysis calculations, nuclear and thermal-hydraulic performance is highly dependent on local material temperatures throughout the reactor core. In order to achieve accurate results, this temperature dependence should be included in nuclear calculations for reactor analysis and design. Therefore, the main goal is the ability to perform full-core Monte Carlo reactor calculations taking into account the distribution of temperature and density. Since the fuel composition within a reactor core changes with time due to irradiation, a complementary goal is the incorporation of depletion capability in the Monte Carlo solver.

This thesis presents the research and development of Monte Carlo methods for finding eigenvectors and eigenvalues of the stationary neutron transport equation, taking into account the local values of the temperature, density and fuel depletion. The focus is on both improving the calculation algorithm and increasing the accuracy of the physics models. Therefore, special attention is paid to improving the eigenvalue solution, the associated variance of the Monte Carlo estimates, the temperature dependence of the nuclear data and the stability of the depletion calculations.

The primary goal of this work is to develop Monte Carlo based multi-physics capability for real large scale problems, such as a full commercial reactor core at single fuel pin cell resolution. The superiority of the newly developed methods is proven and their accuracy validated by comparing them to the existing methodologies for performing Monte Carlo transport calculations and by simulating international benchmark exercises.

Kurzfassung

Die komplizierten heterogenen Reaktor-Geometrien und Kernbeladungen von zukünftigen Kernreaktoren stellen eine große Herausforderungen an die verwendeten Rechenmethoden dar. In den letzten Jahren gibt es ein zunehmendes Interesse an der Verwendung von Monte-Carlo-Verfahren für die Durchführung von sehr genauen dreidimensionalen Berechnungen von Kernreaktoren. Diese können als Referenzlösungen für die deterministischen Verfahren eingesetzt werden. Die Monte-Carlo-Methode kann die genaueste Lösung des Neutronentransportproblem anbieten. Die Kombination, effiziente Hochleistungsrechner-Architekturen und genaue physikalischen Modelle mit Monte-Carlo-Codes zu nutzen, ermöglicht genaue Simulation von reellen Reaktorproblemen. In Reaktor-Analyseberechnungen hängen nukleare und thermisch-hydraulische Leistung stark von lokalen Material-Temperaturen und -Dichten im gesamten Reaktorkern ab. Um genaue Ergebnisse zu erzielen, sollte diese Temperatur- und Dichte-Abhängigkeit in Kernberechnungen für Reaktor-Analyse und Auslegung enthalten sein. Daher ist das Hauptziel die Fähigkeit, Vollkern Monte-Carlo Reaktor-Berechnungen unter Berücksichtigung der Temperatur- und der Dichteverteilung bereitzustellen. Da sich die Brennstoffzusammensetzung innerhalb eines Reaktorkerns mit der Zeit infolge der Bestrahlung verändert, ist das komplementäre Ziel eine Abbrand-Option in dem Monte-Carlo-Löser einzuführen.

Diese Arbeit stellt die Forschung und Entwicklung von Monte-Carlo-Methoden zum Auffinden von Eigenvektoren und Eigenwerte der stationären Neutronentransportgleichung, unter Berücksichtigung der lokalen Werte der Temperatur, Dichte und Brennstoffzusammensetzung dar. Der Schwerpunkt liegt sowohl auf der Verbesserung von Berechnungsalgorithmen, als auch auf der Erhöhung der Genauigkeit der Physik-Modelle. Deswegen wird besonders auf die Verbesserung der Eigenwertlösung, auf die zugehörige Varianz der Monte-Carlo-Schätzungen, auf die Temperaturabhängigkeit der Kerndaten und auf die Stabilität der Abbrand-Berechnungen geachtet.

Das primäre Ziel dieser Arbeit ist die auf Monte-Carlo basierte Multi-Physik-Fähigkeit für reelle große Probleme, wie z.B. ein voller Leistungsreaktorkern bei einzelner Auflösung der

Brennstabzelle zu entwickeln. Die Überlegenheit der neu entwickelten Methode wird gezeigt und die Genauigkeit durch Vergleiche mit bestehenden Methoden zur Durchführung von Monte-Carlo-Transportberechnungen und durch Simulation von internationalen Benchmark-Untersuchungen validiert.

List of Publications

[1] Large-Scale Monte Carlo Neutron Transport Calculations with Thermal Hydraulic Feedback, A.Ivanov, V.Sanchez, R.Stieglitz, K.Ivanov, Accepted for publication, Multi-Physics Modelling of LWR Static and Transient Behaviour, *Annals of Nuclear Energy*, **84** , pp. 204-219, (2015)

[2] High-fidelity coupled Monte Carlo neutron transport and thermal-hydraulic simulations using Serpent 2/SUBCHANFLOW, Miriam Däubler, A. Ivanov, B. L. Sjenitzer, V. Sanchez, R. Stieglitz, R. Macian-Juan, *Annals of Nuclear Energy*, **83** , pp. 352-375, (2014)

[3] Internal multi-scale multi-physics coupled system for high fidelity simulation of light water reactors, A.Ivanov, V.Sanchez, R.Stieglitz, K.Ivanov, *Annals of Nuclear Energy*, **66** , pp. 104-112, (2013)

[4] High fidelity simulation of conventional and innovative LWR with the coupled Monte-Carlo thermal-hydraulic system MCNP-SUBCHANFLOW, A.Ivanov, V.Sanchez, R.Stieglitz, K.Ivanov, *Nuclear Engineering and Design*, **262** , pp. 264-275, (2013)

[5] Maximum Efficiency in Massively Parallel Execution of Monte Carlo Criticality Calculations, J.E. Hoogenboom, A. Ivanov, V. Sanchez, *Proc. Int. Conf. American Nuclear Society - Joint International Conference on Mathematics and Computation (M&C), Supercomputing in Nuclear Applications (SNA) and the Monte Carlo (MC) Method, Nashville TN, USA*, (2015)

- [6] Variance Reduction in High Resolution Coupled Monte Carlo - Thermal-Hydraulics Calculations, *Proc. Int. Conf. American Nuclear Society - Joint International Conference on Mathematics and Computation (M&C), Supercomputing in Nuclear Applications (SNA) and the Monte Carlo (MC) Method*, Special session on Monte Carlo Criticality Calculations with Thermo-Hydraulic Feedback, Nashville TN, USA, (2015)
- [7] Optimization of a coupling scheme between MCNP5 and SUBCHANFLOW for high fidelity modeling of LWR reactors, A. Ivanov, V. Sanchez, K. Ivanov, *Proc. Int. Conf. PHYSOR 2012, Knoxville, Tennessee, USA*, (2012)
- [8] Large-Scale Monte Carlo calculations with thermal-hydraulic feedback, A. Ivanov, V. Sanchez, R. Stieglitz, *Proc. Int. Conf. PHYSOR 2014, Kyoto, Japan*, (2014)
- [9] High-Fidelity Coupled Monte-Carlo/Thermal-Hydraulics Calculations, A. Ivanov, V. Sanchez, K. Ivanov, *Proc. Int. Conf. MC+SNA Paris, France*, (2013)
- [10] Single pin BWR Benchmark Problem for Coupled Monte Carlo - Thermal Hydraulics Analysis, A. Ivanov, V. Sanchez, K. Ivanov, J.E. Hoogenboom, *Proc. Int. Conf. PHYSOR 2012, Knoxville, Tennessee, USA*, (2012)

1.1 State of the art

The computational tools used to perform neutronics simulations are divided into two major branches, namely deterministic and stochastic - Monte Carlo tools. Deterministic methods determine the average behaviour of particles in a system by numerically solving the Boltzmann transport equation. This approach requires discretising the equations governing the neutron transport in all independent variables. The integro-differential neutron transport equation is converted into a system of algebraic equations that are used to approximate the solution functions. In contrast, the Monte Carlo method is used to simulate the statistical process of neutron and charged particle interaction with the medium they travel in, almost without approximations. The events that comprise the process are simulated by following the histories of individual particles. Individual events are statistically sampled to describe the total phenomenon, where the particle distributions become better known with increasing the number of simulated histories. The main obstacle to the establishment of the Monte Carlo tools as the standard for reactor physics calculations is their computational expense.

Modern computing has made it possible to obtain high-fidelity solutions of extremely large scale reactor simulations. The approximations for the energy, angle and spatial dependence of the neutron flux are gradually lifted and tools capable of simulating the neutron transport problem by considering a detailed description of the phase space, are being developed worldwide.

In the case of deterministic tools, diffusion theory is being replaced by simplified transport (SP_3) [3],[4], [5]. Recently, deterministic tools capable of running three dimensional reactor core neutron transport calculations have been developed [6], [7]. Careful analysis of the results, however, reveals some significant approximations. For instance, running three dimensional neutrons transport is computationally prohibitive even with today's high performance computers. Therefore, the transport solution is run only in the radial direction and lower order solution is used for the axial direction. Developing deterministic tools capable of efficiently utilizing the modern high performance computing architectures is a very challenging task due

to the solution mechanism of deterministic tools. Deterministic codes are usually sequential and even codes using significant approximations such as SP_3 take days to complete, if high resolution solutions are demanded. Deterministic tools also require significant amount of computer memory in order to store the data associated with the discretised computational domain.

The deficiencies associated with the deterministic tools and the increased capabilities offered by modern high performance computing architectures, have revived the interest in Monte Carlo methods. Contrary to deterministic codes, Monte Carlo codes can efficiently scale to hundreds of thousands of cores [8], [9]. The computational efficiency of Monte Carlo codes and their ability to use continuous representation of the phase space makes them natural candidates to meet the demand for high precision reactor physics solutions.

Nowadays, Monte Carlo codes are well suited for calculation of large reactor core problems, but mainly for integral quantities, such as the eigenvalue. Estimating local quantities like the fission heat deposition poses serious challenges, associated with the large statistical variances of the local Monte Carlo estimates. This is mainly due to the lack of variance reduction techniques specially designed to improve the efficiency of the eigenvalue calculations. In particular, the general purpose **MCNP** code used for this analysis completely lacks adequate variance reduction techniques to be used in the eigenvalue calculation (criticality) mode. Variance reduction techniques dedicated to this task have been implemented in [10], [11], unfortunately due to distribution restrictions issues, the codes are not publicly available.

Running full core criticality calculations poses serious challenges due to the poor convergence of the eigenvalue calculation. No solution of this problem is given in the available computer codes. Miscalculating the convergence of the eigenvalue calculation results in wrong Monte Carlo estimates and serves as significant barrier on the path towards large scale reactor calculations. This deficiency strongly affects the estimation of local quantities such as fission heat deposition and neutron flux.

In general, Monte Carlo codes are used to calculate the steady state spatial distribution of neutrons in eigenvalue and fixed source problems. These calculations are highly dependent on local material temperatures throughout the reactor core. The distribution of the temperature in the core is determined by the reactor operating conditions. In contrast to deterministic codes, which are usually linked to thermal hydraulic modules, in Monte Carlo calculations those conditions are approximated by homogeneous distributions. This is a rather strong simplification and departure from the physical reality. In the recent years, there has been a significant effort to introduce thermal hydraulic feedback to Monte Carlo criticality calculations. Due to the difficulties related to the temperature dependence of the nuclear data, the large variance of the Monte Carlo estimates needed as boundary conditions for the thermal hydraulic calculation and the lack of efficient thermal hydraulic handling methods, most of this solutions use simplified thermal hydraulic models. In particular, either coarse meshes are used for estimating the power density [12], [13] or are applied to small size problems consisting of individual fuel pins [14]. A very advanced method for incorporating the varying distribution of temperature was implemented in the the **MC21** code [15]. Moreover, little to

no work was done in clarifying measures needed for correcting the temperature dependence of the nuclear data that describes the scattering of neutrons from water molecules.

Monte Carlo codes have been linked to depletion modules [16], [17], [18], [19], [20], [21] and [22]. The inclusion of depletion capabilities, introduces the possibility to compute the changes in the fuel isotopic content caused by the fuel irradiation inside the core. The important issue of rapid buildup of fission isotopes having large thermal absorption cross sections, such as ^{135}Xe is not properly addressed in the available Monte Carlo codes. The strong coupling between the neutron flux distribution and the local ^{135}Xe concentrations induces instabilities and results in unphysical results for the Monte Carlo depletion calculations.

1.2 Thesis objective

Having in mind the deficiencies of the deterministic codes associated with the approximative treatment of the energy, the space, the angular dependences and their inability to run full three dimensional transport solutions Monte Carlo codes are the most natural candidates to meet the demand for high accurate reactor physics calculations. As yet, none of the available Monte Carlo transport codes are able to perform reactor core simulations taking into account local distributions of density and temperatures and provide solutions having single fuel pin resolution in both the neutronic and thermal hydraulic domains. Therefore, the overall goal of the thesis is to perform accurate Monte Carlo based calculations using precise physics and geometry models. This requires solving a complex problem that links numerics, physics and high performance computing. To achieve this objective, various methods for improving both the efficiency of the computational algorithm, the underlying variance of the Monte Carlo estimates and the accuracy of the physics modeling are needed.

Even before introducing the thermal hydraulic feedback one has to significantly improve the efficiency of the standard Monte Carlo based computational methodology used for running criticality calculations. Running detailed transport calculations and estimating local fission heat deposition within acceptable statistical accuracy in large scale reactor geometries, even without taking into account the thermal hydraulic feedback, is a complicated task. In addition, due to the poor performance of the Monte Carlo criticality calculation when applied to full core problems, the local values of the fission heat deposition tend to be statistically biased.

Due to the small mean free path of the neutrons in a typical light water reactor core, the neutrons born in a particular assembly are likely to end their path, by either absorption or fission, in the same assembly or its nearest neighbouring assemblies. Therefore, remote parts of the core geometry are decoupled from each other and one speaks of a loosely coupled transport problem. Monte Carlo transport solvers rely on a modified version of the power iteration method. It simulates batches of individual neutrons to obtain global distributions of flux and fission rate density throughout the problem. The fission sites sampled in a particular batch are used as starting fission sites for the neutrons in the next batch. The neutron batches, closely resemble successive application of the transport operator that is required for the power iteration solution of the eigenvalue problem. The fundamental neutron source

distribution is unknown at the beginning of the calculation and one starts the calculation with a pre-defined initial guess. A number of power iterations are needed to converge the fission source distribution. Therefore, Monte Carlo codes allow for some number of initial batches to be disregarded at the beginning of the job. The number of initial cycles strongly depends and increases with increasing the problem complexity. The decoupling of the spatial domains slows down the convergence of the power iteration, since it takes large number of successive batches before local changes in the fission heat deposition have their effect on the overall source distribution. Miscalculating the convergence of the fission source would allow the contribution from the initial batches to contaminate the final results. Taking into account that large scale geometries have complex material compositions will be discussed, this thesis aims at developing an improved method for performing the Monte Carlo power calculation.

Since the fission heat deposition is used as a boundary condition for the thermal hydraulic calculations, it has to be estimated by the Monte Carlo code within acceptable variance, usually less than one percent. Another major issue is ensuring that all the quantities of interest have acceptable statistical uncertainties. In principle, brute force increasing of the number of simulated particle histories can improve the statistical uncertainties. This strategy is inefficient, since it affects mainly the regions where the particle abundance is high. Therefore, a method capable of not only reducing, but also homogenizing the statistical uncertainties for different regions of the computational domain has been developed. The criticality calculation is to be modified to run nonanalog transport. Nonanalog transport increases the occurrence frequency of statistically rare events, thereby ensuring reliable sampling. To keep the score for the Monte Carlo estimates such as the neutron flux or the fission heat deposition unbiased the score weight has to be properly defined. Moreover the variance reduction technique to be developed has to have very small footprint on the overall computing time.

To make the criticality calculation accurate and minimize approximations, the computational domain has to be modeled with minimal geometry approximations and taking into account the local distribution of temperature and density. Varying temperatures on their side require the evaluation of the nuclear data at the corresponding temperature of interest. This is valid for the nuclear data describing both reaction rates and the inelastic scattering of thermal neutrons inside the moderator.

A steady state of the system of interest is to be computed, thus a coupling between the Monte Carlo and the thermal hydraulic calculations has to be developed. The coupled system should be able to reach convergence and a reliable stable relaxation scheme is needed. Since the fission heat distribution is estimated with a certain statistical uncertainty, it experiences random fluctuation within its confidence interval. This behaviour poses significant convergence challenges. To overcome this issue an accelerating scheme taking into account the stochastic nature of the simulation is needed. Each iteration of the coupled system involves a criticality calculation, that estimates the fission heat deposition, and an updated temperature and density distributions. Therefore, it suffers from all the deficiencies described in this paragraph, and requires their improvement as input.

Taking into account the change of isotopic compositions introduces another level of com-

plexity. The strong feedback of the fission poison buildup on the neutron flux distribution introduces another level of complexity. The local fuel compositions need to be supplied as a function of irradiation time and the stability of the calculation has to be ensured. Since the fluxes suffer statistical fluctuations, that translates to artificial power changes leading to unphysical 'feedback' effects. The large thermal absorption cross section of ^{135}Xe has a significant impact on the flux distribution and the reactivity change and provides strong feedback. This makes three dimensional Monte Carlo based depletion calculations unstable. Currently, depletion systems are mainly applied to two dimensional problems. In this case, the spacial coupling between the ^{135}Xe feedback concentration and the neutron flux can be dampened by either using very fine time discretisation or by applying semi implicit methods. These methods were proven unstable [23]. Moreover, running very small time steps is constitutionally prohibitive, since it increases the number of time three dimensional Monte Carlo transport is run. Therefore ensuring the stability of the Monte Carlo depletion system serves as prerequisite for performing three dimensional depletion calculations and new methods are needed to tackle the problem.

1.3 Organization of the Dissertation

To realise the overall goal of the thesis of performing high accurate and computationally efficient neutron transport criticality calculations taking into account the local thermal hydraulic and the fuel isotope distributions, various improvements and new modeling features were introduced in **MCNP**. They aim at both improving the computational efficiency of the Monte Carlo transport part of the solution and at increasing the accuracy of the physics models used by the code.

It is also important to both verify the newly implemented methods and to prove their superiority to the existing methods. Therefore, special attention was dedicated to code-to-code comparison and validation using international benchmark exercises.

Chapters 1 and 2 are introductory chapters representing the thesis objectives and organization as well as a general description of a nuclear pressurized reactor core.

Chapter 3 presents a theoretical introduction to the Monte Carlo transport theory and the fundamental concepts needed for understanding the various developments presented in this thesis. The Monte Carlo solution of the Boltzmann transport equation is described and the collision density equations are derived. The concept of tally estimators is introduced and their derivation from the collision equations are presented. The method of successive generations used for estimating the fundamental eigenpair of the transport operator is introduced. The convergence of the method is discussed and the concept of dominance ratio - the quotient of the two largest eigenvalues of the stationary transport operator is introduced. The stochastic method of simulating the neutron transport problem is compared to deterministic transport and their differences are discussed. The Shannon entropy method for monitoring fission source convergence is described. The chapter also explains the boundary conditions used and their role at speeding up the calculation and reducing the dominance ratio of the problem.

Since the thermal hydraulic feedback is introduced in the neutron transport process via the nuclear cross sections, Chapter 4 treats the temperature dependence of both the single and double differential nuclear data. Theoretical explanation of the Doppler effect is given. In addition, the theoretical description of incoherent inelastic scattering from bound hydrogen is presented. In this chapter the method of pseudo material mixing is introduced and its accuracy proven. The developments done in this thesis for correcting the temperature dependence of the double differential data are presented. The development and implementation of novel on-the-fly technique for treating the effect of varying moderator temperature on the thermal scattering data is presented and its results validated. The newly implemented methodologies for correcting the temperature dependence of both the double and single differential nuclear data are verified by comparison with exact temperature processed nuclear data. The techniques described in this chapter are later on used for introducing the thermal hydraulic feedback to the neutron transport process.

The main goal of this thesis is to run full high resolution full core calculations, therefore, Chapter 5 discusses the Wielandt shift method as a tool for improving the criticality calculation. The standard method, known from matrix calculations, is implemented in the Monte

Carlo code by modifying the transport operator. The efficiency of the method and its effect on the local reaction rate estimates is investigated. It is shown in practice, that the modified by the Wielandt shift transport operator converges rapidly to the fundamental eigenvalue of the system. The consistency of the method is proven by comparing the eigenvalues and eigenvectors to reference values obtained by analog simulation. The effect of shifting the spectrum of the eigenvalues on the relative error distribution and tally symmetry is investigated. By applying the Wielandt shift method a general tool for improving the criticality calculation was developed.

Since tallying the local distribution of the power significantly slows down the neutronic calculation, Chapter 6 introduces the improvement of methodology used for tallying the Monte Carlo estimates. It is shown, that by combining effective utilization of optimized coding and improved spatial bin storage based on Morton ordering, it is possible to significantly speed up the flux and reaction rate estimation. The newly developed techniques for accelerating the tallying are applied later in this thesis to efficiently compute the fission heat deposition. Since the newly implemented methodology represents an improved computational algorithm estimating the same quantity of interest it must deliver identical results when compared to the standard tallying procedures. Therefore, the consistency of the new algorithm is verified by comparing it to the standard **MCNP** code.

To investigate the efficiency of the newly implemented power iteration techniques, the implementation of additional computational techniques is needed. Chapter 7 treats the implementation of the Fission matrix technique used as a tool for investigating the efficiency of the Wielandt shift method. Theoretical description of both the Fission Matrix technique and the computational methods used for estimating the eigenvalues of large sparse matrices are described. The advanced bin storage technique developed for improving the tallying, is used to ensure compact storage of the matrix elements. The higher mode eigenvalues of the Fission matrix are used to provide direct proof that the the Wieland shift Method reduces the dominance ratio of the system and to motivate the implementation of the Wieland method. The correctness of the implementation is verified by comparing the fundamental mode eigenvalues obtained by the standard Monte Carlo power iteration and the fundamental mode eigenvalues of the fission matrix. Using the advanced bin storage techniques it was possible for the first time to compute eigenvalues of the fission matrix at pin by pin resolution. Another unique result was the computation of the higher mode eigenvalues taking into account the thermal hydraulic boundary condition. This allowed the analysis of the the convergence of the transport operator when applied to a real nuclear reactor core configuration.

Since the fission heat deposition is used as a boundary condition for the coupled Monte Carlo - thermal hydraulic calculation, in Chapter 8 the methods used for improving the variance of the Monte Carlo reaction rates are demonstrated. The newly implemented Uniform Fission Site method and the Global Variance Reduction technique are implemented and their efficiency is compared. By analysing of the figure of merit the superiority of the Uniform Fission Site method is proven.

To overcome the deficiencies of the methods used for introducing the thermal hydraulic feed-

back, novel methodology for the introduction of local temperature and densities distribution is developed. Chapter 9 describes the new methodology for running transport calculations with thermal hydraulic feedback. This chapter relies on all the developments done in the previous chapters. The newly developed internal coupling scheme for on-the-fly introduction of the thermal hydraulic feedback is presented. It integrates the methods developed for treating the temperature dependence of the nuclear data and allows to define a three dimensional distribution of temperature and density. The novel methodology is proven superior to the standard method of introducing the feedback by explicit geometry splitting. The stochastic approximation technique is introduced and its application as convergence acceleration tool is demonstrated.

Chapter 10 illustrates the practical application of the novel coupling scheme to the PWR UOX-MOX benchmark. Using the novel strategy of coupling Monte Carlo and thermal hydraulic and the improved criticality calculation it was possible for the first time to run coupled PWR core problem at unprecedented resolution. To prove the consistency of the methodology, comparison to reference solutions is needed. The verification of the results is done for both three and two dimensional cases. The two dimensional model is used to verify the geometry model and to prove the consistency of the newly implemented techniques for accelerated fission heat distribution tallying. The subsequent three dimensional problem takes into account the thermal hydraulic feedback. It is used to verify the newly implemented methods for on the fly feedback definition, the improved power iteration and the newly implemented variance reduction techniques.

Chapter 11 discusses the development and integration of depletion capabilities into the **MCNP** code. The internal coupling scheme is extended further to take into account fuel depletion. For this purpose a coupled code system between **MCNP** and the in-house depletion code **KORIGEN** is developed. The theoretical foundations of Monte Carlo based depletion calculations are presented. The xenon feedback effect is discussed and the stability of the depletion calculations is studied. The existing methodologies for performing three dimensional Monte Carlo based depletion calculations are analysed. Based on their deficiencies optimal methodology for stable depletion calculations is selected. The state of the art technique for direct estimation of the xenon production using the Monte Carlo code is implemented in **MCNP**. This technique imposes the correct xenon distribution and dampens the divergence. Since the ^{135}Xe concentration is estimated using high resolution neutron transport, it ensures that the isotope having the largest impact on the flux and the power distribution is reliably computed. The newly implemented scheme utilizes efficiently the inactive Monte Carlo cycles used for converting the fission source and computes the equilibrium ^{135}Xe concentration within a single Monte Carlo transport calculation. Due to the fact that the equilibrium ^{135}Xe concentration is computed within a single run, the calculation runs much faster than the currently established strategies for stabilizing the depletion calculation, where multiple runs of the Monte Carlo transport code are needed. Since the ^{135}Xe concentration is computed as a function of the neutron flux, instabilities are impossible to occur, proving the superiority of the newly implemented methodology. The methodology is validated by comparing it to explicit depletion computations using fine step time discretisation. The strategy

to compute the ^{135}Xe concentration directly as a function of the neutron flux, paves the way to large scale three dimensional depletion calculations by significantly reducing the computational expense of the depletion calculation.

The nuclear reactor core

There are many different types of power reactors. What is common to all of them is that they produce thermal energy that can be used for its own sake or converted into mechanical energy and ultimately, in the vast majority of cases, into electrical energy. The most common type of nuclear reactors are the pressurized water reactors (PWR) and the boiling water reactors (BWR). In these reactors, the fission of heavy atomic nuclei, produces heat that is transferred to a fluid which acts as a coolant. During the fission process, the nuclear binding energy is released and this first becomes noticeable as the kinetic energy of the fission products generated and that of the neutrons being released. Following the fission reaction, the fission products deposit their kinetic energy locally in the fuel and it is transformed into heat. In this thesis both the neutronic and the thermal hydraulic calculations are applied to a pressurized water reactor problem. Pressurized Water Reactor are characterised by a high pressure coolant system in order to prevent boiling.

The primary attention of this work is dedicated to a PWR reactor core. The reactor core consists of fuel assemblies in a square lattice arrangement. Each fuel assembly contains a lattice of pins, typically 17 times 17 array, containing fuel clad in Zircaloy tubes. The core power level is controlled by control rods, containing neutron absorbing material.

There are a large number of vessel internal structures to support the core, direct the coolant flow etc. see fig. 2.1. The reactor is cooled by light water that circulates through the core. The coolant temperature is typically 298 °C at the inlet to the reactor core. The temperature rise across the core region is about 28 °C. PWRs typically have four coolant loops. The flow rate through each loop is about four tonnes per second.

The reactor vessel itself is a steel cylinder with a domed upper lower head. The cylindrical section is about 4.5 meters. Attached to the pressure vessel are four inlet outlet nozzles. These nozzles are symmetrically arranged around the vessel and connect the vessel to the hot and cold legs of the primary circuit. The upper head is removable to insert and extract the fuel assemblies.

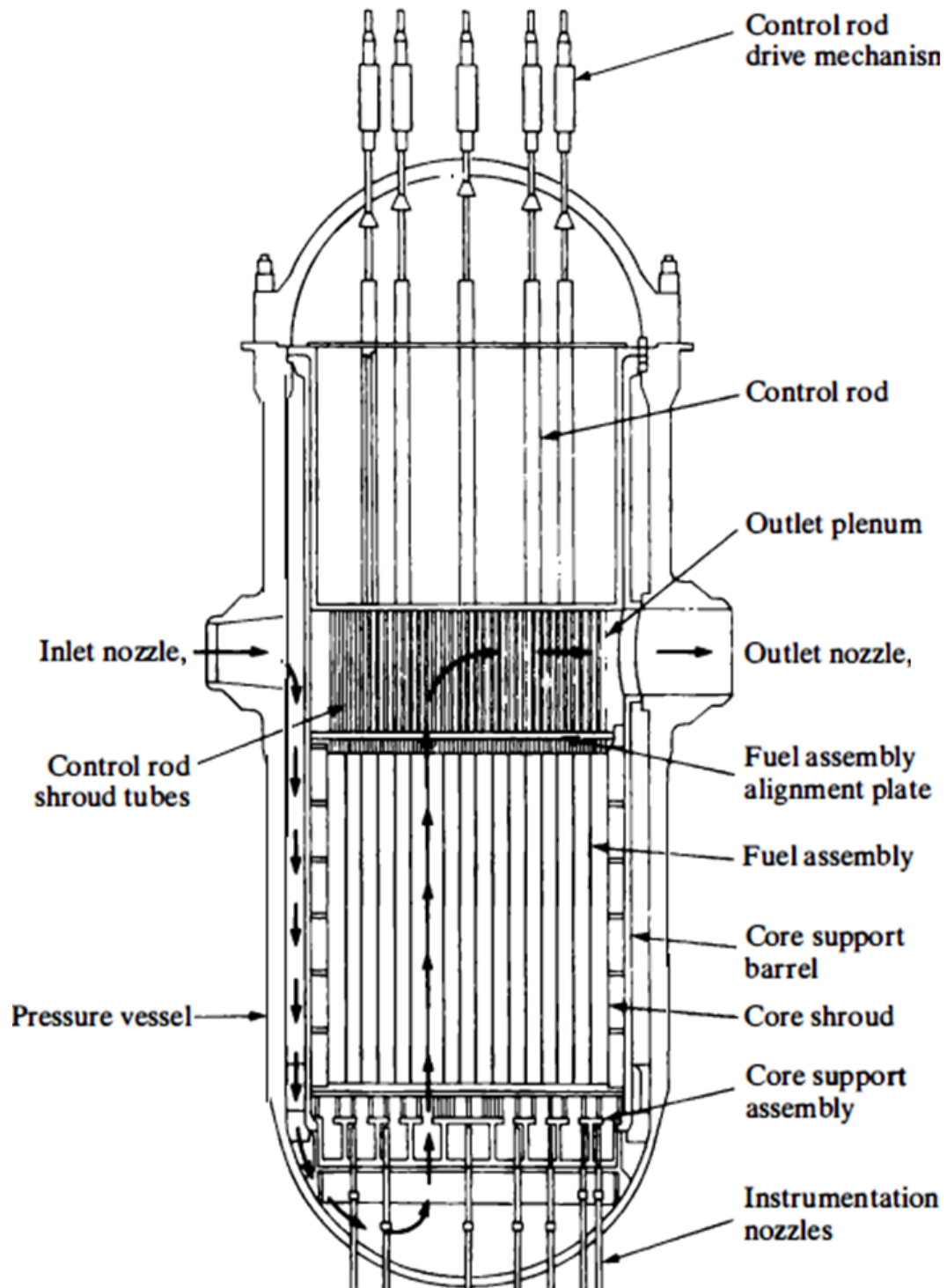


Figure 2.1: Pressurized water reactor core.

source: J.R. Lamarsh and A. J. Baratta "Introduction to nuclear engineering".

Monte Carlo solution of the neutron transport equation

3.1 The collision density equations

The general form of the stationary Boltzmann transport equation is given by (3.1)

$$\begin{aligned} & \left(\hat{\Omega} \cdot \nabla + \Sigma_t(\mathbf{r}, E) \right) \Psi(\mathbf{r}, E, \hat{\Omega}) = \\ & = \int_0^\infty \int_{4\pi} \Sigma_s(\mathbf{r}, \hat{\Omega} \cdot \hat{\Omega}', E' \rightarrow E) \Psi(\mathbf{r}, E', \hat{\Omega}') dE' d\hat{\Omega}' + S(\mathbf{r}, E, \hat{\Omega}). \end{aligned} \quad (3.1)$$

The equation gives the balance of neutrons entering and leaving a certain phase space volume $V_S = \Delta \mathbf{r} \Delta \hat{\Omega} \Delta E$. The $\Psi(\mathbf{r}, E, \hat{\Omega})$ representing the total track length of all neutrons in V_S per unit of phase space. The term $\hat{\Omega} \cdot \nabla$ is the leakage of the neutrons from $\Delta \hat{\Omega} \Delta E$ and $\Sigma_t \Psi(\mathbf{r}, E, \hat{\Omega})$ gives the total reaction rate. The right hand side of (3.1) gives the number of neutrons entering V_S after scattering or after being emitted from the source $S(\mathbf{r}, E, \hat{\Omega})$.

As given this is an integro-differential equation unsuitable for direct use in the Monte Carlo simulation. This equation can be written in a more suitable integral form. However, instead of working with the flux equation, the strategy given in [24] will be followed by defining an integral equations for the collision densities. Define the expected number of particles coming out of a collision in a certain volume element $d\mathbf{r}$ around \mathbf{r} and having energy and direction within $E + dE, \hat{\Omega} + d\hat{\Omega}$ by (3.2)

$$\chi(\mathbf{r}, \hat{\Omega}, E) d\mathbf{r} d\hat{\Omega} dE. \quad (3.2)$$

The counterpart of (3.2), denoting the particles entering a collision in the volume element $d\mathbf{r}$ around \mathbf{r} and having energy and direction within $E + dE$ and $\hat{\Omega} + d\hat{\Omega}$ by (3.3)

$$\xi(\mathbf{r}, \hat{\Omega}, E) d\mathbf{r} d\hat{\Omega} dE. \quad (3.3)$$

For brevity apply the convention [24] and denote the coordinates in the phase space by a single letter (3.4)

$$\mathbf{P} = (\mathbf{r}, \hat{\Omega}, dE). \quad (3.4)$$

For defining the equation governing the behavior of the collision densities, define the probability for a particle leaving a collision at \mathbf{r}' to have its next collision at \mathbf{r} . This quantity is the transport kernel given by (3.5)

$$T(\mathbf{r}' \rightarrow \mathbf{r} | \hat{\Omega}, E) = \Sigma_t(\mathbf{r}, E) \exp \left\{ - \int_0^s \Sigma_t(\mathbf{r} - s\hat{\Omega}, E) ds \right\} \frac{\delta(\hat{\Omega} - \hat{\mathbf{s}})}{s^2} \quad (3.5)$$

$$\mathbf{s} = \mathbf{r} - \mathbf{r}'.$$

This quantity relates directly to the integral transport equation and contains the expected result, that the probability of an interaction is proportional to the total cross section at that point $\Sigma_t(\mathbf{r}, E)$.

The second quantity to be defined is the collision kernel $C(\hat{\Omega} \cdot \hat{\Omega}', E' \rightarrow E | \mathbf{r})$ determining the number of particles coming from a collision at \mathbf{r} and having energy and direction within $E + dE$ and $\Omega + d\Omega$ by (3.6)

$$C(\hat{\Omega} \cdot \hat{\Omega}', E' \rightarrow E | \mathbf{r}) = \frac{\sum_{i=1}^N \sum_{j=1}^R v_{i,j} \Sigma_{i,j}(\mathbf{r}, \hat{\Omega} \cdot \hat{\Omega}', E' \rightarrow E)}{\Sigma_t(\mathbf{r}, E')}, \quad (3.6)$$

where N is the number of isotopes and R is the number of possible reactions. $v_{i,j}$ denotes the number of outgoing particles and $\Sigma_{i,j}$ is the differential cross section for a particular reaction.

Having defined the transport and the collision kernels, the governing equations can be defined. Particles with certain direction and energy are either emitted from the source or are born after a collision. Therefore, the outgoing collision density satisfies the following equation (3.7)

$$\chi(\mathbf{r}, \mathbf{E}) = Q(\mathbf{r}, \mathbf{E}) + \int d\mathbf{E}' C(\mathbf{E}' \rightarrow \mathbf{E} | \mathbf{r}) \xi(\mathbf{r}, \mathbf{E}'), \quad (3.7)$$

where $Q(\mathbf{r}, \mathbf{E})$ is the source term emitting particles having \mathbf{E} . In the above equation, the fact that both the energy and the angle are usually changed after collision is used. In most of the cases, they are also not independent [24]. Therefore, a simplified notation is introduced $\mathbf{E} = (E, \hat{\Omega})$. The same can be achieved by introducing the vector velocity \mathbf{v} .

Particles born at \mathbf{r}' can enter a subsequent collision at \mathbf{r} if they have the proper direction and energy. Using the definition of the transport kernel, (3.5) the governing equation of the ingoing collision density is given by (3.8)

$$\xi(\mathbf{r}, \mathbf{E}) = \int d\mathbf{r}' T(\mathbf{r}' \rightarrow \mathbf{r} | \mathbf{E}) \chi(\mathbf{r}', \mathbf{E}) \quad (3.8)$$

In principle, by substitution, equations (3.8) and (3.7) can be reduced to a single equation. Nevertheless keeping the equations separate provides a more simple way of explaining the physical properties of the computation.

The solution of the Fredholm integral equations for the collision and the emission densities is in the form of von Neumann series. Therefore, both collision densities defined above can be expanded in series (3.9)

$$\begin{aligned} \chi(P) &= \sum_{k=1}^N \chi_k(P) \\ \xi(P) &= \sum_{k=1}^N \xi_k(P). \end{aligned} \quad (3.9)$$

The separate terms of the von Neumann expansion can be recursively generated using (3.7) and (3.8)

$$\begin{aligned} \chi_0(\mathbf{r}, \mathbf{E}) &= Q(\mathbf{r}, \mathbf{E}) \\ \xi_0(\mathbf{r}, \mathbf{E}) &= \int d\mathbf{r}' T(\mathbf{r}' \rightarrow \mathbf{r} | \mathbf{E}) \chi_0(\mathbf{r}', \mathbf{E}) \\ \chi_{i+1}(\mathbf{r}, \mathbf{E}) &= Q(\mathbf{r}, \mathbf{E}) + \int d\mathbf{E}' C(\mathbf{E}' \rightarrow \mathbf{E} | \mathbf{r}) \xi_i(\mathbf{r}, \mathbf{E}') \\ \xi_{i+1}(\mathbf{r}, \mathbf{E}) &= \int d\mathbf{r}' T(\mathbf{r}' \rightarrow \mathbf{r} | \mathbf{E}) \chi_i(\mathbf{r}', \mathbf{E}). \end{aligned} \quad (3.10)$$

The zero order terms χ_0 and ψ_0 from (3.10) are the density of source particles and the particles entering from the first collision correspondingly. Here the benefit of using two separate equations becomes evident. The quantity χ_{i+1} denotes the density of particles leaving their $i+1$ collision and ψ_i is the density of particles entering this collision. The Monte Carlo solution of the transport problem is an iterative update of the densities of particles entering and leaving a collision. As mentioned above the two equations describing the collision densities can be reduced to a single equation by substitution. Substitution of (3.8) in (3.7) yields (3.11)

$$\begin{aligned} \xi(\mathbf{r}, \mathbf{E}) &= \int d\mathbf{r}' Q(\mathbf{r}, \mathbf{E}) T(\mathbf{r}' \rightarrow \mathbf{r} | \mathbf{E}) + \\ &+ \int d\mathbf{E}' \int d\mathbf{r}' T(\mathbf{r}' \rightarrow \mathbf{r} | \mathbf{E}) C(\mathbf{E}' \rightarrow \mathbf{E} | \mathbf{r}') \xi(\mathbf{r}', \mathbf{E}'). \end{aligned} \quad (3.11)$$

Using the simplified notation for points in the phase space, denoting the kernel of (3.11) by $K(Q, Q')$ and identifying $\int d\mathbf{r}' Q(\mathbf{r}, \mathbf{E}) T(\mathbf{r}' \rightarrow \mathbf{r} | \mathbf{E})$ with the zeroth term of the von Neumann series $\psi_0(\mathbf{r}, \mathbf{E})$ yields (3.12)

$$\xi(P) = \xi_0(P) + \int dP' K(P \rightarrow P') \xi(P'). \quad (3.12)$$

In most of the cases, the collision densities are not of interest but the functionals involving them are, such as, reaction rates or detector responses. These quantities can be derived from either the incoming or the outgoing particle densities

$$\begin{aligned} R &= \int dP \eta_\chi(P) \chi(P) \\ R &= \int dP f_\xi(P) \xi(P), \end{aligned} \quad (3.13)$$

where $f_\psi(P)$ and $\eta_\chi(P)$ from (3.13) are the payoff functions. They are determined by the physical quantity to be estimated. The definition of the payoff function can be used to estimate differential quantities, in this case (3.13) transforms to (3.14)

$$\begin{aligned} R &= \int dP f_\xi^x(P) \xi(P) \\ R &= \int dP \eta_\chi^x(P) \chi(P). \end{aligned} \quad (3.14)$$

Here superscript x denotes the bin structure, for instance, energy intervals or geometric subdivision. Important consequences can be drawn from the above definition. The bins x are estimated using the same quantity and they are correlated. The estimates are independent of the simulation process. One can build the estimates by evaluating the data after the transport calculation. This was a common technique in the past with the aim of saving computer resources.

The simplest type of response is the number of collisions within a certain domain Γ

$$R = \iiint dE d\mathbf{r} d\hat{\Omega} h_\Gamma(\mathbf{r}) \Psi(\mathbf{r}, E, \hat{\Omega}). \quad (3.15)$$

$h_\Gamma(\mathbf{r})$ from (3.15) is the characteristic function of the domain Γ i.e. $h_\Gamma(\mathbf{r}) = 0$ only if $\mathbf{r} \in \Gamma$. The same estimator can be used for determining reaction rates

$$R = \iiint dE d\mathbf{r} d\hat{\Omega} h_\Gamma(\mathbf{r}) \frac{\Sigma_r(\mathbf{r}, E)}{\Sigma_t(\mathbf{r}, E)} \Psi(\mathbf{r}, E, \hat{\Omega}). \quad (3.16)$$

The above formulas establish important relation to the flux integral. Rewriting (3.16) and using the relationship $\xi = \Psi \Sigma_t$ yields (3.17)

$$R = \iiint dE d\mathbf{r} d\hat{\Omega} h_\Gamma(\mathbf{r}) \frac{\xi(\mathbf{r}, E, \hat{\Omega})}{\Sigma_t(\mathbf{r}, E)}. \quad (3.17)$$

In the Monte Carlo codes one usually associates a certain weight w_i to each particle from the simulation [25]. Using the concept of particle weight one obtains (3.18)

$$\widehat{R} = \frac{1}{N} \sum_{i=1}^N \frac{w_i h_{\mathbf{r}}(\mathbf{r}_i)}{\Sigma_t(\mathbf{r}_i, E_i)}. \quad (3.18)$$

This type of estimator is unsuitable for low collision and void cells. However, for high collision regions like the fuel pellets, it gives fairly good results. The main advantage when compared with (3.19) is that the tally subroutines are called less frequently and the calculation of the distance traveled by the particle is not needed.

To overcome the inefficiencies of the collision estimator in case of low collision cells, most modern Monte Carlo codes use the track length estimator. It can be derived by substituting (3.8) in (3.17) and using the abbreviation $\mathbf{E} = (E, \hat{\Omega})$

$$R = \int d\mathbf{E} \int d\mathbf{r} \frac{\int d\mathbf{r}' \chi(\mathbf{r}', \mathbf{E}) T(\mathbf{r}' \rightarrow \mathbf{r} | \mathbf{E})}{\Sigma_t(\mathbf{r}, \mathbf{E})}. \quad (3.19)$$

From (3.19) the pay off function can be deduced and it can be proven [24] that

$$f_{\chi}(\mathbf{r}, \mathbf{E}) = \frac{\int d\mathbf{r}' \chi(\mathbf{r}', \mathbf{E}) T(\mathbf{r}' \rightarrow \mathbf{r} | \mathbf{E})}{\Sigma_t(\mathbf{r}, \mathbf{E})} = \langle l \rangle. \quad (3.20)$$

Where $\langle l \rangle$ is the expected path length of the particle. Using the concept of particle weight the final form as it is used by Monte Carlo codes is obtained

$$\widehat{R} = \frac{1}{N} \sum_{i=1}^N w_i l_i. \quad (3.21)$$

Another important quantity is the criticality eigenvalue. It is by definition the ratio of the number of fissions in two successive iterations. **MCNP** uses three different estimators together with a combined estimator for computing the eigenvalue. These are the collision (3.22), track length (3.24) and absorption (3.24) estimators.

$$k_{\text{eff}}^C = \frac{1}{N} \sum_i w_i \left[\frac{\Sigma_f \nu}{\Sigma_t} \right] \quad (3.22)$$

$$k_{\text{eff}}^T = \frac{1}{N} \sum_i w_i l_i \Sigma_f \nu \quad (3.23)$$

$$k_{\text{eff}}^A = \frac{1}{N} \sum_i w_i \left[\frac{\sigma_{z,f} \nu_z}{\sigma_{z,f} + \sigma_{z,c}} \right], \quad (3.24)$$

where ν is the fission neutron yield. Note, that in contrast to the other two estimators, microscopic capture $\sigma_{z,c}$ and fission $\sigma_{z,f}$ cross sections for the specific collision nuclide z are used for the absorption estimator of k_{eff} .

Since the Monte Carlo estimates are mean values accumulated by stochastic sampling, each estimator have associated standard deviation S and is computed as a mean value $\langle x \rangle$ of N samples. To indicate the statistical uncertainty, Monte Carlo codes report the results from the calculation with their corresponding relative error, defined as

$$\text{Relative error} = \frac{S}{\langle x \rangle \sqrt{N}}. \quad (3.25)$$

This value is used later in this work to judge the quality of the Monte Carlo results.

3.2 Fission source convergence

Monte Carlo methods rely on a modified version of the power method, often referred to as the method of successive generations for estimating the fundamental eigenpair of the stationary transport operator. This method uses successive cycles in which individual neutron histories are followed and the fission events they are tallied. The estimated fission source distribution from each cycle is randomly sampled to provide starting fission sites for the neutrons in next cycle. This strategy is similar to the power iteration method used in matrix calculations. Being an iterative process, it requires a number of iterations until a stationary source distribution is obtained. For the first criticality cycle the user specified initial source distribution is needed. The quality of this initial source guess determines the fission source convergence rate. Starting tallying before the source distribution has converged will result in a biased calculation. The convergence rate of the source is determined by the dominance ratio of the system. Consider the stationary transport equation (3.26)

$$\begin{aligned} \left[\hat{\Omega} \cdot \nabla + \Sigma_t(\mathbf{r}, E) \right] \Psi(\bar{\mathbf{r}}, E, \hat{\Omega}) &= \frac{\chi(E)}{k_{\text{eff}}} \int \int \nu \Sigma_f(\mathbf{r}, E') \Psi(\mathbf{r}, E', \hat{\Omega}') dE' d\hat{\Omega}' + \\ &+ \int \int \Sigma_s(\mathbf{r}, \hat{\Omega} \cdot \hat{\Omega}', E' \rightarrow E) \Psi(\bar{\mathbf{r}}, E', \hat{\Omega}') dE' d\hat{\Omega}'. \end{aligned} \quad (3.26)$$

It would be more convenient to simplify the notation and write [26]

$$\begin{aligned} \hat{\mathbf{L}}\Psi &= \hat{\mathbf{S}}\Psi + \frac{1}{k_{\text{eff}}}\hat{\mathbf{F}}\Psi \\ \Psi &= \frac{1}{k_{\text{eff}}}(\hat{\mathbf{L}} - \hat{\mathbf{S}})^{-1}\hat{\mathbf{F}}\Psi = \frac{1}{k_{\text{eff}}}\hat{\mathbf{M}}\Psi. \end{aligned} \quad (3.27)$$

Where the loss term is defined by $\hat{\mathbf{L}} = \hat{\Omega} \cdot \nabla + \Sigma_t(\mathbf{r}, E)$. This equation is solved by successive iterations. The iteration starts with initial source guess Ψ_0 . Expanding Ψ_0 in terms of the eigenfunctions u_j of (3.26) and substituting in the recurrence relation derived from (3.27) yields [26]

$$\begin{aligned} \Psi^{(n+1)} &= \frac{1}{k^{(n)}}\hat{\mathbf{M}}\Psi^{(n)} = \frac{1}{k^{(n)}k^{(n-1)}} \cdots \frac{1}{k^{(0)}}\hat{\mathbf{M}}^n\Psi^{(0)} = \\ &= \frac{1}{k^{(n)}k^{(n-1)}} \cdots \frac{1}{k^{(0)}}\hat{\mathbf{M}}^n \{a_0u_0 + a_1u_1 + a_2u_2 + \cdots\} = \\ &= \frac{k_0^n}{k^{(n)}k^{(n-1)} \cdots k^{(0)}} \times a_0 \times \left[u_0 + \frac{a_1}{a_0}(\rho)^{(n+1)}u_1 + \frac{a_2}{a_0}\left(\frac{k_2}{k_0}\right)^{(n+1)}u_2 + \cdots \right] \\ \rho &= \frac{k_1}{k_0}, \end{aligned} \quad (3.28)$$

where $\{k_i\}$ is the set of eigenvalues of the transport operator. Here ρ denotes the dominance ratio and according to (5.2) determines the convergence of the expansion. a_n are expansion coefficients. If ρ approaches unity the system is stated to have large dominance ratio. Usually in the Monte Carlo calculations, one defines the number of skipped cycles needed to converge the source. The number of those cycles should be carefully selected. To monitor the convergence behavior **MCNP** offers the Shannon Entropy method. It consist of overlaying a mesh of N_s elements and monitoring the number of source cites in a particular mesh element $\#_i$. The superimposed mesh encompasses all the fissionable regions. Following the definitions from [25] , [27] the fraction of source sites in a certain mesh element is defined as

$$P_J = \frac{\#_i}{\sum_i \#_i}, \quad (3.29)$$

The Shannon entropy is then defined to be

$$H_{src} = - \sum_{j=1}^{N_s} P_J \ln(P_J). \quad (3.30)$$

H_{src} converges to a single steady state value as the source distribution approaches stationary. The values of H_{src} are computed and printed for each criticality cycle of **MCNP** . The code computes the average $\langle H_{src} \rangle$ for the last half of the active cycles, as well as its standard deviation. At the end of each run, **MCNP** reports the first cycle falling within one standard deviation of its average over the last half cycles. This value is used as a suggestion when tallying might be started [27]. In addition to the fission source, convergence of the eigenvalue should also be monitored. Being an integral quantity, the convergence of the eigenvalue is much easier to achieve.

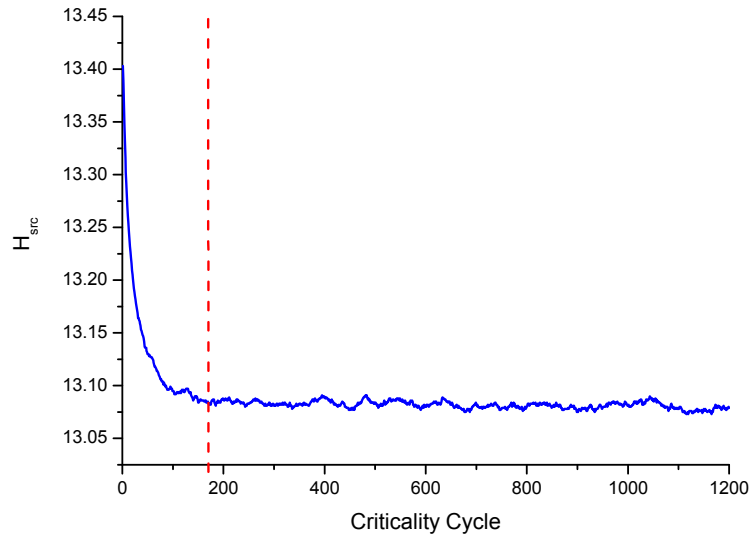


Figure 3.1: Evolution of the Shannon entropy H_{src} vs. criticality cycle.

Two plots showing H_{src} and k_{eff} vs. criticality cycle are shown in fig. 3.1 and fig. 3.2. The computation problem consists of a quarter PWR core. 1200 cycles with 10^6 neutrons per cycle were simulated. As expected H_{src} converges much slower, the vertical line in fig. 3.1 shows cycle 170, when **MCNP** detected source convergence.

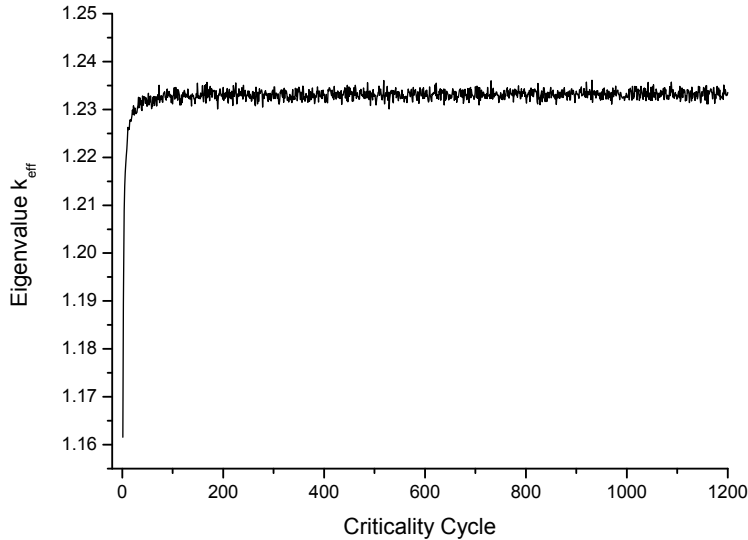


Figure 3.2: Evolution of the eigenvalue k_{eff} vs. criticality cycle.

Different methods have been applied to accelerate the fission source convergence. **MCNP** offers the possibility to define sources via the **SDEF** card, user specified source subroutine or by reading the fission source from some previous **MCNP** run. In this work two other methods were developed. Acceleration of the fission source via the Wielandt method and sampling the fission source distribution via power profile. Using the power profile to define the fission source is a very convenient method, due to the possibility to use either power coming out from an actual calculation or a user specified guess. For instance, a fair estimate would be cosine axial and a flat radial distribution. The method can be further elaborated by computing the radial power with a deterministic neutron transport code. The Wielandt method is a much more elaborate procedure requiring modifications of the **MCNP** code. It provides rapid convergence of the Monte Carlo power iteration by reducing the dominance ratio of the system. The Monte Carlo implementation of the Wielandt acceleration will be presented in Chapter 4.

3.3 Nonanalog Monte Carlo transport

The simplest form of Monte Carlo transport is analog transport. The analog transport model uses the natural probabilities to sample the different reactions that occur along the path of the simulated particles. Each subsequent event along a particle trajectory is sampled from a number of possible events according to the natural probabilities. This model is directly analogous to the naturally occurring transport and hence the name.

Analog transport gives good results in the cases when significant number of the particles contribute to the Monte Carlo estimate of interest. This situation can be significantly different for some cases. Consider the problem of detecting particle flux behind a thick shielding material e.g. gamma source and detector separated by a thick lead wall. In this case due to heavy absorption, the fraction of particles that contribute to the detector response might be easily $\times 10^{-6}$. In such situations the analog transport model will produce very large uncertainties.

A heuristic approach to improve the statistical uncertainty of the shielding problem, would be to simply run more particle histories. This methodology will be very inefficient in practices, since the much larger number of simulated histories will increase significantly the computing time.

Consider the situation where absorption is treated as scattering, meaning that all the particles emitted will reach the detector. In this case the fraction of particles contributing to the detector estimate will be unity and the variance will be substantially reduced. To keep the score unbiased, the score weight must be modified. Since the probability for scattering is given by the ratio of the scattering cross section Σ_s to the total cross section Σ_t , the weight w would have to fulfill the condition

$$\begin{aligned} w \times \text{biased probability distribution} &= w_0 \times \text{unbiased probability distribution}, \\ w \times 1 &= w_0 \times \frac{\Sigma_s}{\Sigma_t}, \\ w &= w_0 \times \frac{\Sigma_s}{\Sigma_t}, \\ \text{after } n \text{ collisions: } w &= w_0 \times \left(\frac{\Sigma_s}{\Sigma_t} \right)^n. \end{aligned}$$

Note that in the non analog transport all collisions are treated as scattering, hence the probability is unity. Since all the particles are contributing to the score, the statistical uncertainty will be significantly reduced. This nonanalog technique of reducing the variance is called implicit capture and is standard tool in deep penetration problems. It is also used as a default option in the eigenvalue calculation mode of **MCNP**, where absorption is not explicitly sampled. If the weight of the particle becomes smaller than a certain threshold, the particles are either killed or have their weights increased according to a stochastic selection rule.

One can summarize that nonanalog Monte Carlo model attempts to follow “interesting” particles more often than “uninteresting” ones. An “interesting” particle is one that contributes a large amount to the quantity (or quantities) that needs to be estimated [25]. Such nonanalog, or variance reduction, techniques can often decrease the relative error by sampling naturally rare events with an unnaturally high frequency and weighting the tallies appropriately.

To clarify further the concepts of Monte Carlo weights and variance reduction consider the standard problem of computing averages. Let $x^{(i)}$ be a set of samples drawn according to $p(x)$. In this case, the expectation value of the function $f(x)$ under $p(x)$ can be approximated

by the average of $f(x)$ evaluated at those samples

$$\langle f \rangle = \int f(x)p(x)dx \approx \frac{1}{N} \sum_{i=1}^N f(x^{(i)}). \quad (3.31)$$

Usually, it is possible to evaluate the values of $p(x)$ at given x , but drawing samples directly from $p(x)$ is either inefficient or impossible. To deal with this, another distribution $q(x)$ called the sampling distribution is used to draw \bar{x}^i from. This strategy is referred to as importance sampling. The modified average value reads

$$\begin{aligned} \langle f \rangle &= \int f(x) \frac{p(x)}{q(x)} q(x) dx, \\ &\approx \frac{1}{N} \sum_{i=1}^N \frac{p(\bar{x}^i)}{q(\bar{x}^i)} f(\bar{x}^i), \\ &= \frac{1}{N} \sum_{i=1}^N w_i f(\bar{x}^i) \\ w_i &= \frac{p(\bar{x}^i)}{q(\bar{x}^i)}. \end{aligned}$$

In the above equation the concept of statistical weights w_i is introduced. Coming back to the scattering example we obtain $p(x) = \frac{\Sigma_s}{\Sigma_t}$ and $q(x) = 1$.

The decision to draw samples from a modified distribution, has profound effect on the variance of the expectation value. Consider the expression for the variance

$$\sigma^2(f) = \int (f(x) - \langle f \rangle)^2 p(x) dx = \int f^2(x) p(x) dx - (\langle f \rangle)^2. \quad (3.32)$$

Substituting for the importance sampling case yields the following expression for the variance

$$\begin{aligned} \sigma^2(\bar{f}) &= \int f^2(x) \left[\frac{p(x)}{q(x)} \right]^2 q(x) dx - (\langle f \rangle)^2, \\ &= \int f^2(x) \left[\frac{p(x)}{q(x)} \right] p(x) dx - (\langle f \rangle)^2. \end{aligned} \quad (3.33)$$

Therefore, if the ratio $w = \frac{p(x)}{q(x)}$ in (3.33) is chosen smaller than unity the variance is reduced, that is

$$\sigma^2(\bar{f}) = \sigma^2(f \cdot \frac{p}{q}). \quad (3.34)$$

The condition $\frac{p(x)}{q(x)} < 1$ gives also a prescription how to select the modified sampling distribution. The choice should be made such, so that the weight is reduced. This is confirmed in the scattering example, since $\frac{p(x)}{q(x)} = \frac{\Sigma_s}{\Sigma_t} < 1$ and after each collision the weight is reduced. More sophisticated examples of this technique will be presented in Chapter 7, where they are used to improve the variance of the fission heat deposition.

3.4 Monte Carlo and deterministic transport

Apart from Monte Carlo simulations another class of solution method for the neutron transport equation exists, called deterministic methods. These methods discretize the phase space and apply various approximations [28]. The discretized problem is reduced to a system of algebraic equations. One approximation used by all the deterministic codes is the energy discretization.

Consider the steady state neutron transport equation (3.35)

$$\begin{aligned} \left[\hat{\Omega} \cdot \nabla + \Sigma_t(\mathbf{r}, E) - \frac{1}{k_{\text{eff}}} \hat{\mathbf{F}} \right] \Psi(\mathbf{r}, E, \hat{\Omega}) &= \hat{\mathbf{S}} \Psi(\mathbf{r}, E, \hat{\Omega}) \\ \hat{\mathbf{F}} \Psi(\mathbf{r}, E, \hat{\Omega}) &= \frac{\chi(E)}{4\pi} \int \int \nu \Sigma_f(\mathbf{r}, E') \Psi(\mathbf{r}, E', \hat{\Omega}') dE' d\hat{\Omega}' \\ \hat{\mathbf{S}} \Psi(\mathbf{r}, E, \hat{\Omega}) &= \int \int \Sigma_s(\mathbf{r}, \hat{\Omega} \cdot \hat{\Omega}', E' \rightarrow E) \Psi(\mathbf{r}, E', \hat{\Omega}') dE' d\hat{\Omega}' \end{aligned} \quad (3.35)$$

Instead of dealing with $\Psi(\mathbf{r}, E, \hat{\Omega})$ as a continuous function of E , subdivide the energy interval into G energy groups

$$\Delta E_g = [E_g, E_{g+1}] \text{ with} \quad (3.36)$$

$$g = \{g \in \mathbb{N}, g \leq G\}.$$

Using the approximation (3.36) and integrating over ΔE_g the neutron transport equation (3.35) becomes (3.37)

$$\begin{aligned} \hat{\Omega} \cdot \nabla \int_{\Delta E_g} dE \Psi(\mathbf{r}, E, \hat{\Omega}) + \int_{\Delta E_g} dE \Sigma_t(\mathbf{r}, E) \Psi(\mathbf{r}, E, \hat{\Omega}) &= \\ \int_{\Delta E_g} dE \sum_{g'=1}^G \int_{\Delta E_{g'}} dE' \int_{4\pi} d\hat{\Omega}' \Sigma_s(\mathbf{r}, \hat{\Omega} \cdot \hat{\Omega}' E' \rightarrow E) \Psi(\mathbf{r}, E', \hat{\Omega}') &+ \\ + \int_{\Delta E_g} dE \frac{1}{k} \frac{\chi(E)}{4\pi} \sum_{g'=1}^G \int_{\Delta E_{g'}} dE' \int_{4\pi} d\hat{\Omega}' \nu \Sigma_f(\mathbf{r}, E') \Psi(\mathbf{r}, E', \hat{\Omega}') & \end{aligned} \quad (3.37)$$

Assuming a separation Ansatz for the energy dependence and normalizing (3.38)

$$\begin{aligned} \Psi(\mathbf{r}, E, \hat{\Omega}) &= f(E) \cdot \phi(\mathbf{r}, \hat{\Omega}) \\ \int_{\Delta E_g} f(E) dE &= 1 \end{aligned} \quad (3.38)$$

the energy discretized neutron transport equation becomes (3.39)

$$\begin{aligned} \hat{\Omega} \cdot \nabla \phi_g(\mathbf{r}, \hat{\Omega}) + \Sigma_g(\mathbf{r}) \phi_g(\mathbf{r}, \hat{\Omega}) &= \sum_{g'=1}^G \int_{4\pi} d\hat{\Omega}' \Sigma_{s,gg'}(\mathbf{r}, \hat{\Omega} \cdot \hat{\Omega}') \phi_g(\mathbf{r}, \hat{\Omega}') + \\ &+ \frac{1}{k} \frac{\chi_g}{4\pi} \sum_{g'=1}^G \int_{4\pi} d\hat{\Omega}' \nu_{g'} \Sigma_{f,g}(\mathbf{r}) \phi_{g'}(\mathbf{r}, \hat{\Omega}') \end{aligned} \quad (3.39)$$

This form of the neutron transport equation is the basis for all deterministic codes. It reduces the continuous energy transport equation to a coupled system of equations [29]. This formulation requires in advance prepared multigroup nuclear cross section data, which are in turn collapsed from continuous energy. The number of energy groups varies, depending on the application. Core simulators usually use two groups. Lattice solvers apply finer energy discretization, usually few hundred groups.

To solve (3.39) with deterministic methods, both the space and the angular dependence need to be discretized. Usually the spatial dependence is discretized by splitting the geometry into a number of spacial domains. To illustrate some of the strategies for treating the angular dependence consider the one dimensional monochromatic form of the neutron transport equation (3.40)

$$\mu \frac{\partial \psi(x, \mu)}{\partial x} + \Sigma_t(x) \psi(x, \mu) = \frac{1}{2} \int_{-1}^1 \Sigma_s(x, \mu_0) \psi(x, \mu) d\mu + S(x, \mu), \quad (3.40)$$

where $\mu_0 = \cos \theta_0$ is the cosine of the angle between the directions $\mu = \cos \theta$ and $\mu' = \cos \theta'$. If the angular dependence is expanded in orthogonal Legendre polynomials (3.41)

$$\begin{aligned} \psi(x, \mu) &= \sum_{l=0} \frac{2l+1}{2} \phi_l(x) P_l(\mu) \\ \Sigma_s(x, \mu_0) &= \sum_{l=0} \frac{2l+1}{2} \Sigma_{s,l}(x) P_l(\mu_0) \\ S(x, \mu_0) &= \sum_{l=0} \frac{2l+1}{2} S_l(x) P_l(\mu) \end{aligned} \quad (3.41)$$

By this the following form of the transport equation is obtained

$$\begin{aligned} \frac{l+1}{2l+1} \frac{d\phi_{l+1}}{dx} + \frac{l}{2l+1} \frac{d\phi_{l-1}}{dx} + [\Sigma_t(x) - \Sigma_{s,l}(x)] \phi_l(x) &= S_l(x), l = 0, L-1 \\ \frac{l}{2l+1} \frac{d\phi_{L-1}}{dx} + [\Sigma_t(x) - \Sigma_{s,l}(x)] \phi_L(x) &= S_L(x). \end{aligned} \quad (3.42)$$

In the general three dimensional case the flux is expanded in terms of spherical harmonics $Y_{l,m}(\hat{\Omega})$

$$\psi(\mathbf{r}, E, \hat{\Omega}, t) = \sum_{l=1}^L \sum_{m=-l}^l \phi_{l,m}(\mathbf{r}, E, t) Y_{l,m}(\hat{\Omega}).$$

To derive the equations (3.42), the closure relation $\frac{d\phi_L}{dx} = 0$, known as P_L approximation was used. Depending on the, problem different number of terms are used for the angular expansion. If the zeroth order is used the neutron transport equation is reduced to diffusion problem. This is a widely used approximation, unfortunately due to the neglected anisotropy the solution near locations where strong anisotropy of the flux is present is inaccurate. For instance, near reflectors or control rods. A more accurate approximation is made by considering the first order Legendre moments. In this case, on the basis of (3.42) a three dimensional equations are derived. Replacing the derivatives with either gradient ∇ or divergence $\nabla \cdot$ depending whether the index l is even or odd. These are the simplified P_3 or SP_3 equations. Since the truncation error in spatial discretisation is of significant concern in deterministic calculations, several techniques are used, such as finite differencing, finite element and nodal methods. Usually deterministic codes using low order approximation of the angular dependence utilize homogenization theory. These cross sections are inserted into the homogenized version of the transport equation and deliver the same results for certain important quantities. The most important of them being the multiplication constant, the group reaction rates averaged over the homogenization domain and the group currents averaged over the surface of the homogenization region. The homogenized group constants $\bar{\Sigma}_{\mathbf{R}_i}^g$ are generated such so that the integral reaction rate are preserved within the homogenization volume V_i

$$\bar{\Sigma}_{\mathbf{R}_i}^g = \frac{\int_{E_{g-1}}^{E_g} \int_{\mathbf{V}_i} \bar{\Sigma}_{\mathbf{R}_i}(\mathbf{r}, E) \phi(\mathbf{r}, E) d\mathbf{r} dE}{\int_{E_{g-1}}^{E_g} \int_{\mathbf{V}_i} \phi(\mathbf{r}, E) d\mathbf{r} dE}. \quad (3.43)$$

Since local physical properties within each nodal region are more dependent on the physical properties and the thermal hydraulic conditions inside the assembly, than on the global position of the assembly in the reactor core [30],[31], the cross sections are prepared in advanced using detailed two dimensional calculations. Either lattice or stochastic codes codes are used to prepare the homogenized group constants prior to the reactor physics calculations [32],[33],[20].

Another possibility for discretising the angular dependence is to apply numerical quadrature for integrating the angular dependence. Instead of using the full set of angular directions, the transport equation is enforced to hold only on a discrete set of values μ_M

$$\mu_1, \mu_2, \dots, \mu_M. \quad (3.44)$$

Define further the following set of quadrature weights

$$w_1, w_2, \dots, w_M. \quad (3.45)$$

In this case, the angular expansion is

$$\psi(x, \mu_n) = \frac{1}{2} \sum_{l=1}^L w_l \phi_l(x) P_l(\mu_n). \quad (3.46)$$

In terms of the discretized angular variable (3.40) becomes

$$\mu_n \frac{\partial \psi_n(x)}{\partial x} + \Sigma_t(x) \psi_n(x) = \sum_{n=1}^M (2l+1) P_l(\mu_n) \Sigma_{s,l}(x) \psi_n(x) + S(x, \mu_n) \quad (3.47)$$

Integrating the angular dependence using a numerical quadrature is known as the discrete ordinates method. In one dimension only one angle is needed to specify the neutron angular distribution. In a multidimensional problem, two angular variables are required to specify the direction of neutron travel $\hat{\omega}$. The precise form of the discrete ordinates method in higher dimensions depends on the geometry type.

The quadrature set is usually chosen symmetric around $\mu = 0$ to assign the same importance of particles streaming in different directions. To avoid the case of actually having $\mu_n = 0$ even number of directions M is chosen. Different choices of the quadrature set are possible. If insufficient number of directions might result in unphysical ray effects. This might also occur in regions with low absorption cross section or localized sources.

As seen from the previous examples different approximations are used in the deterministic calculations. Increasing the resolution of the energy, angle and spatial discretization naturally increases the computational effort. In principle, by choosing fine discretization very accurate results can be provided by both the P_n and the S_n approximations.

The main advantage of the Monte Carlo method is that all the above described approximations are not needed. Violating the conditions that led to those assumptions typically results in inaccurate calculations. This is why when using deterministic codes one has to carefully consider, whether the physics of the problem is properly captured by the simulation Ansatz. Monte Carlo codes treat the full angular, space and energy dependence of the neutron flux without any approximations. Due to the fact that individual particles are tracked, it is possible to model complicated geometries by representing their corresponding surfaces via analytic equations. Deterministic codes can provide large amount of information about the solution within a single calculation. Since the solution is calculated within every discretization node of the system, obtaining the flux (power) distribution is not an issue. On the contrary, significant effort is needed to achieve the same with Monte Carlo codes. Later in chapter 4, developments to tackle the problem of efficiently obtaining flux (fission heat) estimates for large systems is presented.

Deterministic codes are difficult to scale to multiple processor cores and run time significantly

deteriorates with increasing the model resolution. Since Monte Carlo codes simulate the histories of individual particles, the codes can be very efficiently scaled to large number of cores (10000 and more) just by distributing the number of particles and providing the geometry and material description to each core. For instance, fixed source computations scale almost linearly with the number of cores.

3.5 Boundary conditions

The Monte Carlo transport equation is subjected to a set of boundary conditions [34]. Depending on the problem, one can have reflective, periodic, vacuum or white boundary conditions. The reflective boundary conditions can be either specular reflection, which as the name suggests, indicates that the incident and reflection angle are equal

$$\begin{aligned}\Psi(\mathbf{r}, E, \hat{\Omega}) &= \Psi(\mathbf{r}, E, \hat{\Omega}_R), \\ \mathbf{r} &\in \Gamma, \\ \mathbf{n} \cdot \hat{\Omega} &< 0.\end{aligned}\tag{3.48}$$

The reflective boundary conditions can be used to model infinite systems. Reflective boundary conditions are usually imposed on the symmetry cuts of a problem to reduce the computational effort. $\mathbf{r} \in \Gamma$ indicates that the tip of the radius vector is located on the reflective surface Γ . The unit vector \mathbf{n} is the outward unit normal to the reflective surface. A variation of the reflective boundary conditions is an albedo condition

$$\begin{aligned}\Psi(\mathbf{r}, E, \hat{\Omega}) &= \alpha \Psi(\mathbf{r}, E, \hat{\Omega}_R) \\ \mathbf{r} &\in \Gamma \\ \mathbf{n} \cdot \hat{\Omega} &< 0.\end{aligned}\tag{3.49}$$

The albedo α says that unlike in the case of the specular reflection (3.48) some of the particles might leave the volume. If a reliable estimate of the albedo is at hand, reflectors can be modeled very efficiently, by substituting the physical reflector volume by the parameter α . For infinite periodic geometries, periodic boundary conditions are usually used

$$\Psi(\mathbf{r}, E, \hat{\Omega}) = \Psi(\mathbf{r} + \delta, E, \hat{\Omega}).\tag{3.50}$$

Periodic boundary conditions are typically used to model infinite lattices.

To speed up the calculations by not modeling the precise reflective surface, white or isotropic reflection is used. In this case, the particles are reflected off the surface, with uniformly sampled direction.

In the case of fixed source simulation one can define the surface source. This is done by

equating the neutron flux to a function known in advance

$$\Psi(\mathbf{r}, E, \hat{\Omega}) = \mathbf{F}(\mathbf{r}, E, \hat{\Omega})$$
$$\mathbf{r} \in \Gamma \tag{3.51}$$

$$\mathbf{n} \cdot \hat{\Omega} < 0.$$

The application of these boundary conditions will be presented in this thesis. Careful application of the boundary conditions and exploiting the symmetry of the problem can significantly reduce the computational effort. Therefore, special care should be taken when setting up the problem.

Temperature dependence of the nuclear cross sections

In the past due to the limited computer resources, Monte Carlo codes have been used to model limited in size problems. Usually the data was taken at room temperature and the temperature driven effects were neglected. Although applicable to problems, such as the simulation of particle detectors, this assumption fails when reactor cores are simulated. One of the main objectives of this thesis is to develop an effective thermal hydraulic feedback model for the Monte Carlo transport code **MCNP**. When operating at hot full power conditions the coolant density, coolant temperature and the fuel temperature are represented by three dimensional distributions. Densities and temperatures vary in different parts of the core due to the different power and coolant flow distributions. These spatial variations should be properly taken into account when running the transport simulation. In particular, this means that the total cross sections have to be computed by taking into account the local medium density and temperature. To solve this problem both the temperature dependence of the microscopic nuclear data and the number densities of the different isotopes present in the material have to be corrected. Since this thesis is focused on simulating light water reactors, the moderation in the coolant is especially important. Therefore spatial attention was devoted to developing a method for treating the temperature dependence of the thermal scattering data for bound hydrogen. In this chapter the temperature dependence of the single and double differential data is discussed. Techniques for correcting the temperature dependent effects used in this thesis are presented and verified.

4.1 Temperature dependence of the single differential nuclear data

One of the most powerful features of the Monte Carlo codes is the use of 'continuous-energy' nuclear data. Cross sections are reconstructed from resonance parameters and are stored on an energy grid with hundred of thousands of energy points. This is a major difference when compared to deterministic codes, where the energy dependence is usually averaged over an energy interval. In fig. 4.1 cross sections describing the interaction of the ${}_{92}^{238}\text{U}$

nucleus with neutrons are plotted versus the incident neutron energy.

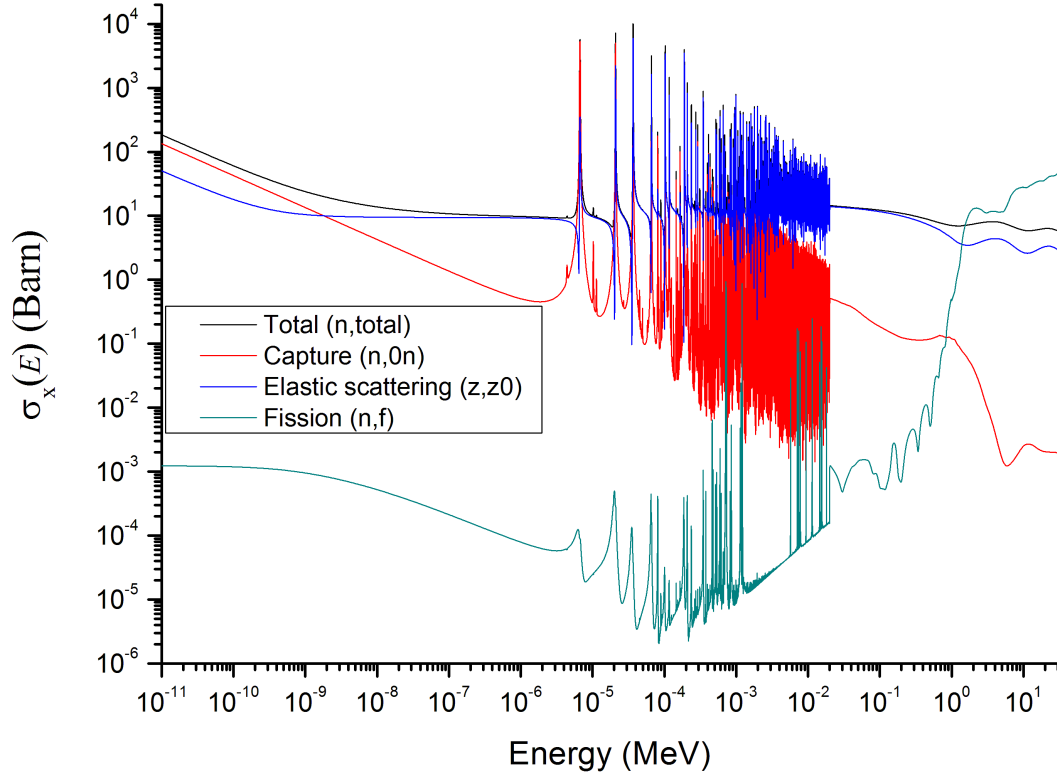


Figure 4.1: Cross sections of ${}^{238}_{92}\text{U}$ as a function of the incident neutron energy.

The nuclear cross sections depend on the relative velocity in the center of mass frame. Temperature motion of the target nuclei results in the Doppler effect, which is one of the most important phenomena in reactor physics. The temperature dependence of the nuclear data is determined by the following convolution with the Maxwell-Boltzmann distribution $P(\mathbf{v}, T)d\mathbf{v}$ [35] [36]

$$\rho v \sigma(v, T) = \int d\mathbf{v}' \rho |\mathbf{v} - \mathbf{v}'| \sigma(|\mathbf{v} - \mathbf{v}'|) P(\mathbf{v}', T) \quad (4.1)$$

$$P(\mathbf{v}', T) d\mathbf{v}' = \left(\frac{M}{2kT\pi} \right)^{\frac{3}{2}} \exp\left(-\frac{M}{2kT} v'^2 \right) d\mathbf{v}'.$$

Here \mathbf{v} is the neutron velocity, \mathbf{v}' denotes the velocity of the target nucleus and $\mathbf{v} - \mathbf{v}'$ is the relative velocity. It is possible to see clearly that the cross section depends on the relative velocity between the neutrons and the target nuclei. As the nuclei are in thermal motion, the relative velocity can change. This difference between the relative velocities rises to the Doppler deviation effect. The effect of Doppler broadening is shown in fig. 4.2 for the 6.675 eV resonance of ${}^{238}_{92}\text{U}$. The resonances tend to become wider and reduce their amplitude.

Exception are the v^{-1} cross section that remain unchanged. In general, the area under a resonance does change unless $E \gg \frac{kT}{A}$, where A is the mass number. In fact, each resonance develops v^{-1} tail. Constant cross section (for example, elastic scattering) develops a v^{-1} tail at low energies after Doppler-broadening [36].

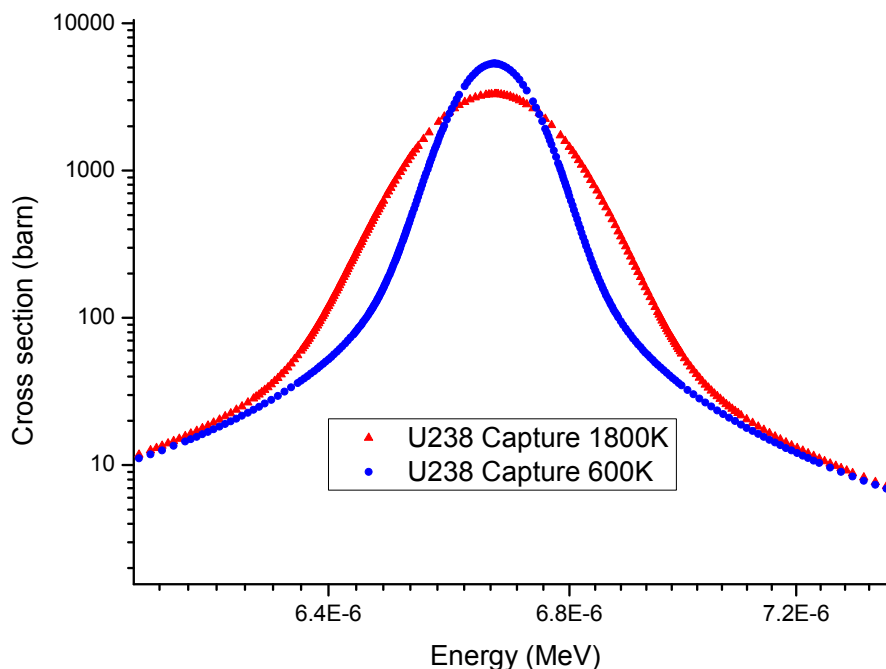


Figure 4.2: Capture cross section for U_{92}^{238} evaluated at 600K and 1800K showing the effect of Doppler broadening.

In principle, nuclear data processing codes like NJOY [36] can process the single differential data at all desired temperatures. However, in some cases this might be an impossible task. In the case of a coupled calculation, the thermal hydraulic calculation supplies fuel temperatures in the range $570K - 1200K$. Evaluating the data at $1K$ increments for the entire range would pose serious memory storage challenges. The main problem being the presence of large amount of double precision data allocated on the heap. This will slow down the computation significantly, therefore, another method for correcting the temperature dependence is needed.

The temperature dependence of the nuclear data can be taken into account using pseudo material mixing [37]. The method consists in mixing nuclear data evaluated at different temperatures and bracketing the temperature of interest. Doing so the number of materials is doubled. This method relies on the stochastic nature of the computation. The probability for interaction with a particular nuclide is given by the atomic fraction of that nuclide. Therefore, the temperature dependent atomic fractions introduce temperature dependent interaction probabilities. In practical terms this yields an 'effective' cross section (4.2) having the correct temperature

$$\Sigma_{\text{pseudo}}(T_{\text{actual}}) = f_{\text{low}}\Sigma_{\text{low}}(T_{\text{low}}) + f_{\text{high}}\Sigma_{\text{high}}(T_{\text{high}}). \quad (4.2)$$

The weights determining the concentrations of the 'low' and 'high' temperature evaluations in the case of square root weighting are given by (4.3)

$$\begin{aligned} f_{\text{high}} &= 1 - f_{\text{low}} \\ f_{\text{low}} &= \frac{\sqrt{T_{\text{high}}} - \sqrt{T_{\text{actual}}}}{\sqrt{T_{\text{high}}} - \sqrt{T_{\text{low}}}}. \end{aligned} \quad (4.3)$$

Whereas in the case of linear weighting of the mixing coefficients they are given by (4.4)

$$\begin{aligned} f_{\text{high}} &= 1 - f_{\text{low}} \\ f_{\text{low}} &= \frac{T_{\text{high}} - T_{\text{actual}}}{T_{\text{high}} - T_{\text{low}}}. \end{aligned} \quad (4.4)$$

The consistency of this methodology was verified [2], [38], [39] by comparing calculations performed with NJOY-BROADR processed data at specific temperature, and calculations performed with interpolated cross sections at the same temperature by using pseudo materials. For the actual tests, a 17x17 PWR fuel assembly with 24 guide tubes was used. The details of the computational problem are given by table 4.1 and fig. 4.3.

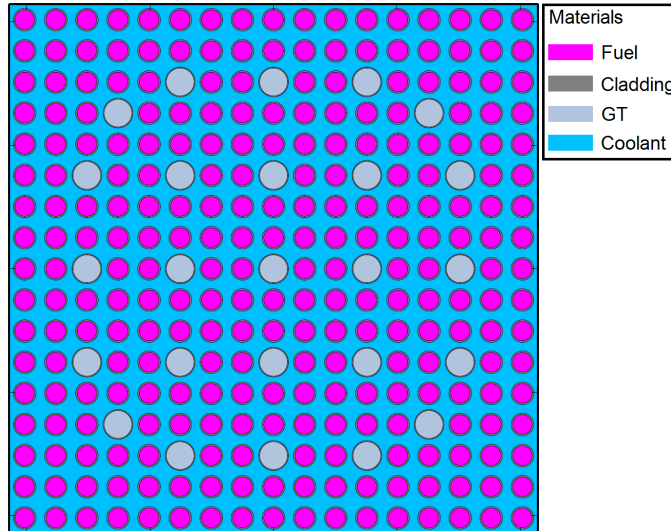


Figure 4.3: Geometry of the fuel assembly used for the numerical tests. The color code of the figure indicates the different materials. For the calculation identical coolant was used inside the guide tube and in between the fuel pins.

Table 4.1: List of the geometry and material composition data for the fuel assembly geometry specified in fig. 4.3.

Item	Value
Fuel density	10.26 g/cm ³
Coolant density	0.72 g/cm ³
Coolant temperature	573.6 K
Coolant material	Water
Fuel Material	UOX or MOX
Fuel temperature	Varies
Fuel pellet radius	0.412 cm
Fuel cladding radius	0.476 cm
Fuel cladding material	Zirconium
Fuel cladding temperature	600 K
Fuel Material	UOX or MOX
Guide tube outer radius	0.610 cm
Guide tube inner radius	0.570 cm
Guide tube material	Zirconium
Guide tube cladding temperature	600 K

Two cases were studied with UOX and MOX fuel. MOX fuel was chosen because the mixture of uranium and plutonium isotopes is expected to give higher sensitivity to thermal spectrum shifts than the UOX fuel. The MOX fuel contained 14wt% plutonium, and the UOX was enriched to 4wt%. Both cases had the same geometric dimensions. Results comparing the eigenvalue computed with exact broadened and interpolated data are shown in table 4.2 and table 4.3. Each temperature in the interpolated case is a mixture between the cross sections evaluated at $\pm 50K$ apart from it. Square root mixing given by (4.3) and linear mixing given by (4.4) were used. The Standard deviation of the eigenvalue is shown in brackets. The difference with respect to the exact broadened data is smaller in the case when linear mixing is used.

Table 4.2: Comparison of the k_{∞} values computed using linear and square root (sqrt) pseudo material mixing against the exact broadened reference data for the UOX case.

Temperature	Exact value	Pseudo material (sqrt)	Pseudo material (linear)
1000 K	1.39495 (5)	1.39500 (6)	1.39497 (5)
1150 K	1.39077 (6)	1.39085 (5)	1.39089 (6)
1250 K	1.38803 (6)	1.38803 (6)	1.38804 (6)
1400 K	1.38419 (6)	1.38416 (6)	1.38414 (6)

Both calculation agree well with the reference case. This leads to the conclusion that the

pseudo material approach gives sufficiently accurate results.

Table 4.3: Comparison of the k_{∞} values computed using linear and square root (sqrt) pseudo material mixing against the exact broadened reference data for the MOX case.

Temperature	Exact value	Pseudo material (sqrt)	Pseudo material (linear)
1000 K	1.21042 (5)	1.21047 (6)	1.21055 (7)
1150 K	1.20612 (6)	1.20596 (6)	1.20609 (7)
1250 K	1.20313 (7)	1.20312 (6)	1.20308 (7)
1400 K	1.19910 (6)	1.19921 (6)	1.19901 (6)

Based on the results obtained in this chapter it is possible to confirm the accuracy of the pseudo material mixing methodology. This method is a unique feature of the Monte Carlo codes. It allows to correct the temperature dependence of the nuclear data, by the introduction of temperature dependent interaction probabilities. Pseudo material mixing has been used in the past by explicitly defining the pseudo material compositions in the **MCNP** input. In chapter 7 of this thesis an effective method for the direct introduction of the pseudo material mixing in the neutron transport is presented.

4.2 Thermal neutron scattering

Light water reactors operate on thermal neutrons, meaning that the fission neutrons lose their initial energy in collisions with the nuclei of the moderator. The hydrogen nucleus is bound in a molecule, making the computation of the scattering reaction very complicated. Since systems having dense energy levels is considered, inelastic scattering plays a dominant role. Moreover, the local coolant temperature variation, introducing an additional degree of complication. Therefore, the proper introduction of the coolant feedback, requires methodology for treating thermal neutron scattering at varying moderator temperatures.

The theory of the thermal neutron scattering is built in the frame work of the Born approximation. The scattering amplitude in this case is given [40] as an integral (4.5) over the wave function $\Psi(\mathbf{k}, \mathbf{r})$ and the interaction potential $V(\mathbf{r})$

$$f(\theta) = -\frac{m}{2\pi\hbar^2} \int d\mathbf{r} e^{-i\mathbf{k}\cdot\mathbf{r}} V(\mathbf{r}) \psi(\mathbf{k}, \mathbf{r}). \quad (4.5)$$

The product of the interaction range and the wave vector is in this case very small $kr_0 < 10^{-4}$. This means that the scattering length a can be represented by (4.6) [41] [42]

$$a = -f(\theta)_{\mathbf{k} \rightarrow 0} = \frac{m}{2\pi\hbar^2} \int d\mathbf{r} V(\mathbf{r}). \quad (4.6)$$

The Born approximation is not directly applicable to this problem, because the weak potential condition is violated due to (4.7)

$$\frac{mV_0r_0^2}{\hbar^2} \approx 1 \quad (4.7)$$

Since the scattering length is determined by the volume integral of the potential (4.6), and since $kr_0 < 10^{-4}$ one can choose another potential having bigger range r_0 but smaller depth which will be used in place of the actual nuclear square well with depth V_0 . Doing so the condition $kr_0 \ll 1$, [41] [42] will be preserved. This choice of the potential is due to E. Fermi. For a scattering target consisting of N nuclei the potential is given by

$$V(\mathbf{r}) = \frac{2\pi\hbar^2}{m} \sum_l^N a_l \delta(\mathbf{r} - \mathbf{R}_l). \quad (4.8)$$

Since the potential enters the expression for the scattering length (4.6) only as a volume integral, the precise form is not important. Having in mind that the de Broglie wavelength is much greater than the modified range of the potential, the interaction takes place only in a small region of space.

Here \mathbf{r} and \mathbf{R}_l are the coordinates of the neutron and the scattering nucleus. This potential can be substituted in the Schrödinger equation and the following expression is obtained (4.9)

$$\begin{aligned}
(\Delta + k_n) \psi_n &= \frac{2m}{\hbar^2} \sum_n \langle n' | V | n \rangle \psi_{n'} \\
\Psi(r, E) &= \sum_n |n\rangle \psi_n(r) \\
k_n &= \frac{2m\varepsilon_n}{\hbar^2}
\end{aligned} \tag{4.9}$$

Where the wave function was expanded in the orthogonal basis $|n\rangle$ with eigenvalues ε_n of the energy representation. Using the Born approximation the scattering amplitude can be expressed as Fourier transform of the potential (4.10)

$$\begin{aligned}
f(n_0 \rightarrow n) &= -\frac{2\pi\hbar^2}{m} \int d\mathbf{r} \exp(i(\mathbf{k}_i - \mathbf{k}_n) \cdot \mathbf{r}) \langle n | V(\mathbf{r}) | n_0 \rangle \\
&= -\sum_l^N a_l \langle n | \exp(i(\mathbf{k}_i - \mathbf{k}_n) \cdot \mathbf{R}_l) | n_0 \rangle \\
&= -\sum_l^N a_l \langle n | \exp(i\mathbf{Q}_n \cdot \mathbf{R}_l) | n_0 \rangle.
\end{aligned} \tag{4.10}$$

The scattering cross section can be readily defined as the modulus squared of the scattering amplitude (4.11)

$$\begin{aligned}
\frac{d^2\sigma}{d\Omega dE_f} &= \frac{1}{N} \sum_n \sum_{n_0} P(n_0) \frac{k_f}{k_i} |f(n_0 \rightarrow n)|^2 \delta(E_f + \varepsilon_n - E_i + \varepsilon_0) \\
P(n) &= \frac{\exp\left(-\frac{\varepsilon_n}{kT}\right)}{\sum_s \exp\left(-\frac{\varepsilon_s}{kT}\right)}
\end{aligned} \tag{4.11}$$

Here the quantity $P(n)$ is the probability to find the target having temperature T in the state $|n\rangle$. The delta function ensures the conservation of energy in the system neutron plus target. Substituting the integral form of the delta function yields (4.12)

$$\begin{aligned}
\frac{d^2\sigma}{d\Omega dE_f} &= \frac{k_f}{k_i} \frac{1}{2\pi N} \int_{-\infty}^{\infty} dt e^{-it(E_f - E_i)/\hbar} \chi(Q, t) \\
\chi(Q, t) &= \sum_n \sum_{n_0} P(n_0) e^{-it(\varepsilon_f - \varepsilon_i)/\hbar} |f(n_0 \rightarrow n)|^2.
\end{aligned} \tag{4.12}$$

The expression for $\chi(Q, t)$ can be further simplified (4.13)

$$\begin{aligned}
\chi(Q, t) &= \sum_{ll'} a_l a_{l'} \sum_{n_0} \frac{P(n_0)}{N} \sum_n \langle n_0 | e^{-i\mathbf{Q}_n \cdot \mathbf{R}_{l'}} e^{-itH_s/\hbar} | n \rangle \langle n | e^{i\mathbf{Q}_n \cdot \mathbf{R}_l} e^{itH_s/\hbar} | n_0 \rangle \\
\chi(Q, t) &= \sum_{ll'} a_l a_{l'} \sum_{n_0} \frac{P(n_0)}{N} \langle n_0 | e^{-i\mathbf{Q}_n(t) \cdot \mathbf{R}_{l'}} e^{i\mathbf{Q}_n \cdot \mathbf{R}_l} | n_0 \rangle .
\end{aligned} \tag{4.13}$$

H_s is the Hamiltonian of the system. This yields for the double differential cross section (4.14)

$$\begin{aligned}
\frac{d^2\sigma}{d\Omega d\omega} &= \sqrt{\frac{E_f}{E_i}} a^2 S(Q, \omega) \\
S(Q, \omega) &= \frac{1}{2\pi N} \int_{-\infty}^{\infty} dt e^{i\omega t} \sum_{ll'} \langle n_0 | e^{-i\mathbf{Q}_n(t) \cdot \mathbf{R}_{l'}} e^{i\mathbf{Q}_n \cdot \mathbf{R}_l} | n_0 \rangle \\
\hbar\omega &= E_f - E_i.
\end{aligned} \tag{4.14}$$

$\chi(Q, t)$ is called the dynamic structure factor and governs the entire scattering process of the bound nucleus. The dynamic scattering factor is divided into coherent and incoherent parts (4.15)

$$\begin{aligned}
\chi_{incoh}(Q, t) &= \sum_{ll'} a_l a_{l'} \sum_{n_0} \frac{P(n_0)}{N} \sum_l \langle n_0 | e^{-i\mathbf{Q}_n(t) \cdot \mathbf{R}_{l'}} e^{i\mathbf{Q}_n \cdot \mathbf{R}_l} | n_0 \rangle \\
\chi_{coh}(Q, t) &= \sum_l a_l^2 \sum_{n_0} \frac{P(n_0)}{N} \sum_l \langle n_0 | e^{-i\mathbf{Q}_n(t) \cdot \mathbf{R}_l} e^{i\mathbf{Q}_n \cdot \mathbf{R}_l} | n_0 \rangle
\end{aligned} \tag{4.15}$$

Computing it requires knowledge of the initial state vector $|n_0\rangle$. This is an intractable problem and significant approximations are required. Usually the incoherent approximation is assumed, where $\chi_{coh} = 0$. The Gaussian approximation is assumed further, expressing χ_{incoh} as (4.16)

$$\chi_{incoh}(Q, \omega) = \exp \left[\frac{Q^2}{2m} \left\{ - \int_0^{\infty} \frac{\rho(\zeta)}{\hbar\zeta} \coth \left(\frac{\hbar\zeta}{2kT} \right) d\zeta + \int_0^{\infty} \frac{\rho(\zeta)}{\hbar\zeta} \coth \left(\frac{\hbar\zeta}{2kT} \cos(\zeta t) + i \sin(\zeta t) \right) d\zeta + \right\} \right]. \tag{4.16}$$

The oscillation spectrum of the target nucleolus $\rho(\zeta)$ is decomposed as a sum of simple oscillation spectra [43]

$$\begin{aligned}
\int \rho(\zeta) d\zeta &= 1 \\
\rho(\zeta) &= \sum_k p_k \rho_k(\zeta).
\end{aligned} \tag{4.17}$$

The summation in (4.17) runs over translation, diffusion, solid-type and discrete oscillator spectra. The choice of the weights p_k is done to best fit experimental data. In this manner the entire physics of the problem is transformed in what is essentially a parameter optimization problem. Another important consequence is that the spectrum depends on temperature. The inelastic cross section is usually given in terms of the $S(\alpha, \beta)$ function

$$\frac{d^2\sigma}{d\Omega dE_f}(E_i \rightarrow E_f, \Omega \rightarrow \Omega') = \frac{\sigma_b^{incoh} + \sigma_b^{coh}}{4\pi kT} \sqrt{\frac{E_f}{E_i}} e^{-\frac{\beta}{2}} S(\alpha, \beta)$$

$$\alpha = \frac{Q^2}{2mkT} \quad (4.18)$$

$$\beta = \frac{E_f - E_i}{kT}.$$

Where σ_b represents the bound scattering cross section. Plots of the inelastic scattering cross section for bound hydrogen and the oscillation frequency spectrum of the target nucleus are shown in fig. 4.4 and fig. 4.5 corresponding to different temperatures available from the JEFF 3.1.1 nuclear data library.

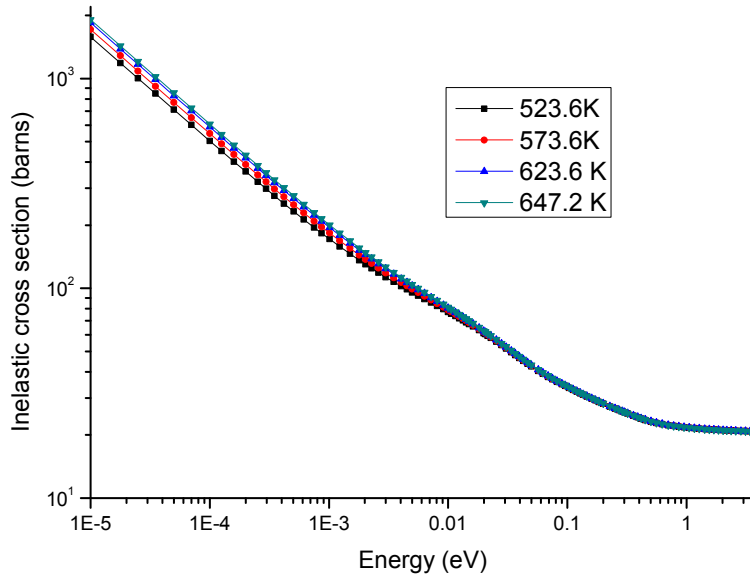


Figure 4.4: Inelastic scattering cross sections for bound hydrogen as a function of the incident neutron energy.

Thermal scattering from bound scatterers is treated in **MCNP** utilizing additional thermal scattering data files prepared by the LEAPR-THERMR-ACER modules sequence of NJOY. While the Doppler broadening module of BROADR is capable of producing cross section files at all desired temperatures, LEAPR requires frequency spectrum of the scattering nucleus $\rho(\zeta)$ for each temperature as an input for generating the scattering law $S(\alpha, \beta)$. For the current study the LEAPR input given in [43] was used. In addition, the THERMR module

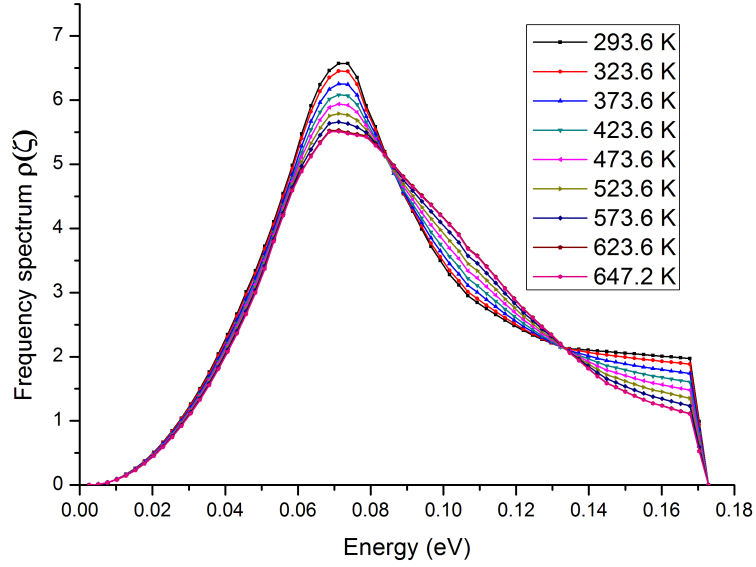


Figure 4.5: Oscillation spectrum $\rho(\zeta)$ of the target nucleus as a function of the oscillator energy.

of NJOY was used to generate the point wise thermal scattering cross sections in PENDF format and the ACER module of NJOY was used to generate thermal scattering data for **MCNP** code in ACE format. The data used in the **MCNP** calculation contains the inelastic scattering cross section, outgoing energy and directions. For each neutron having energy E_0 before the collision an interpolation factor is computed

$$\mathbf{f} = \frac{E_0 - E_i}{E_{i+1} - E_i}, \quad (4.19)$$

where the following relation holds $E_i \leq E_0 \leq E_{i+1}$. Based on the interpolation factor \mathbf{f} the outgoing energy bin is sampled from a uniform distribution and subsequently interpolated on the incoming energy grid between energies corresponding to neighboring incoming energies

$$E = E_{i,j} + \mathbf{f} (E_{i+1,j} - E_{i,j}), \quad (4.20)$$

where $E_{i,j}$ is the j -th outgoing energy corresponding to the i -th incoming energy. For each combination of incoming and outgoing energy bins (i, j) a set of k equally probable cosines $\mu_{i,j,k}$ is available. The cosine is selected uniformly out of the k values available and interpolated on the incoming energy grid

$$\mu = \mu_{i,j,k} + \mathbf{f} (\mu_{i+1,j,k} - \mu_{i,j,k}). \quad (4.21)$$

When performing coupled calculations, moderator temperatures may be significantly different from the temperatures for which thermal scattering data is available. If no action is taken the thermal scattering data will always be used inaccurately. The standard approach to correct for this effect is a simple extension of the pseudo material approach, presented hereafter.

In the **MCNP** material card one can specify two materials and via changing the corresponding atom fractions temperature correction via modified pseudo material mixing can be done. However this is not possible in the case of thermal scattering data. The material transformation card will always apply to one isotope of hydrogen only. There exists a simple trick to overcome this obstacle. One defines pseudo isotopes of hydrogen (1004, 1005, 1007, 1008) at specific temperatures, coinciding with the temperatures at which the thermal scattering law is defined. In coherence with this, the isotope index is changed correspondingly in the thermal scattering data files. From this point on, **MCNP** treats the modified data files for hydrogen as separate isotopes and it is possible to utilize more than one thermal scattering data files for hydrogen in water, within single material transformation card. Interpolation is performed via the atom fractions as usual. For the sake completeness, a sample **MCNP** material card is shown in fig. 4.6 In this example, 1004.97c and 1006.99c are NJOY evaluations of hydrogen for 523.6 K and 623.6 K, where lwal06.31t and lwal08.31t are the corresponding thermal scattering data files produced by LEAPR-THERMR-ACER sequence. The temperature being interpolated is 573.6 K. The extension of the pseudo material mixing to double differential data was proposed in [12]

```

m1      1004.97c  0.333333  $ H 523.6
        8016.97c  0.166667  $ O 523.6
        1006.99c  0.333333  $ H 623.6
        8016.99c  0.166667  $ O 623.6
mt1     lwal06.31t lwal08.31t

```

Figure 4.6: Material composition illustrating the pseudo material mixing for thermal scattering data.

4.3 Implementation of a new methodology for correcting the temperature dependence of the thermal scattering data.

Although very simple to implement, the modified pseudo material mixing for thermal scattering data gives some deviations in the flux below 0.6 eV on the order of magnitude of 5 %. This effect is in practice undetectable if only the eigenvalue is considered. Tallying the flux into multiple energy bins, however, reveals this difference [38]. Moreover, this is the energy range to which most of the neutrons in the moderator belong fig. 4.7. Note that as expected in the case of the colder moderator, more neutrons are slowed down to low energies.

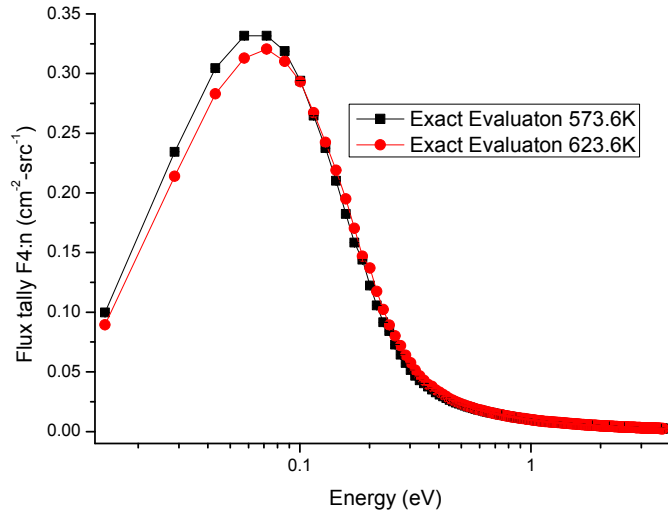


Figure 4.7: Linear logarithmic plot of the neutron flux as a function of energy evaluated for two moderator temperatures: 573.6K and 623.6K.

Therefore, to keep the claim of high fidelity calculations this problem should be properly addressed. Another approach was developed and implemented in the current work. One important physical property leading to the difference in the spectra is the method for interpolating the equal probable emission elements. Proper treatment of the problem is given in [44]. Since the extent of the data in the energy-angle phase space is inversely proportional to the probability for that element, one has to use reciprocal interpolation law. This requirement is violated when using the pseudo material mixing. In the pseudo material mixing case, the interaction with bound nuclei at different temperatures is stochastic, where the probability for selecting particular nuclide is given by the corresponding atomic fraction. Finally, the combined effect of those separate cases is used to incorporate the temperature effects. This method was abandoned and a deterministic temperature interpolation was implemented in **MCNP**. The idea is to use two step interpolation processes. The first step interpolates the inelastic scattering cross section for bound hydrogen, and the second step uses reciprocal law to select the proper equal probable emission elements. Each time when a neutron enters a moderator cell, an interpolated value for the total inelastic scattering cross section is being computed. This cross section is an interpolation between two tables, having temperatures bracketing the temperature of interest. The value of the inelastic cross section is stored in the memory and is used to further process the neutron history and govern the scattering dynamics. The second step is executed when selecting the scattering cosine (4.21) and the out scattering energy (4.20). Both of them are interpolated via reciprocal law [44]. This means that (4.21) and (4.20) are modified and the selection of the outgoing energy and angle (4.22) is done using temperature corrected values

$$E(T) = E_{i,j,T} + \mathbf{f}(E_{i+1,j,T} - E_{i,j,T}), \quad (4.22)$$

$$\mu(T) = \mu_{i,j,T} + \mathbf{f}(\mu_{i+1,j,T} - \mu_{i,j,T}).$$

Where the temperature dependence of the outgoing equal probable emission elements is corrected using

$$\mu_{i,j,k,T} = \left(\frac{x}{\mu_{i,j,k,T_1}} + \frac{1-x}{\mu_{i,j,k,T_2}} \right)^{-1}$$

$$E_{i,j,T} = \left(\frac{x}{\mu_{i,j,T_1}} + \frac{1-x}{\mu_{i,j,T_2}} \right)^{-1} \quad (4.23)$$

$$x = \frac{T - T_1}{T_2 - T_1}.$$

The newly computed value for the scattering cosine is used to compute the scattered direction. Using this methodology, the errors introduced by the pseudo material mixing were reduced and precise control over the temperature dependence correction was established.

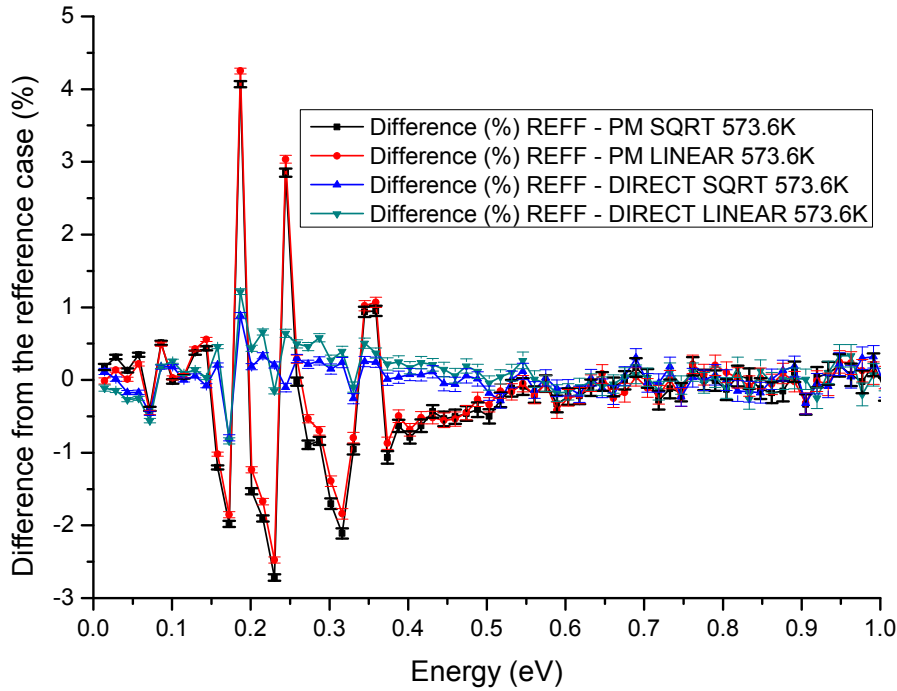


Figure 4.8: Difference in the neutron flux spectrum evaluated using interpolated data and exact evaluated data for the case of coolant temperature of 573.6 K.

The methodology was tested on the 17x17 PWR fuel assembly used to verify the pseudo material mixing for single differential data. The details of the computational problem are given by table 4.1 and fig. 4.3. The spectrum for moderator flux was tallied in 260 equally spaced energy groups for the entire range of the thermal scattering data (0-3.75eV). As a reference calculation thermal scattering data prepared by the nuclear processing code NJOY was used. In fig. 4.8 and fig. 4.9 the difference for the part of the thermal neutron spectrum below 1eV is shown. The statistical uncertainty of the tally estimates were propagated to

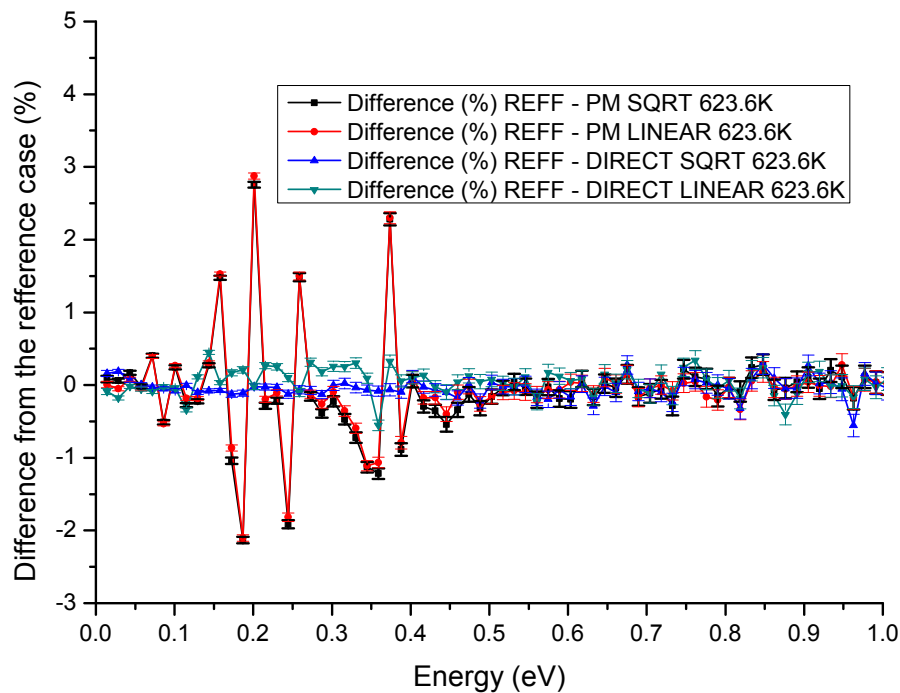


Figure 4.9: Difference in the neutron flux spectrum evaluated using interpolated data and exact evaluated data for the case of coolant temperature of 623.6 K.

the relative difference and shows that the differences are large and can not be explained by poor variance. In fig. 4.10 and fig. 4.11 the pseudo material mixing and the direct on-the-fly interpolation of the thermal scattering data is shown. As evident from fig. 4.10, the pseudo material mixing gives worse results in all the cases. Due to the low number of neutrons residing in the region above 1eV, the difference is suppressed by the large variance.

The validation calculation presented in fig. 4.11 confirms the validity of the new methodology. It is in very good agreement with the reference calculation, where the maximum difference is within 1 %. The newly developed on the fly treatment of the thermal scattering data allows the proper introduction of the moderator temperature effect. The methodology was implemented in the **MCNP** source code and is used in chapter 8 of this thesis for simulating the PWR UOX-MOX benchmark.

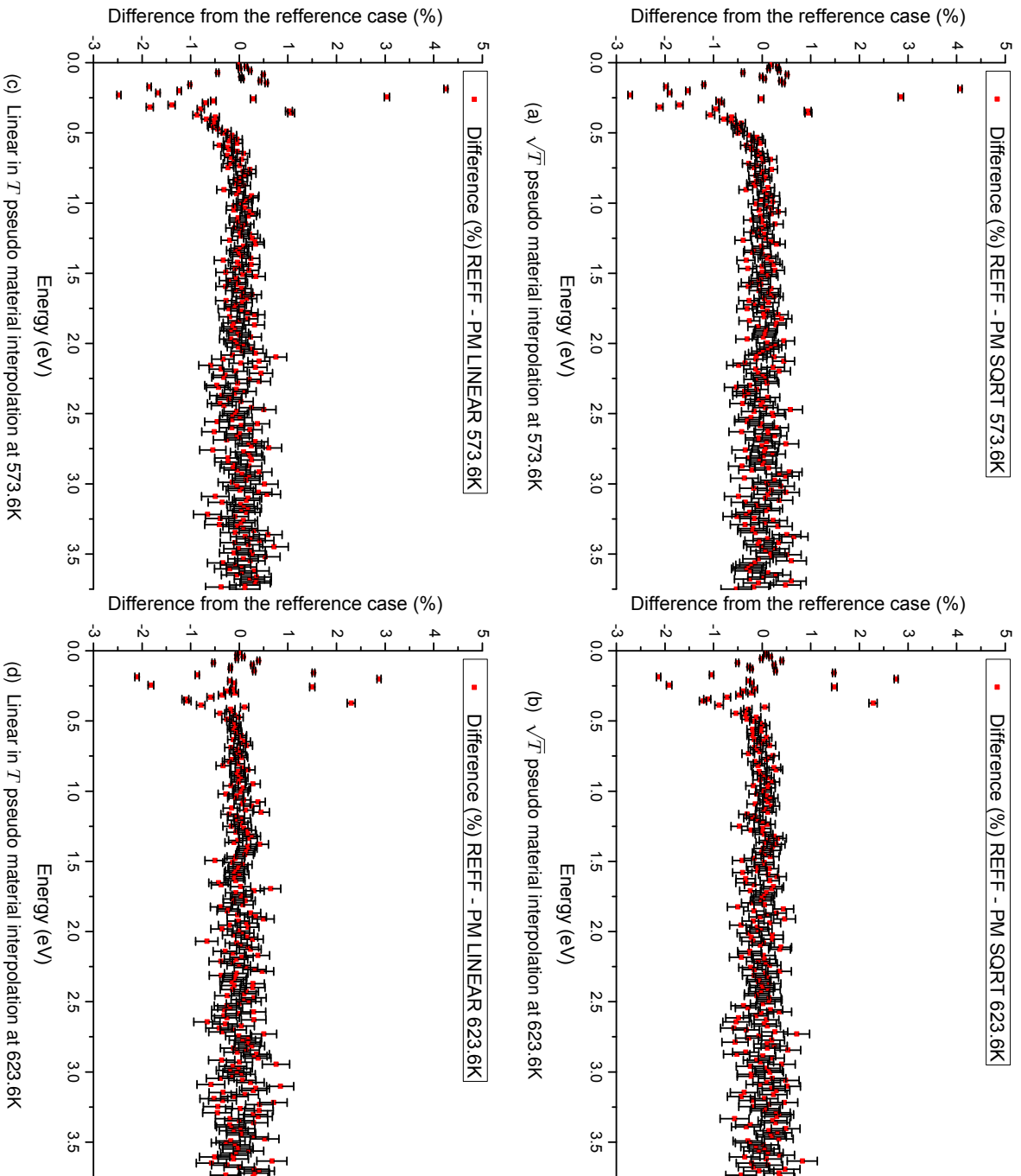


Figure 4.10: Difference between the neutron moderator spectrum evaluated using the pseudo material mixing methodology and the direct evaluated thermal scattering data.

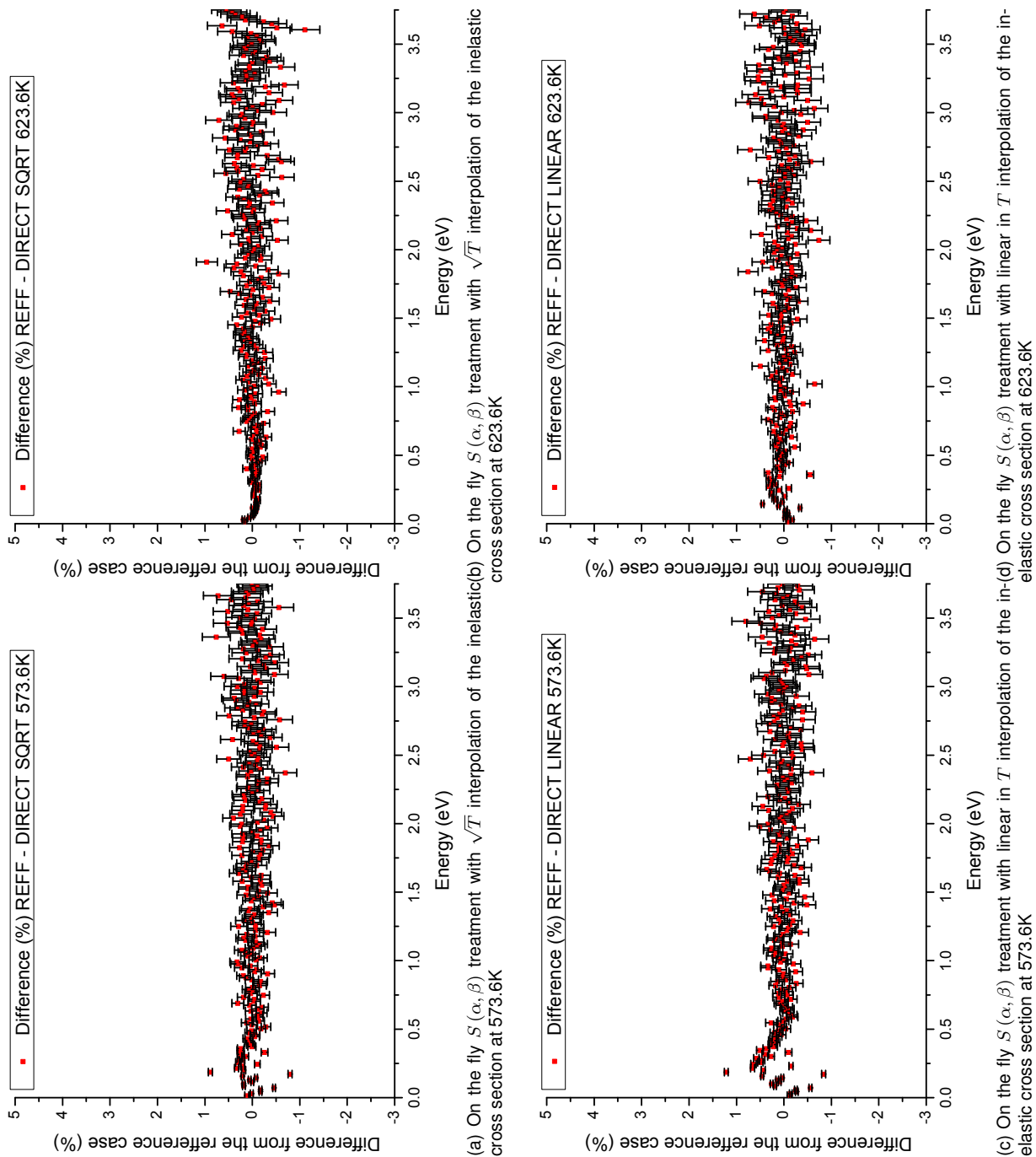


Figure 4.11: Difference between the neutron moderator spectrum evaluated using the on the fly thermal scattering interpolation and the direct evaluated thermal scattering data. The reference data is evaluated at 573.6K and 623.6K.

The Wielandt acceleration method

Running coupled Monte Carlo thermal hydraulics calculations applied to large loosely coupled systems requires a reliable method to accelerate the fission source convergence. Typically in **MCNP** one uses precalculated fission source files. Another approach is followed here, namely accelerating the fission source convergence, by modifying the transport operator.

5.1 Wielandt shift acceleration of the Monte Carlo power iteration

It is well known from the theory of iterative methods that the dominance ratio of the system can be reduced using the Wielandt acceleration technique. The essence of the method is to split the fission source. The neutron transport equation without external sources is written in the following form (5.1).

$$\left[\hat{\Omega} \cdot \nabla + \Sigma_t(\mathbf{r}, E) - \frac{1}{k_e} \hat{\mathbf{F}} \right] \Psi(\mathbf{r}, E, \hat{\Omega}) = \left(\frac{1}{k_{\text{eff}}} - \frac{1}{k_e} \right) \hat{\mathbf{F}} \Psi(\mathbf{r}, E, \hat{\Omega}) + \hat{\mathbf{S}} \Psi(\mathbf{r}, E, \hat{\Omega})$$

$$\hat{\mathbf{F}} \Psi(\mathbf{r}, E, \hat{\Omega}) = \frac{\chi(E)}{4\pi} \int \int \nu \Sigma_f(\mathbf{r}, E') \Psi(\mathbf{r}, E', \hat{\Omega}') dE' d\hat{\Omega}' \quad (5.1)$$

$$\hat{\mathbf{S}} \Psi(\mathbf{r}, E, \hat{\Omega}) = \int \int \Sigma_s(\mathbf{r}, \hat{\Omega} \cdot \hat{\Omega}', E' \rightarrow E) \Psi(\mathbf{r}, E', \hat{\Omega}') dE' d\hat{\Omega}'$$

Splitting the fission source yields the dominance ratio of the system as (5.2)

$$\rho' = \frac{k_e - k_0}{k_e - k_1} \rho. \quad (5.2)$$

The eigenvalues are selected so that $k_e > k_0 > k_1$ holds. The Wielandt method has already been implemented in **MCNP** [45], [46]. Unfortunately this implementation is not publicly

available and an implementation from scratch was realised in this work. Since in Monte Carlo codes no matrix equations are used the implementation of the method, relies on the insight of how the fission reaction is simulated. If fission occurs, the neutron path is terminated and N_f fission neutrons (5.3) are stored in the fission bank array

$$N_f = w \frac{\nu \Sigma_f}{\Sigma_t k_{\text{eff}}} + \xi. \quad (5.3)$$

Here $0 \leq \xi \leq 1$ is a random number. Only during the next criticality cycle those neutrons are retrieved. Each neutron is started from the fission bank with uniformly sampled direction. The energy is determined from a fission spectrum distribution immediately after starting the history. In [46] a fixed source calculations has been used to track all the starting fission neutrons and their progenies. Therefore, the criticality cycles are replaced by consecutive fixed source runs. The most efficient implementation has been proposed in [45] and was implemented in the current work. The idea is to monitor the fission events. Each time when a fission event occurs, a flag is lifted by **MCNP**. At this point a reduced number of fission neutrons N_R (5.4) is stored in the fission bank

$$N_R = w \frac{\nu \Sigma_f}{\Sigma_t} \left(\frac{1}{k_{\text{eff}}} - \frac{1}{k_e} \right) + \xi. \quad (5.4)$$

This corresponds to the splitting of the fission source from the right hand side of (5.1). The rest of the neutrons given by (5.5) are stored in the memory and run within the current cycle

$$N_C = w \frac{\nu \Sigma_f}{\Sigma_t k_e} + \xi. \quad (5.5)$$

The Wielandt acceleration was originally developed to accelerate the power iteration method for finding matrix eigenvalues. Given the eigenvalue problem (5.6)

$$\mathbf{A}\mathbf{x} = \lambda\mathbf{x}, \quad (5.6)$$

one can shift the spectrum by σ to obtain (5.7)

$$(\mathbf{A} - \sigma\mathbf{I})\mathbf{x} = (\lambda - \sigma)\mathbf{x}. \quad (5.7)$$

This modifies the power iteration to compute the eigenvalues of the shifted operator $\mathbf{B} = \mathbf{A} - \sigma\mathbf{I}$. In this case, the convergence rate is determined by the ratio

$$\left| \frac{\lambda_1 - \sigma}{\lambda_0 - \sigma} \right|. \quad (5.8)$$

Following numerical tests, it was determined that the best results are obtained when the N_C neutrons, are continued with random position and energy independently sampled from a fission distribution. Due to the additional N_C neutrons, the computational time is increased. As it might be deduced from (5.4) and (5.5) in the limit $k_e \rightarrow k_{\text{eff}}$ the computational effort

will increase. The effect of the extra fission neutrons contributing to current cycle can be estimated directly based on (5.1) [47]. Using the convention $\hat{\mathbf{L}} = \hat{\Omega} \cdot \nabla + \Sigma_t(\mathbf{r}, E)$ the neutron transport equation can be written in compact operator form

$$\begin{aligned} \left(\hat{\mathbf{L}} - \hat{\mathbf{S}} - \frac{\hat{\mathbf{F}}}{k_e} \right) \Psi &= \left(\frac{1}{k_{\text{eff}}} - \frac{1}{k_e} \right) \hat{\mathbf{F}} \Psi, \\ \left(\hat{\mathbf{L}} - \hat{\mathbf{S}} - \frac{\hat{\mathbf{F}}}{k_e} \right) \Psi &= \frac{\hat{\mathbf{F}}}{k_w} \Psi. \end{aligned} \quad (5.9)$$

Inverting the left hand side of (5.9) one obtains

$$\begin{aligned} \Psi &= \left(\hat{\mathbf{L}} - \hat{\mathbf{S}} - \frac{\hat{\mathbf{F}}}{k_e} \right)^{-1} \frac{\hat{\mathbf{F}}}{k_w} \Psi, \\ \Psi &= \left(\left(\hat{\mathbf{L}} - \hat{\mathbf{S}} \right) \left(1 - \frac{(\hat{\mathbf{L}} - \hat{\mathbf{S}})^{-1} \hat{\mathbf{F}}}{k_e} \right) \right)^{-1} \frac{\hat{\mathbf{F}}}{k_w} \Psi, \\ \Psi &= \left(1 - \frac{(\hat{\mathbf{L}} - \hat{\mathbf{S}})^{-1} \hat{\mathbf{F}}}{k_e} \right)^{-1} (\hat{\mathbf{L}} - \hat{\mathbf{S}})^{-1} \frac{\hat{\mathbf{F}}}{k_w} \Psi. \end{aligned} \quad (5.10)$$

In the limit $k_e \rightarrow \infty$ from (5.10) the usual expression for the criticality power iterations is obtained

$$\Psi = (\hat{\mathbf{L}} - \hat{\mathbf{S}})^{-1} \frac{\hat{\mathbf{F}}}{k_{\text{eff}}} \Psi. \quad (5.11)$$

The above expression can be expanded in power series

$$\begin{aligned} \Psi &= \left(\frac{1}{k_e} + \frac{(\hat{\mathbf{L}} - \hat{\mathbf{S}})^{-1} \hat{\mathbf{F}}}{k_e} + \left(\frac{(\hat{\mathbf{L}} - \hat{\mathbf{S}})^{-1} \hat{\mathbf{F}}}{k_e} \right)^2 + \left(\frac{(\hat{\mathbf{L}} - \hat{\mathbf{S}})^{-1} \hat{\mathbf{F}}}{k_e} \right)^3 + \dots + \right) \frac{(\hat{\mathbf{L}} - \hat{\mathbf{S}})^{-1} \hat{\mathbf{F}}}{k_w} \Psi, \\ \Psi &= \left(\frac{1}{k_e} + \frac{(\hat{\mathbf{L}} - \hat{\mathbf{S}})^{-1} \hat{\mathbf{F}}}{k_e} + \left(\frac{(\hat{\mathbf{L}} - \hat{\mathbf{S}})^{-1} \hat{\mathbf{F}}}{k_e} \right)^2 + \left(\frac{(\hat{\mathbf{L}} - \hat{\mathbf{S}})^{-1} \hat{\mathbf{F}}}{k_e} \right)^3 + \dots + \right) \frac{k_{\text{eff}}}{k_w} \Psi, \end{aligned} \quad (5.12)$$

where in the last expression (5.11) is inserted. The expected number of extra neutrons produced in the current cycle is obtained by taking the contribution k_e^{-1} and integrating over the entire phase space (5.13)

$$N_{\text{extra}} = \int_{V_{\text{phase}}} \left(\frac{1}{k_e} + \frac{(\hat{\mathbf{L}} - \hat{\mathbf{S}})^{-1} \hat{\mathbf{F}}}{k_e} + \left(\frac{(\hat{\mathbf{L}} - \hat{\mathbf{S}})^{-1} \hat{\mathbf{F}}}{k_e} \right)^2 + \dots + \right) \frac{k_{\text{eff}}}{k_e} \Psi dE d\hat{\Omega} d\mathbf{r}, \quad (5.13)$$

$$N_{\text{extra}} = \left(\frac{k_{\text{eff}}}{k_e} + \left(\frac{k_{\text{eff}}}{k_e} \right)^2 + \left(\frac{k_{\text{eff}}}{k_e} \right)^3 + \dots + \right).$$

Therefore, the expected number of neutrons per history N is given by

$$N = 1 + N_{\text{extra}} = \frac{1}{1 - \frac{k_{\text{eff}}}{k_e}}. \quad (5.14)$$

According to (5.14) the expected number of neutrons per history will increase in the limit $k_e \rightarrow k_{\text{eff}}$ and as expected $N \rightarrow 1$ as $k_e \rightarrow \infty$. This is a plausible result, since if no shift is present only one neutron is expected to be run within a single history. This effect was observed when running the modified version of **MCNP**, where with shifts of 900 pcm, run times were observed to increase by seven times. Therefore, the efficiency of the method has to be investigated in detail. To test the efficiency of the calculation, the figure of merit (FOM) was computed and compared for different values of k_{eff} . The figure of merit is a standard parameter for estimating the calculation efficiency. Usually, the estimated relative error Re^2 is proportional to $1/N$, where N is the number of histories. The relative error is defined in the introduction chapter and is given by equation (3.25). On the other hand the computational time T , is proportional to the number of histories N . Therefore, the product (5.15) is approximately constant for a given calculation.

$$\text{FOM} = \frac{1}{\text{Re}^2 T} \quad (5.15)$$

The aim is to have the FOM as large as possible. Since the performance of the method over all tally bins is of interest, a modified FOM (5.16) as has been proposed in [48] is used

$$\text{FOM} = \frac{N_{\text{BINS}}}{T \sum_k \text{Re}_k^2}. \quad (5.16)$$

The summation in (5.16) runs over all the tally bins. The aim is to maximize the FOM, this however, might lead to larger spatial averages of the relative error. Situation difficult to detect using only equation (5.16). Therefore, in [49] the standard deviation σ_{Re} for the relative error set Re_k has been introduced (5.17)

$$\sigma_{Re} = \sqrt{\frac{1}{N_{\text{BINS}}} \left\{ \sum_k^{N_{\text{BINS}}} Re_k^2 - \frac{1}{N_{\text{BINS}}} \left(\sum_k^{N_{\text{BINS}}} Re_k \right)^2 \right\}}. \quad (5.17)$$

5.2 Testing the performance of the Wielandt method

As a test case a 1/4 PWR core was used. The geometry plot is included in fig. 5.1. Since the aim is to test the numerical performance, a simplified fuel composition was used, explaining the larger than unity eigenvalue. Pin by pin calculation with each pin divided into 20 axial nodes was run. 1.0×10^6 neutrons per cycle were simulated. Reflective boundary conditions were assigned for the symmetry cut boundaries. Void condition was used for all other boundaries. Each calculation was started with a homogeneous fission source over all the fuel assemblies. The choice of volumetric source distribution is motivated by the fact that starting with a single or limited number of source points will put the convergence of the reference calculation in serious jeopardy. This will make the comparison with the Wielandt method meaningless.

The test calculations are summarized in table 6.4. Clearly both the FOM and σ_{Re} are improved as $k_e \rightarrow k_{\text{eff}}$. It is also important to note that all the eigenvalues are very close to each other. This clearly shows that the method was properly implemented. From the same table, the rapid acceleration of the H_{src} convergence is evident. This is a considerable improvement in terms of source convergence and the number of initial skipped cycles needed to converge the source distribution.

Table 5.1: Performance of Wielandt acceleration method for different k_e showing the reduction of cycles needed to converge the fission source distribution.

Shift k_e	Eigenvalue k_{eff}	FOM	σ_{Re}	H_{src} convergence
∞	1.15099 (1)	25.2354 (6)	9.23724E-03 (5)	170 cycles
1.8	1.15098 (2)	51.4265 (5)	5.53555E-03 (6)	60 cycles
1.3	1.15098 (1)	82.5184 (6)	3.05351E-03 (6)	23 cycles
1.22	1.15097 (1)	88.2289 (6)	2.06565E-03 (6)	12 cycles
1.16	1.15098 (1)	87.2289 (6)	1.25620E-03 (6)	7 cycles

To further demonstrate the power of the method, consider the following figure fig. 5.2 showing plots of H_{src} versus criticality cycle.

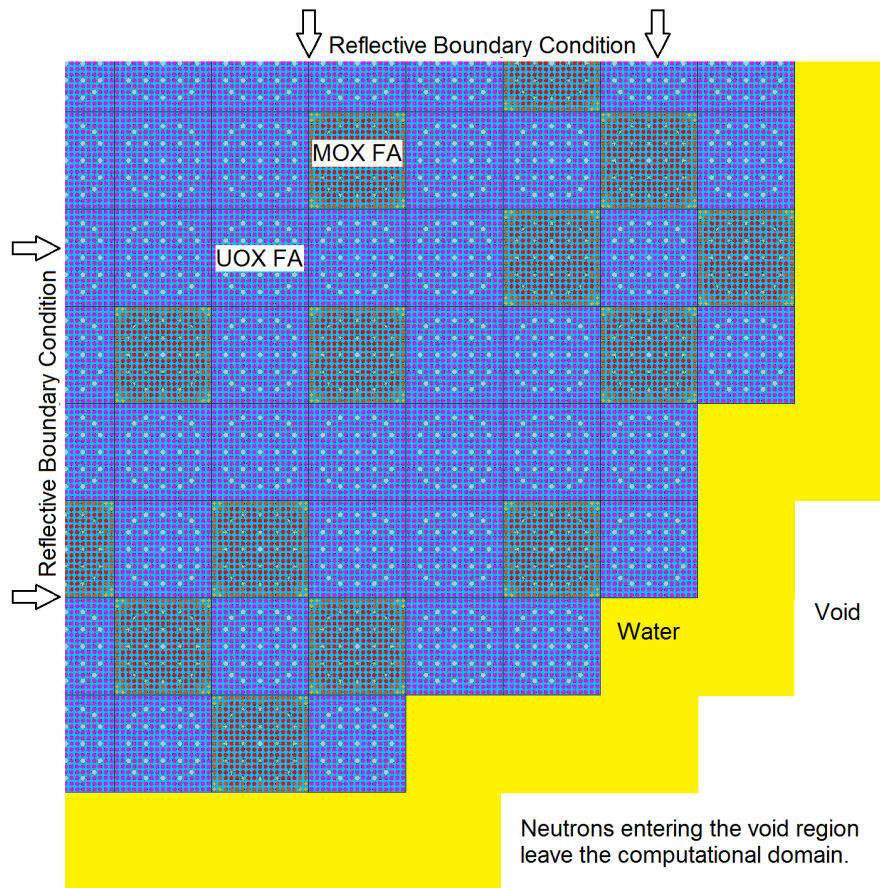


Figure 5.1: Quarter PWR core geometry loaded with MOX and UOX fuel assemblies, denoted by (MOX FA) and (UOX FA). The computational geometry is surrounded by water volume serving the role of neutron reflector.

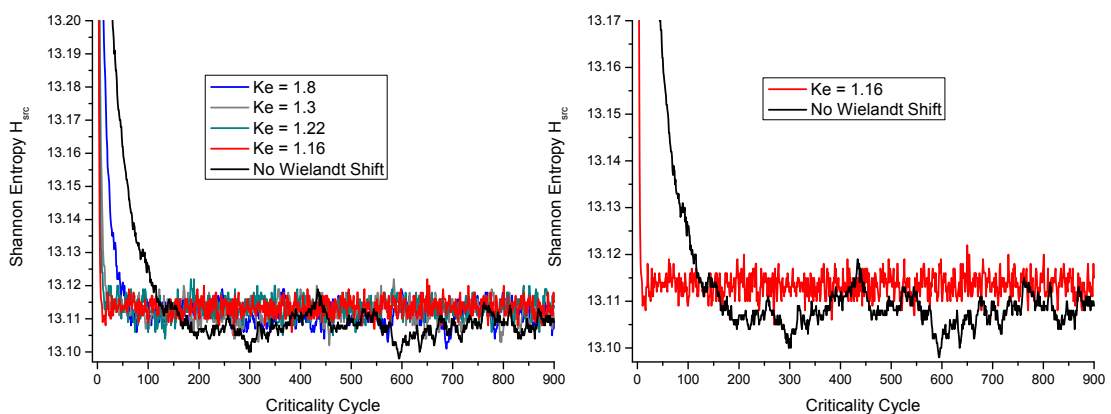


Figure 5.2: H_{src} vs. criticality cycle for different values of k_e and H_{src} vs. criticality cycle for the cases $k_e = \infty$ and $k_e = 1.16$ illustrating the reduction of the cycles needed for converging the source entropy.

As evident from the right hand side of the plot, H_{src} for the reference case shows clear trends of regions with positive and negative slope. This is an undesired effect. As shown later, these oscillations will deteriorate the tallying procedure. The clear trend of accelerating the H_{src} convergence as $k_e \rightarrow k_{eff}$ is also observed.

Since geometry having diagonal symmetry is dealt with, it is to be expected that the same symmetry argument holds for the tallies. To qualify this result consider the notion of power tilt for a particular axial node k defined via (5.18)

$$T_{i,j}^k = 100 \times \frac{|F_{i,j,k} - F_{j,i,k}|}{F_{i,j,k}}, \quad (5.18)$$

for all $i > j$.

Define further the maximal value for the power tilt $T_{i,j}^k$ for axial node k by (5.19)

$$\|\mathbf{T}_k\| = \max_{i,j} T_{i,j}^k. \quad (5.19)$$

In the ideal case $\|\mathbf{T}_k\| = 0$, although due to the statistical nature of the code and convergence issues associated with the power iteration this does not hold. Therefore, an effective method to accelerate the convergence of the source should force $\|\mathbf{T}_k\|$ to zero. Different test calculations were done starting with a reference calculation and varying $k_e \rightarrow k_{eff}$. The values of $\|\mathbf{T}_k\|$ calculated for the twenty axial nodes, as well as the mean $\mu(T_{i,j}^k)$ and standard deviation $\sigma(T_{i,j}^k)$ are summarized in table 5.2.

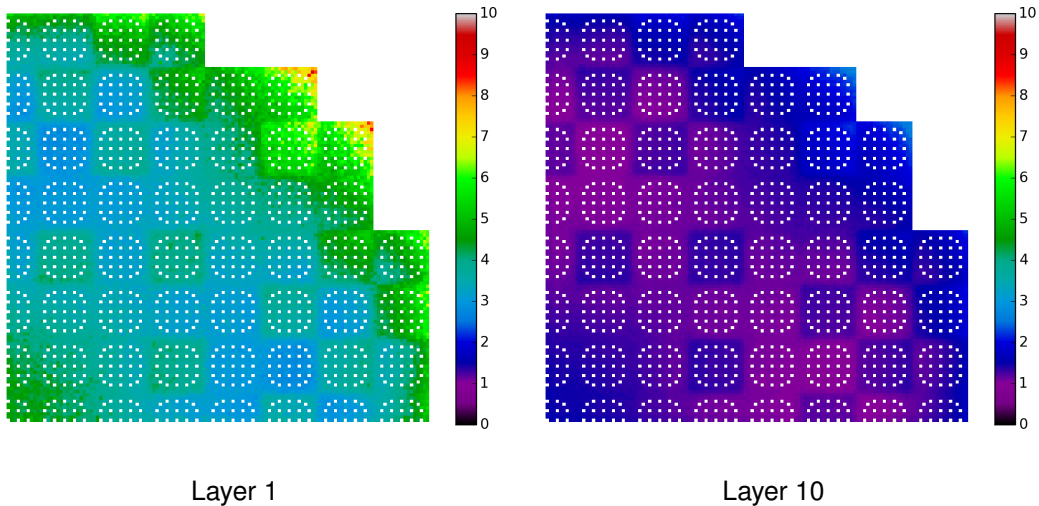


Figure 5.3: Two dimensional plot of the relative error of the fission heat deposition distribution in % for the case $k_e = \infty$. Each point represents the value of the relative error for a single fuel pin.

Table 5.2: Table showing the suppression of the unphysical tally asymmetry for the ten axial planes of the problem shown as a function of the shift eigenvalue k_e . Shown are the maximum tilt $\|\mathbf{T}_k\|$, its corresponding mean value $\mu(T_{i,j}^k)$ and standard deviation $\sigma(T_{i,j}^k)$ estimated over all pin cells having positions i and j for a certain axial level k .

Axial node k	$k_e = \infty$			$k_e = 1.8$			$k_e = 1.3$			$k_e = 1.22$			$k_e = 1.17$			$k_e = 1.16$		
	$\ \mathbf{T}_k\ $	$\mu(T_{i,j}^k)$	$\sigma(T_{i,j}^k)$															
1	43.11	4.73	3.81	19.58	2.87	2.36	8.67	1.60	1.24	5.98	1.10	0.87	3.31	0.60	0.47	2.11	0.42	0.34
2	17.26	2.93	2.34	11.88	1.82	1.44	5.99	0.99	0.78	5.31	0.71	0.55	2.63	0.39	0.30	1.25	0.26	0.21
3	14.86	2.37	1.90	10.64	1.48	1.18	5.56	0.82	0.65	4.25	0.57	0.44	2.21	0.31	0.24	1.31	0.21	0.17
4	11.20	2.10	1.66	8.45	1.24	0.99	4.07	0.69	0.56	3.58	0.49	0.39	1.98	0.27	0.21	1.25	0.18	0.15
5	10.64	1.83	1.45	6.41	1.10	0.88	5.87	0.63	0.51	2.47	0.44	0.35	1.53	0.24	0.19	1.36	0.16	0.13
6	9.88	1.71	1.35	5.69	1.03	0.79	3.59	0.59	0.47	2.88	0.43	0.34	1.16	0.22	0.18	1.06	0.15	0.12
7	9.23	1.60	1.27	6.45	0.97	0.78	4.55	0.55	0.44	2.72	0.39	0.31	1.32	0.21	0.17	0.92	0.15	0.12
8	9.69	1.57	1.27	5.71	0.96	0.75	3.64	0.55	0.44	2.25	0.39	0.30	1.53	0.20	0.16	0.85	0.14	0.11
9	8.99	1.56	1.25	5.80	0.96	0.76	2.93	0.52	0.42	2.72	0.37	0.30	1.15	0.19	0.15	0.97	0.14	0.11
10	11.40	1.55	1.24	5.89	0.93	0.74	3.06	0.51	0.41	2.40	0.38	0.30	1.04	0.19	0.15	1.07	0.14	0.11
11	10.01	1.61	1.29	6.99	0.93	0.73	3.62	0.51	0.40	2.52	0.37	0.30	1.13	0.19	0.15	0.98	0.13	0.11
12	11.92	1.64	1.33	6.39	0.96	0.75	2.83	0.51	0.40	2.12	0.37	0.30	1.16	0.19	0.15	0.87	0.14	0.11
13	12.96	1.75	1.40	5.55	1.00	0.81	3.64	0.54	0.43	2.49	0.38	0.31	1.17	0.20	0.16	0.84	0.14	0.11
14	9.39	1.80	1.40	7.56	1.11	0.84	3.58	0.57	0.45	2.23	0.42	0.33	1.29	0.21	0.16	1.04	0.15	0.12
15	13.81	1.90	1.52	5.87	1.16	0.88	3.85	0.58	0.45	2.59	0.45	0.35	1.58	0.23	0.18	1.06	0.16	0.12
16	12.82	2.04	1.62	6.30	1.18	0.93	3.52	0.63	0.51	2.92	0.49	0.39	1.40	0.25	0.19	1.10	0.16	0.13
17	14.05	2.15	1.73	6.61	1.27	1.02	4.03	0.70	0.55	2.74	0.54	0.42	2.38	0.27	0.21	1.16	0.18	0.15
18	18.95	2.51	2.01	8.57	1.44	1.13	6.40	0.79	0.63	4.37	0.61	0.48	2.04	0.31	0.24	1.10	0.21	0.17
19	16.82	3.07	2.44	12.96	1.84	1.49	7.57	0.99	0.79	4.78	0.74	0.59	2.75	0.37	0.30	1.55	0.26	0.21
20	32.06	4.78	3.84	18.82	2.85	2.29	11.24	1.60	1.27	6.23	1.13	0.88	3.71	0.61	0.49	2.10	0.41	0.33

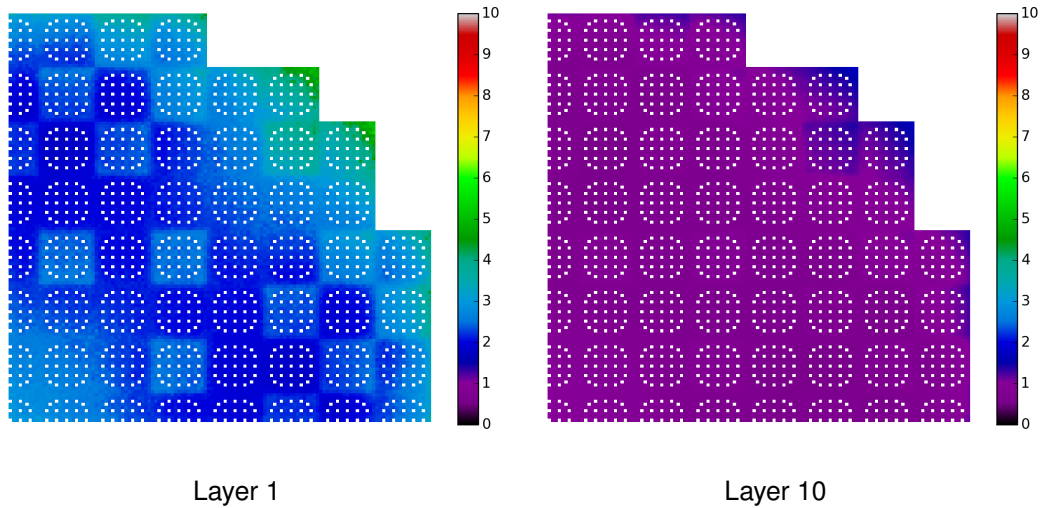


Figure 5.4: Two dimensional plot of the relative error of the fission heat deposition distribution in % for the case $k_e = 1.8$. Each point represents the value of the relative error for a single fuel pin.

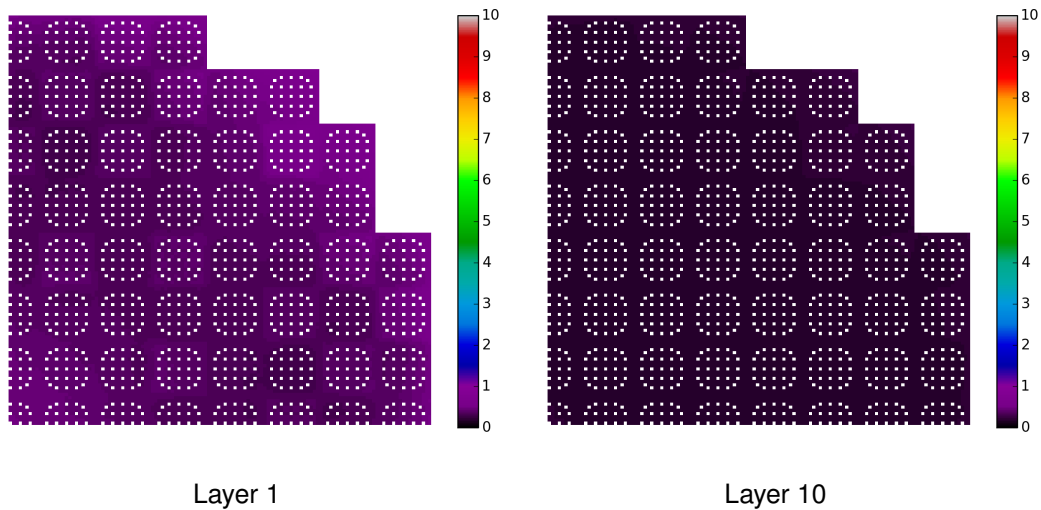


Figure 5.5: Two dimensional plot of the relative error of the fission heat deposition distribution in % for the case $k_e = 1.16$. Each point represents the value of the relative error for a single fuel pin.

Clearly the Wielandt method improves all three parameters $\|\mathbf{T}_k\|$, $\mu(T_{i,j}^k)$ and $\sigma(T_{i,j}^k)$. The large values of $\|\mathbf{T}_k\|$ for the first and the last node can be explained with the poor statistics due to the neighboring vacuum boundaries causing low cell population. In particular, the fission heat deposition in those cells is eleven times smaller than in the middle of the core. Most notably this problem is visible in the case of the standard **MCNP** calculation ($k_e = \infty$). In this case, $\|\mathbf{T}_k\|$ has very large values. These are insulated cases occurring only for small number of tally bins. The rarity of these events is most clearly shown by the values of $\sigma(T_{i,j}^k)$. The values of $\mu(T_{i,j}^k)$ give more information about the general behavior. For

the case of the standard **MCNP** calculation $\mu(T_{i,j}^k)$ is bigger than the associated statistical uncertainty (1 %). This is a clear problem, arising due to the biased fission source and convergence issues of the power iteration. The same table shows the reduction of the power tilt in the limit $k_e \rightarrow k_{\text{eff}}$. Having in mind that the statistical uncertainty in the upper and lowermost axial levels is on the order of magnitude of 1 %, all the runs using the Wielandt method are able to reduce the mean value of the power tilt to levels within the statistical uncertainty of the calculation. Clearly judging based on the computer run time alone, one can not effectively estimate the efficiency of the method. Moreover this comparison is not very meaningful, since a fast running calculation that gives erroneous results is compared to a time consuming high fidelity calculation. It should be also taken into account that to produce results of the same quality as the Wielandt scheme, a significant increase in the number of histories per criticality cycle would be needed. Later in this thesis, based on the fission matrix eigenvalues, it will be shown that the Wielandt method actually reduces the dominance ratio of the problem. This theoretical prediction will be demonstrated on an actual calculation. The modified power iteration has completely different convergence behavior when compared to the analog calculation. This is why a simple increase of the particle population will be a very inefficient method of achieving the improvements due to the application of the spectrum shift.

The most important question is to determine whether the Wielandt method introduces a bias in the **MCNP** calculation. This can be obtained by comparing it to unmodified **MCNP** calculation. According to the theoretical description of the method, equal eigenfunctions are to be expected. Clearly the analog calculation ($k_e = \infty$) from table 5.2 has to be improved to ensure meaningful comparison. This was done by increasing the number of histories simulated per cycle to 2.0×10^6 and running two **MCNP** iterations with a total of 240 recordings of the fission source. For the initial source guess of the first iteration, the source from the run with $k_e = 1.118$ was used. The multiple recordings of the fission source were done to ensure that the reference calculation will start from a well converged fission source having sufficient number of starting neutrons. Doing this over two iterations is assumed to improve the results even further. H_{src} convergence was reported after the first cycle for both runs. To mitigate any potential bias, twenty skipped cycles were done before tallying was started. Following this strategy, a consistent reference calculation is to be expected. To quantify the difference between the runs having $k_e = \infty$ and $k_e = 1.18$. Define the following operator for a particular axial node by (5.20)

$$\Delta_{i,j}^k = 100 \times \frac{(F_{i,j,k}^{k_e=1.16} - F_{i,j,k}^{k_e=\infty})}{F_{i,j,k}^{k_e=1.16}}. \quad (5.20)$$

The maximal value of (5.20) is given by (5.21)

$$\|\Delta_k\| = \max_{i,j} \Delta_{i,j}^k. \quad (5.21)$$

The results are summarized in table 5.3. The statistical uncertainty of $\|\Delta_k\|$ was propagated using partial derivatives. The values in the table clearly show that both methods deliver

results that are on average close to each other. This is most clearly shown by the small mean $\mu(\Delta_{i,j}^k)$ and the small standard deviation $\sigma(\Delta_{i,j}^k)$. Never the less, the maximal difference between the two methods is bigger than the statistical uncertainty of $\Delta_{i,j}^k$. This difference has many reasons, firstly, the analog calculation has very large statistical uncertainties in the top and the bottom nodes and near the core lateral boundaries. Secondly, the Wielandt method makes the system more tightly coupled. This tight coupling due to the reduced dominance ratio significantly improves the performance of the power iteration. This is most clearly shown by observing the unphysical tilt present in the fission heat deposition shown in table 5.2. It should be also taken into account that the two fold increase of the number of histories in the case of the analog calculation was not able to match the performance of the Wielandt method.

Table 5.3: Maximal relative difference between analog and calculation and the Wielandt shift method.

Axial node k	$\ \Delta_k\ $	$\mu(\Delta_{i,j}^k)$	$\sigma(\Delta_{i,j}^k)$	Uncertainty $\ \Delta_k\ $
1	13.01	2.01	1.61	6.18662
2	8.00	1.31	1.03	4.25235
3	6.82	1.05	0.83	3.66962
4	6.90	0.92	0.73	2.96174
5	6.76	0.83	0.66	2.00374
6	7.06	0.75	0.59	2.03529
7	5.59	0.71	0.57	2.63148
8	4.29	0.69	0.54	1.57568
9	4.77	0.68	0.54	1.85162
10	4.01	0.67	0.53	1.71043
11	5.35	0.66	0.53	2.03951
12	4.65	0.68	0.54	1.78572
13	4.17	0.72	0.57	1.53779
14	5.09	0.74	0.58	1.42600
15	5.10	0.78	0.61	1.97829
16	5.70	0.82	0.65	2.41210
17	5.42	0.89	0.71	2.37587
18	6.23	1.04	0.82	3.16876
19	11.41	1.34	1.07	3.77037
20	14.53	2.05	1.64	5.00285

Summarizing the results from the comparisons shown in this chapter one can deduce that the Wielandt method improves both the tally spacial distribution and the convergence of H_{src} . Moreover the results are becoming better as $k_e \rightarrow k_{eff}$.

If the practical side of the calculations is to be considered, it should be pointed out that very small shifts lead to very extensive computing times. This is a serious deficiency. A more practical approach is to use the Wielandt acceleration only to converge the initial source and disable it during the active cycles. This solution, however will not produce as symmetric results as those presented in table 5.2 because the active cycles will be simple analog power iteration. In the chapter on variance reduction, it will be shown that by using nonanalog transport it is possible to achieve results that are on average very close to those produced

by the Wielandt shift method within reasonable run time. The parameter k_e does not need to be a constant. The constant k_e should be guessed. If one knows the true eigenvalue of the system, the value of k_e can be adequately chosen. A possible strategy is to run a calculation with no tallying just to estimate k_{eff} and then define the corresponding shift eigenvalue. The shift can be also defined from previous run, as it will become apparent when the coupling to thermal hydraulics will be discussed. A more flexible and general approach is implemented using

$$k_e^i = k_{\text{eff}}^i + \Delta_i. \quad (5.22)$$

The parameter Δ_i , changes over the criticality cycles and is defined such so that k_e approaches k_{eff} from above. Here, the index i is a running index denoting the criticality cycles. Due to practical considerations too small Δ_i should be avoided. Therefore, some minimal value for Δ_i should be imposed.

Accelerated flux tallying in MCNP

Although parallel execution of Monte Carlo calculation is very common, the reasons behind the limited parallel efficiency are not sufficiently pointed out as modern general-purpose Monte Carlo codes are still not effective for massively parallel reactor criticality calculations. Therefore, in this chapter a number of essentials with regard to flux and fission heat deposition tallying that improve the parallel Monte Carlo calculation are discussed.

In this thesis Monte Carlo codes are coupled to subchannel analysis codes. Therefore, the axial distribution of the fission heat deposition for each fuel pin needs to be computed (tallied). The large number of fuel pins present in a light water reactor core makes the estimation of the fission heat deposition very complicated. To solve this task one has to simultaneously improve the algorithm used for accumulating the tallies and to provide adequate variance reduction techniques so that the Monte Carlo variance is kept within acceptable limits. In this chapter a newly developed strategy for improving the numerical performance of the tally estimators is presented. It is shown that by exploiting the geometry structure of a nuclear reactor core a very efficient tallying algorithm, specially designed to treat reactor core geometries, can be realised.

Since all the calculations presented in this thesis are run on large scale parallel computer architectures, the communication between the individual parallel processes among which the calculation is divided, causes significant slowdown. Each time when communication between the processes is executed, the code stops running and waits until all messages have been distributed. This communication latency is one of the main reasons for deteriorating the performance of parallel computer codes. Therefore, it has to be avoided if possible. Reducing the variance of the Monte Carlo estimates will be presented in Chapter 7.

The methods presented hereafter, focus on the acceleration of the tallying by optimizing the computer memory usage and reducing the communication overhead of the parallel computation. This is achieved by the implementation of a novel scheme to store the spatial bins of the tally estimates and by reducing the communication between the individual processes that comprise the parallel calculation. The later realises on the fact that the tally estimates are integral quantities, accumulated as a side product of the transport calculation, that can

be collected after the transport has finished.

6.1 Fission heat and flux estimators in **MCNP**

MCNP offers two types of general purpose tallies to tally volume integrated flux i.e. cell and mesh based tallies [25]. In this work the cell averaged tallies estimated with the track length estimator are to be discussed eq. (3.21). The cell based tallies are impractical to use for repeated structure geometries. To define the core geometry, **MCNP** uses a repeated structure representation, consisting of multiple levels of embedded lattices. The first level in this case is the pin unit cell with the cladding, coolant and fuel cells. The second level is the lattice defining the fuel pin location within the assembly lattice. The third level is the lattice defining the fuel assembly loading pattern. To include all fuel pins **MCNP**, stores each unit cell with its repeated structure indices together with the repeated structure indices of the assembly it belongs to. If a three dimensional geometry is to be considered the axial location needs to be included. It is known from practical experience that the computing time increases almost linearly with the number of tally bins. Therefore, using the cell based tallies is not advisory for large repeated structure geometries.

To solve this problem **MCNP** offers the mesh tally option. This option introduces a mesh superimposed over the geometry. The quantity of interest is tallied in each mesh element. In this case, the spacial tally bins are relatively easy to determine. Usually a single mesh cell might encompass different material regions, therefore, tracks corresponding to different material regions cannot be estimated separately. When tallying fission heat deposition, this deficiency is compensated since fission is possible only in the fuel pellet and all other regions will not contribute to the score. Although it is very efficient when compared to the cell tallies, the mesh tally slows down the criticality calculation significantly and further optimization is need.

The primary quantity of interest, the fission heat deposition is given by

$$H = \int_V \int_0^{\infty} \sum_n Q_n N_n(\mathbf{r}) \sigma_{f,n}(\mathbf{r}, E) dE d\mathbf{r}. \quad (6.1)$$

All tallies in **MCNP** are normalized per one source neutron and the resulting flux unit is $\text{cm}^{-2}\text{source-neutron}^{-1}$ rather than the usual unit of $\text{cm}^{-2}\text{s}^{-1}$. ,therefore, it is not accurate to call (6.1) power.

To overcome the deficiencies of the mesh tally, a new tallying approach was implemented in **MCNP**. It consists of optimizing the spatial bin structure and improving the scalability by reducing the communication between the parallel tasks.

6.2 Data locality and bin structure optimization

To run operations the computer processor needs instructions and data that are supplied to it and stored in the main memory. With the increase of the processor speed the delays in transmitting data between the memory and the processor have become a serious issue. The processor operates faster than the memory, so it must wait while the proper segment of the memory is located and read. To overcome this delays, the computer uses multiple levels of fast memory called cache. They are used to acquire and store data from frequently used memory locations. The information from the main memory is copied in the cache in blocks of fixed size called cache lines. If the processor is not able to find the data it needs in the cache (cache miss), it has to search for it in the much slower main memory. To make room for the data that needs to be copied upon a cache miss, the processor has to predict which existing cache entry is least likely to be used in the future. The problem is that the cache can usually hold only few hundred kilobytes of data. Arrays that are used to store the data accumulated by the Monte Carlo code, in particular the tallies, are stored as a continuous contingent in the main memory. They can have sizes easily exceeding the cache capacity. Therefore, if the processor has to 'jump' over large portions of a big array, that don not fit in the cache, it will suffer many cache misses and this will slow down the computation. This can occur if the tally bins are stored in a way in which the code needs to jump over large portions of the array when the neutron goes from one cell to the other.

The strategy of improving the performance of the track length estimator is to use as much as possible the geometric information already available in **MCNP** and store the information in a compact form, so that the cache memory management can operate efficiently.

In reactor physics calculations one deals with repeated structure geometries. Usually a core mesh containing the assemblies is defined. In addition, a second lattice defining the individual pin ordering is defined. Therefore, one can use this information to build a mesh structure (6.2)

$$\begin{aligned}
 M_I &= I_A + I_C \times N_P \\
 M_J &= J_A + J_C \times N_P. \\
 M_K &= K_A
 \end{aligned}
 \tag{6.2}$$

The indexes from (6.2) are defined in the following table table 6.1.

Table 6.1: Description of the indexes used to describe the location of a particular cell in the core geometry.

M_I		Mesh index for the x direction
M_J		Mesh index for the y direction
M_K		Mesh index for the z direction
I_A	$[1 : N_P]$	Assembly lattice index for the x direction
J_A	$[1 : N_P]$	Assembly lattice index for the y direction
K_A		Assembly lattice index for the z direction
K_A	$[1 : N_{axial}]$	Assembly lattice index for the z direction
I_C	$[1 : N]$	Core lattice index for the x direction
J_C	$[1 : M]$	Core lattice index for the y direction.

Using this structure one can define a 3D mesh. The resulting 3D array can be stored in unrolled form using the following formula (6.3)

$$[x, y, z] = x + \text{WIDTH} * (y + \text{DEPTH} * z). \quad (6.3)$$

This strategy has a potential pitfall. Nonlocality is introduced by the index flattening scheme. Consider two pin cells located on top of each other belonging to the same assembly. These cells are close neighbors in the coordinate space. In the index space defined by (6.3) they are $\text{WIDTH} * \text{DEPTH}$ elements apart. This artificial nonlocality is undesirable. It makes cash searches ineffective especially when dealing with large meshes. One can explore the fact that the core and assembly indices define a 5D array structure and some geometric intuition to reduce the nonlocality can be applied. This methodology is hard to implement and is highly problem-dependent.

To resolve this problem the methodology of space filling (Peano) curves was introduced. A space filling curve realises a mapping between one dimensional space and some higher dimensional space $\mathbb{R}^1 \rightarrow \mathbb{R}^d$. Different curves of this type are known. In this work the Morton Z-curve [50] is used. The Z-curve maps, multidimensional data to one dimensional curve while preserving locality. The Z-order of a point is computed by interleaving the binary representation of its coordinates.

Example of the mapping from $\mathbb{R}^3 \rightarrow \text{Z-order}$ is given in table 6.3. Note that 4 bit integers were used for the coordinate indices.

Table 6.2: Z-ordering in three dimensional space. The integers representing the lattice indices are converted to binary form and used to determine the z-order by interleaving the binary representations.

I	Binary I	J	Binary J	K	Binary K	Z-ordered	Binary Z-ordered
1	0001	1	0001	1	0001	7	000111
1	0001	2	0010	3	0011	53	110101
3	0011	2	0010	2	0010	57	111001

To further clarify the idea and give a graphical explanation fig. 6.1 was included. Both the binary converted values and the z-ordering indices are given. The blue connecting line shows

the path traversed in \mathbb{R}^2 .

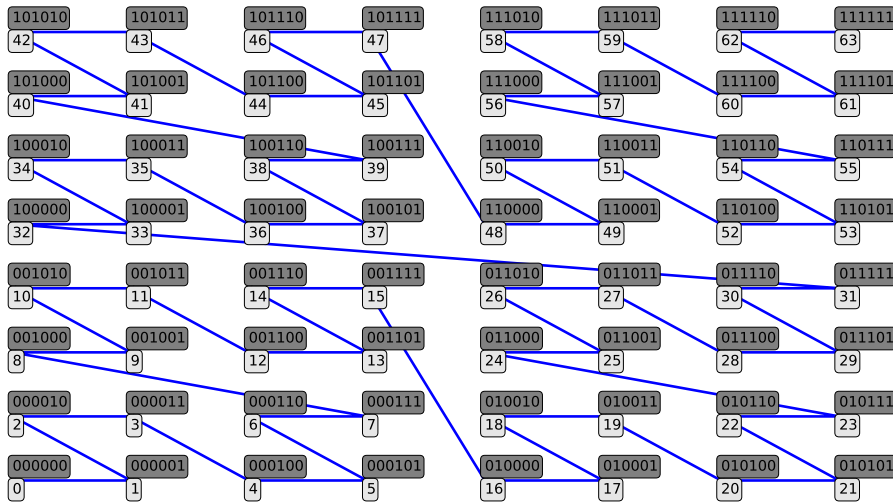


Figure 6.1: Z-ordering in \mathbb{R}^2 for a 8×8 lattice using the space filling technique according to Morton.

The most important consequence of this ordering is to preserve the locality of the data. To illustrate this consider table 6.3. Clearly the Z-ordering preserves the locality to a much larger degree than the usual mesh storage.

Table 6.3: Comparison of the z-ordering and the usual unrolled 3D array ordering, showing that the array storage is much more compact and is less likely to cause cache misses. I, J and K denote the coordinates used to describe the position in \mathbb{R}^3 .

I \in 0-127	J \in 0-127	K \in 0-19	\mathbb{R}^3 ordered	Z-ordered
7	7	1	17288	223
7	7	2	33672	251
7	8	1	17416	1101
7	9	1	17544	1103
9	7	1	17290	663
8	6	1	17161	660

6.3 Implementation in MCNP and performance testing

Modern high performance computers consists of individual computer nodes, connected trough fast interconnect network. Each computer node, consists of multiple processor cores that share common memory.

MCNP is usually run in a hybrid mode, using both shared memory and parallel memory programming models. The first level of parallelisation is done by splitting the computation

between processes that utilize distinct memory spaces. This is the so called distributed memory parallelisation. Each parallel process gets a unique identification and all processes together form a parallel communicator. One of the processes, usually the first according to the communicator numbering is called master and the other are designated as slaves. The master process is used to organize the communication, collect the results from the slaves and do file input output operations. These processes share information by communicating to each other by sending and receiving messages. As explained in the introduction to this chapter, this is undesirable and the amount of communication has to be minimized. Usually, one parallel process is placed on each computing node and the communication goes over the internodal interconnect. The second level of parallelisation is over shared memory, where the individual processes (threads) have access to the common memory. In this scenario, if one process modifies certain value, this affects all other processes. Therefore, it has to be ensured that no data races occur by ensuring that no two threads are trying to simultaneously update the same memory location. For instance, arrays are subdivided into different chunks corresponding to the individual threads. By doing so, each thread updates a separate portion of the array corresponding to its thread id **TID** fig. 6.2. The index **I** is determined by the Z-ordering. The thread id **TID** is the unique identifier assigned to each thread in the shared memory parallelisation model. The shared memory parallel model is used to utilize the parallel cores present within a single computing node. Shared memory parallelisation is done via the **openMP** library and the distributed memory parallelisation is done via the **MPI** library.

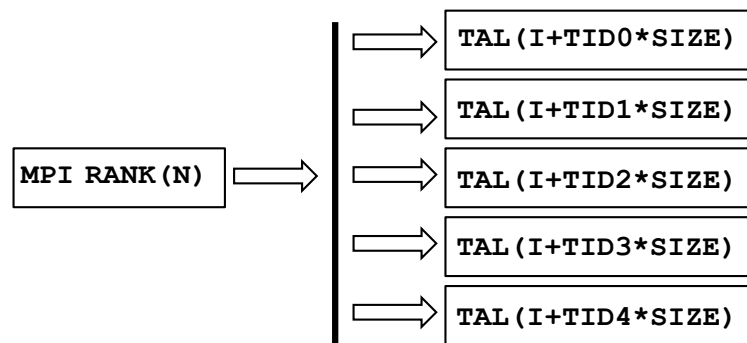


Figure 6.2: The strategy of splitting the arrays into chunks corresponding to the individual threads by offsetting the cell location index **I**.

The efficiency of the newly developed bin storage technique and the optimized communication strategy is tested by simulating a quarter three dimensional **PWR** core. The fission heat deposition (6.1) was tallied in each pin cell. Every pin was subdivided into 20 axial nodes.

To compare the efficiency of the tallying subroutine the run time was compared with the case where no tallying was done. A total of 2.6×10^5 tally volumes were used in the problem. As shown in table 6.4 the newly implemented methodology clearly outperforms the standard mesh tally. The test calculations were run on 240 parallel processors using MPI-OpenMP hybrid parallel model [51], [52].

Table 6.4: Numerical performance of the improved tallying methodology applied to a quarter PWR core. The same geometry as the one used for testing the Wielandt method is used.

No tallying	80.3 min
Standard mesh tally	117 min
Improved tally	83.2 min

It should be noted that the newly implemented tally subroutine preserves the mathematical definition of estimator and produces results completely identical to the usual cell and mesh tallies. The only variation that was observed was when estimating the relative error. Variations in the fourth decimal place were observed. This effect is due to the nondeterministic nature of the floating point operations.

The track length estimators have to be called for every track segment and the value $\nu \Sigma_f(\mathbf{r}, E)$ has to be computed and stored. Using the fact that the fission heat deposition occurs in cells with large densities, one can use the alternative collision estimator (6.4) [53]. As the name suggest, the collision estimator is scored only at collision sites and uses the same bin structure as the one developed for the track length estimator. In fact both estimators are included as alternative option in the newly developed tally routine. Using this method, the flux is estimated by the total number of collisions for N histories in the volume V divided by the total cross section. Here, the second sum runs over the sequence of collisions for history i in the volume V . $\zeta_{i,c}$ is the phase space vector for history i at collision event c .

$$\psi = \frac{1}{NV} \sum_{i=1}^N \sum_{c=1}^{C_i} \frac{w_{i,c}}{\Sigma_t(\zeta_{i,c})} \quad (6.4)$$

In addition, this less frequent invocation of the corresponding routines results in faster code execution. The results were compared with the usual track length estimator and the differences were within the statistical uncertainty of the estimates [1]. As seen from table 6.4 the improved track length estimator adds only an insignificant part to the total execution time. Therefore, the track length estimator was used in this work.

Implementation of the fission matrix technique in MCNP and higher order eigenpair analysis

In the introductory chapter, as well as in the chapter discussing the Wielandt acceleration scheme, the concept of the dominance ratio of the system is used. It is the ratio $\frac{k_0}{k_1}$, where k_0 and k_1 are the fundamental mode and first eigenvalue of the system. To gain a better qualitative insight in the convergence of the power iteration, the higher mode eigenpairs are needed. Only by explicitly calculating the dominance ratio it is possible to justify the application of the Wielandt shift. A decrease of the dominance ratio via shifting the eigenvalue spectrum can be demonstrated to reduce the dominance ratio and by doing so make remote parts of the geometry more tightly coupled. The fundamental mode eigenvalue k_0 is readily available from the Monte Carlo calculation. Since power iteration is used, estimating the higher mode eigenvalues and the corresponding eigenvectors is not possible with the standard Monte Carlo strategy. In general, to estimate the higher mode eigenvalues and their corresponding eigenvectors, deflation of the spectrum is needed. This is not possible with the standard Monte Carlo codes, since no negative weights are used. To estimate the higher mode eigenvalues and ultimately determine the dominance ratio of the system, the fission matrix formalism was implemented in **MCNP**. The fission matrix was computed for 2D and 3D geometries. Due to the large computer memory demand, the main limitation of the fission matrix is its spatial resolution.

7.1 The fission matrix technique in Monte Carlo criticality calculations

It is known from the theory of distributions that the classical solution of the eigenvalue problem (7.1)

$$\left(\hat{\mathcal{L}} - \lambda\right) y = f \quad (7.1)$$

Is given by (7.2) [54]

$$y(x) = \int_{x_1}^{x_2} G(x, x'|\lambda) f(x') dx'. \quad (7.2)$$

Where the $G(x, x'|\lambda)$ is the Green function satisfying

$$\left(\hat{\mathcal{L}} - \lambda\right) G(x, x'|\lambda) = \delta(x - x') \quad (7.3)$$

Defining (7.4)

$$\begin{aligned} \hat{\mathbf{X}}\Psi(\mathbf{r}, E, \hat{\Omega}) &= \hat{\Omega} \cdot \nabla \Psi(\mathbf{r}, E, \hat{\Omega}) + \Sigma_t(\mathbf{r}, E) \Psi(\mathbf{r}, E, \hat{\Omega}) - \\ &- \int \int dE' d\hat{\Omega}' \Sigma_S(\mathbf{r}, \hat{\Omega} \cdot \hat{\Omega}', E' \rightarrow E) \Psi(\mathbf{r}, E', \hat{\Omega}') \end{aligned} \quad (7.4)$$

$$\mathbf{S}(\mathbf{r}) = \int \int dE' d\hat{\Omega}' \nu \Sigma_f(\mathbf{r}, E') \Psi(\mathbf{r}, E', \hat{\Omega}')$$

the transport equation can be written in the following form (7.5)

$$\hat{\mathbf{X}}\Psi(\mathbf{r}, E, \hat{\Omega}) = \frac{1}{k} \frac{\chi(E)}{4\pi} \mathbf{S}(\mathbf{r}). \quad (7.5)$$

The Green function method can be applied to the transport operator (7.5) [55], [56]. The Green function is then defined by (7.6)

$$\hat{\mathcal{L}}G(\mathbf{r}', E', \hat{\Omega}' \rightarrow \mathbf{r}, E, \hat{\Omega}) = \delta(\mathbf{r}' - \mathbf{r}) \delta(E' - E) \delta(\hat{\Omega}' - \hat{\Omega}). \quad (7.6)$$

Where the primed variables denote the initial point in the phase space. The solution of (7.5) can be found by the Green function method (7.2) using (7.6) one obtains (7.7)

$$\Psi(\mathbf{r}, E, \hat{\Omega}) = \frac{1}{4\pi k} \int \int d\mathbf{r}' dE' d\hat{\Omega}' \chi(E') \mathbf{S}(\mathbf{r}') G(\mathbf{r}', E', \hat{\Omega}' \rightarrow \mathbf{r}, E, \hat{\Omega}). \quad (7.7)$$

Multiplying both sides of (7.7) by $\nu \Sigma_f$ and integrating $\int \int \dots dE' d\hat{\Omega}'$ the following integral equation for the fission source is obtained (7.8)

$$\mathbf{S}(\mathbf{r}) = \frac{1}{k} \int d\mathbf{r}' \mathbf{S}(\mathbf{r}') \hat{\mathbf{H}}(\mathbf{r}' \rightarrow \mathbf{r}). \quad (7.8)$$

This integral equation can be integrated using the Monte Carlo transport code. The problem is discretization, which is done by splitting up the region into a number of spatial domains V_i and accumulating $\mathbf{S}(\mathbf{r} \in \mathbf{V}_i)$. This discretization transforms (7.8) to a matrix equation of the form

$$\mathbf{S}_m^{(i)} = \frac{1}{k_{(i)}} \mathbf{S}_n^{(i)} \mathbf{H}_{n,m} \quad (7.9)$$

In general, the square matrix $\mathbf{H} \in \mathbb{R}^{n \times n}$ will have n eigenpairs. With k_0 being the fundamental mode eigenvalue. The continuous energy estimate of \mathbf{H} is in general not guaranteed

to be symmetric, therefore, real and complex eigenvalues are to be expected. Since the fundamental mode eigenvalue coincides with the estimate for k_{eff} , it should be real. Due to the small mean free path of the neutrons in a thermal reactor, the fission matrix should be sparsely populated. Indeed the neutrons born in one assembly would have the largest chance of causing fission within the same assembly or in its nearest neighbours (local fission). Therefore, only a small percentage of the matrix elements will be nonzero.

7.2 Numerical analysis of sparse eigenproblems

To compute the eigenpairs of the fission matrix, a suitable numerical algorithm capable of treating large asymmetric sparse eigenproblems has to be used. The logarithm of the fission matrix is shown in fig. 7.1. To tally the fission matrix, a 128×128 spatial mesh was overlaid over a 2D core slice. The dimensions of the fission matrix are $128^4 \times 128^4$. Morton ordering was used to store the matrix elements. As evident from the plot, the matrix is not symmetric. Since the Morton ordering preserves the geometric locality, most of the nonzero entries are located close to the main diagonal. The nonlocal fission corresponding to large spread in the fission matrix indexes is rear and the corresponding fission matrix elements are small. Significant portions of the matrix elements are zero, justifying the assumption about sparse structure.

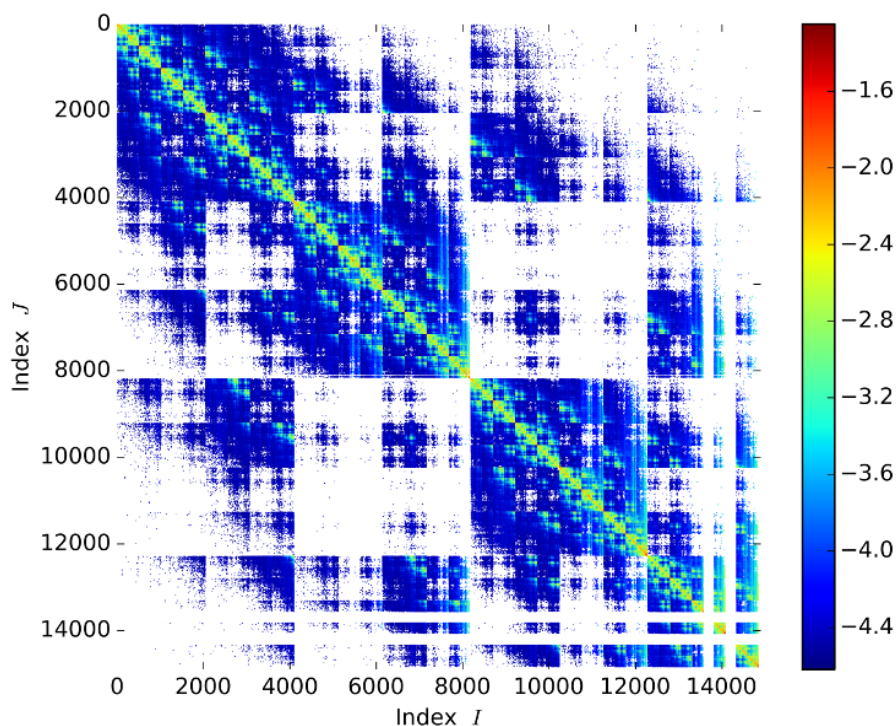


Figure 7.1: Plot of the fission matrix $\log_{10} \mathbf{H}_{i,j}$. The abscissa and the ordinate of the plot represent the matrix indices i and j .

To estimate the eigenvalues power iteration and Arnoldi iteration were used. Unlike the case of discretized deterministic problems the structure of the fission matrix is not known in advance, therefore the choice of the storage scheme is done a posteriori. For the smaller problems dense storage was used and for the larger problems the storage scheme proposed in [57] was used. Once the matrix is accumulated it is transformed into coordinate storage format to be further processed by the eigenvalue algorithms. The coordinate storage uses three vectors **iloc(m)**, **jloc(m)** and **vals(m)** to store the **m** nonzero elements of a matrix. The following example illustrates the storage scheme. The matrix (7.10) is used to demonstrate coordinate format table 7.1. Using this storage format the zero elements are omitted and the memory consumption of the solver routines is significantly improved.

$$\begin{array}{c}
 0 \quad 1 \quad 2 \quad 3 \quad 4 \\
 \begin{array}{c}
 0 \\
 1 \\
 2 \\
 3 \\
 4
 \end{array}
 \begin{pmatrix}
 1 & 7 & 0 & 0 & 0 \\
 7 & 1 & 3 & 0 & 0 \\
 0 & 5 & 1 & 0 & 0 \\
 0 & 0 & 0 & 1 & 0 \\
 0 & 0 & 0 & 0 & 7
 \end{pmatrix}
 \end{array} \tag{7.10}$$

Table 7.1: The coordinate storage format for sparse arrays. Each nonzero matrix element $a_{i,j}$ of the matrix (7.10) is stored by recording its value and its corresponding row i and column j indices.

iloc	0	0	1	1	1	2	2	3	4
jloc	0	1	0	1	2	1	2	3	4
vals	1	7	7	1	3	5	1	1	7

The coordinate storage format works by storing only non zero matrix element $a_{i,j}$ by recording its value and corresponding matrix indices i and j . To illustrate this consider the element $a_{0,0} = 1$ of (7.10). It will be stored by recording its coordinate values $\text{iloc}(0) = 0$, $\text{jloc}(0) = 0$ and the corresponding value of $\text{vals}(0) = 1$. This corresponds to the first column of table 7.1.

Initially the power iteration was used to estimate the eigenvalues of **H**. Suppose $\mathbf{A} \in \mathbb{R}^{n \times n}$ has eigenvalues $|\lambda_0| > |\lambda_1| > |\lambda_2| > \dots > |\lambda_n|$. In addition, the iteration process is started with the initial vector \mathbf{x}_0 continuously multiplied by **A** to form the sequence (7.11)

$$\mathbf{x}^{(k+1)} = \mathbf{A}\mathbf{x}^{(k)}. \tag{7.11}$$

If **A** is diagnosable then the eigenvectors of **A** form a basis. As any vector in \mathbb{R}^n can be expressed as a linear combination of the eigenvectors of **A**. For \mathbf{x}_0 the following expansion holds (7.12)

$$\mathbf{x}_0 = a_0\mathbf{v}_0 + a_1\mathbf{v}_1 + a_2\mathbf{v}_2 + \dots \tag{7.12}$$

Substituting this expression in (7.11) gives (7.13)

$$\begin{aligned}\mathbf{x}^{(k)} &= \mathbf{A}^k \mathbf{x}^{(0)} \\ &= \lambda_0^k \left[a_0 \mathbf{v}_0 + \sum_{i=1}^n a_i \left(\frac{\lambda_i}{\lambda_1} \right)^k \mathbf{v}_i \right].\end{aligned}\quad (7.13)$$

Due to the condition $|\lambda_0| > |\lambda_i|, \forall i \in 1 \dots n$, taking the limit $k \rightarrow \infty$ (7.13) converges to the dominant eigenvector \mathbf{v}_0 . Knowing the eigenvectors the corresponding eigenvalues can be computed using the Rayleigh quotient (7.14)

$$\lambda_k = \frac{\langle \mathbf{v}_k | \mathbf{A} | \mathbf{v}_k \rangle}{\langle \mathbf{v}_k | \mathbf{v}_k \rangle} \quad (7.14)$$

Since not only λ_0 is of interest but also the subsequent eigenvalues, deflation of the spectrum of \mathbf{A} is used. Suppose that at each iteration n

$$\mathbf{x}^{(n+1)} = \mathbf{A} \mathbf{x}^{(n)}, \quad (7.15)$$

subtracting

$$\mathbf{x}^{(n+1)} = \mathbf{x}^{(n+1)} - a_1 \mathbf{v}_1. \quad (7.16)$$

Where a_1 is given by

$$a_1 = \frac{\langle \mathbf{v}_1 | \mathbf{x}^{(n+1)} \rangle}{|\mathbf{x}^{(n+1)}|}. \quad (7.17)$$

In this manner the projection of the iterate $\mathbf{x}^{(n+1)}$ along \mathbf{v}_1 is eliminated and the power iteration converges to the the next largest eigenvalue. In principle, if the matrix \mathbf{A} is symmetric, this technique can be iteratively applied to obtain all the eigenvalues. A custom code was written to perform the iteration (7.11) and apply deflation to estimate the second mode eigenvalue. The consistency of the method was verified against **MATLAB** [58]. The estimated eigenvalues were identical up to eleven places after the decimal. Although the power iteration was able to compute the fundamental eigenvalue in all the cases, the deflation algorithm failed to resolve the eigenvalues when computing 3D problems. To overcome this difficulty a more refined method for computing the eigenvalues was used.

The Arnoldi iteration [59],[60],[61] was chosen for computing the eigenvalues of the fission matrix in the cases where the power iteration with deflation had failed. The power iteration computes normalized sequences in the form (7.18)

$$\mathbf{b}, \mathbf{A}\mathbf{b}, \mathbf{A}^2\mathbf{b}, \mathbf{A}^3\mathbf{b}, \dots \quad (7.18)$$

The elements of the sequence (7.18) all reside in the Krylow spaces

$$\begin{aligned}K_1 &\subseteq K_2 \subseteq \dots \subseteq K_n \subseteq \dots \subseteq K_m \subseteq \mathbb{R}^m \\ K_n &= \text{span}(\{\mathbf{b}, \mathbf{A}\mathbf{b}, \mathbf{A}^2\mathbf{b}, \dots, \mathbf{A}^{n-1}\mathbf{b}\}) \\ \mathbf{b} &\in \mathbb{R}^m\end{aligned}\quad (7.19)$$

The idea of the Arnoldi iteration is to keep the information from all the iterations (7.11) and to

construct iteratively the orthogonal bases for the Krylow space

$$K_n = \text{span} (\{\mathbf{b}, \mathbf{A}\mathbf{b}, \mathbf{A}^2\mathbf{b}, \dots, \mathbf{A}^{n-1}\mathbf{b}\}) = \text{span} (\{\mathbf{x}_1, \mathbf{x}_2, \mathbf{x}_3, \dots, \mathbf{x}_n\}) \quad (7.20)$$

Define the upper Hessenberg matrix by (7.21), i.e. a matrix that has zero elements below the first subdiagonal

$$\mathcal{H} = \begin{pmatrix} h_{11} & h_{12} & \dots & h_{1m} \\ h_{21} & h_{22} & \dots & h_{2m} \\ 0 & \ddots & \ddots & \vdots \\ 0 & 0 & h_{m,m-1} & h_{m,m} \end{pmatrix}. \quad (7.21)$$

Consider the similarity transformation of \mathbf{A} to upper Hessenberg form (7.22), where \mathbf{A}, \mathbf{Q} and \mathcal{H} are matrices in $\mathbb{R}^{m,m}$

$$\begin{aligned} \mathbf{A} &= \mathbf{Q}\mathcal{H}\mathbf{Q}^T \\ \mathbf{A}\mathbf{Q} &= \mathbf{Q}\mathcal{H} \end{aligned} \quad (7.22)$$

since the matrix \mathcal{H} is obtained via similarity transformation from \mathbf{A} , its eigenvalues are related to the eigenvalues of \mathbf{A} . Those eigenvalues are referred to as Ritz values. The above equation can be explicitly written in matrix form

$$\begin{bmatrix} \mathbf{A} \end{bmatrix} \begin{bmatrix} \mathbf{q}_1 & \dots & \mathbf{q}_n \end{bmatrix} = \begin{bmatrix} \mathbf{q}_1 & \dots & \mathbf{q}_m \end{bmatrix} \begin{pmatrix} h_{11} & h_{12} & \dots & h_{1m} \\ h_{21} & h_{22} & \dots & h_{2m} \\ h_{31} & h_{32} & \dots & h_{3m} \\ \vdots & \ddots & \ddots & \vdots \\ h_{m,m-1} & h_{m,m} \end{pmatrix}. \quad (7.23)$$

Considering only the first n columns of (7.23) i.e. the $(n+1) \times n$ upper left section of \mathcal{H}

$$\begin{bmatrix} \mathbf{A} \end{bmatrix} \begin{bmatrix} \mathbf{q}_1 & \dots & \mathbf{q}_n \end{bmatrix} = \begin{bmatrix} \mathbf{q}_1 & \dots & \mathbf{q}_{n+1} \end{bmatrix} \begin{pmatrix} h_{11} & h_{12} & \dots & h_{1n} \\ h_{21} & h_{22} & \dots & h_{2n} \\ \vdots & \ddots & \ddots & \vdots \\ h_{n,n-1} & h_{n,n} \\ h_{n+1,n} \end{pmatrix}. \quad (7.24)$$

The n th column of the above equation gives the recurrence expression for the Arnoldi iteration

$$\mathbf{A}\mathbf{q}_n = h_{1n}\mathbf{q}_1 + h_{2n}\mathbf{q}_2 + \dots + h_{nn}\mathbf{q}_n + h_{n+1,n}\mathbf{q}_{n+1}. \quad (7.25)$$

Equation (7.25) can be written in a more compact form

$$\mathbf{q}_{n+1} = \frac{\mathbf{A}\mathbf{q}_n - \sum_{i=1}^n h_{i,n}\mathbf{q}_i}{h_{n+1,n}}. \quad (7.26)$$

Equation (7.27) is the explicit formula for computing the columns of the unitary matrix \mathbf{Q} and represents the Arnoldi iteration. The iteration process starts with an arbitrary normalized

vector \mathbf{q}_1 . According to (7.27)

$$\mathbf{q}_2 = \frac{\mathbf{A}\mathbf{q}_1 - h_{11}\mathbf{q}_1}{h_{2,1}}. \quad (7.27)$$

The coefficient h_{11} should be chosen such that the scalar product fulfills $\langle \mathbf{q}_1 | \mathbf{q}_2 \rangle = 0$, that is

$$\langle \mathbf{q}_1 | \mathbf{A} | \mathbf{q}_1 \rangle - h_{11} \langle \mathbf{q}_1 | \mathbf{q}_1 \rangle = 0. \quad (7.28)$$

Since $\langle \mathbf{q}_1 | \mathbf{q}_1 \rangle = 1$

$$h_{11} = \frac{\langle \mathbf{q}_1 | \mathbf{A} | \mathbf{q}_1 \rangle}{\langle \mathbf{q}_1 | \mathbf{q}_1 \rangle} = \langle \mathbf{q}_1 | \mathbf{A} | \mathbf{q}_1 \rangle. \quad (7.29)$$

The coefficient h_{11} is given by the Rayleigh quotient (7.29). The last remaining coefficient h_{21} is given by

$$h_{21} = \|\mathbf{A}\mathbf{q}_1 - h_{11}\mathbf{q}_1\| \quad (7.30)$$

Therefore, (7.27) represents a modified Gram-Schmidt method, constructing an orthonormal basis of the Krylov space. In pseudocode the Arnoldi iteration has the following structure.

Algorithm 1 Arnoldi iteration

```

1:  $\mathbf{q}_1 = \frac{\mathbf{b}}{\|\mathbf{b}\|}$  ▷ Start with an initial vector  $\mathbf{b}$ 
2: for  $n=1:N$  do
3:    $\mathbf{x} = \mathbf{A}\mathbf{q}_n$ 
4:   for  $j=1:n$  do
5:      $h_{jn} = \langle \mathbf{q}_j | \mathbf{x} \rangle$ 
6:      $\mathbf{x} = \mathbf{x} - h_{jn}\mathbf{q}_j$  ▷ Subtract the projection on  $\mathbf{q}_j$ 
7:   end for
8:    $h_{n+1,n} = \frac{\|\mathbf{x}\|}{\|\mathbf{x}\|}$ 
9:    $\mathbf{q}_{n+1} = \frac{\mathbf{x}}{h_{n+1,n}}$ 
10: end for

```

The most computational expensive part of the method is the matrix-vector product. Since only the product $\mathbf{A}\mathbf{q}_n$ is needed, a suitable subroutine capable of computing it has to be supplied. For the computations presented here, both the stand-alone version of **ARPACK** and the wrapper available in **MATLAB** were used [62]. It should be noted that the Arnoldi algorithm does not compute the eigenvalues of \mathbf{A} . At each step n , or at occasional steps the eigenvalues of the Hesseneberg Matrix are computed. These are the Ritz values. Since the matrix \mathcal{H} is of a modest size, the Ritz values can be efficiently computed. The Ritz eigenvalues converge to the eigenvalues of \mathbf{A} . Since the size of \mathcal{H} is smaller than the size of \mathbf{A} the method can not be used to compute all the eigenvalues of \mathbf{A} . The Arnoldi iteration actually computes the eigenvalues corresponding to the edge of the spectrum of \mathbf{A} . This is quite useful in the case of the fission matrix, since these are precisely the eigenvalues of interest. As evident from (7.27), storing all the $\mathbf{q}_1, \dots, \mathbf{q}_n$ is rather expensive. Furthermore the computational effort increases linearly with increasing the number of iterations. Therefore, the Arnoldi iteration is usually restarted after a number of iterations [62].

7.3 Practical implementation and numerical computation of higher mode eigenstates

To tally the fission matrix a spatial discretization mesh with N over the geometry is superimposed. The cell of birth m and the cell n , where the neutron born in m causes fission are tallied. This is done by directly evaluating the fission bank array. Therefore the fission matrix will have N^2 elements. For instance, if a spatial mesh with $(N_x = 128) \times (N_y = 128) \times (N_z = 20)$ elements is used, the memory needed to store all the values of \mathbf{H} if 8-bit reals are used, will be significantly more than what most modern computers can provide (860GB). The fact that the matrix is only sparsely populated, together with suitable sparse storage scheme can significantly reduce the amount of memory needed. As shown in fig. 7.1 the fission matrix have diagonal structure. Moreover, due to the limited mean free path of thermal neutrons, the elements having small spread in the indexes (m, n) are much larger than those corresponding to nonlocal fission. The first 15 eigenvalues estimated using different fission matrix resolution are shown in table 7.2. In all the cases the fission matrix was capable of precisely estimating the fundamental eigenvalue k_0 , which showed excellent agreement with the Monte Carlo power estimate. The higher order eigenvalues showed larger susceptibility to the mesh resolution. To ensure that no bias is introduced, the mesh study was further improved by refining the mesh to 256×256 elements corresponding to quarter pin resolution. The k_1 in this case showed good agreement with the 128×128 case.

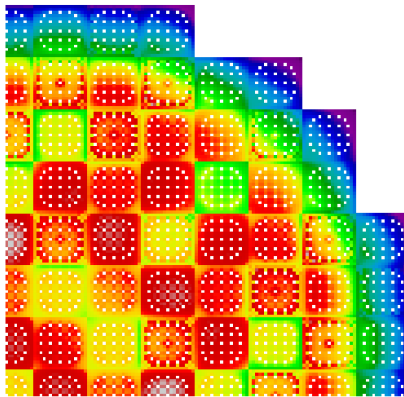
Table 7.2: Higher mode eigenvalues of the fission matrix as a function of the mesh resolution and the number of histories used for the simulation.

Histories	5×10^6	5×10^5	1×10^6
Estimated k_{eff}	1.00635 (2)	1.00635 (2)	1.00635 (2)
Mesh	60×60	128×128	256×256
k_0	1.00633681	1.00633682	1.00633681
k_1	0.98734693	0.98776299	0.98758907
k_2	0.97818760	0.97891091	0.97854092
k_3	0.95377283	0.95495717	0.95446119
k_4	0.92188236	0.92374119	0.91736150
k_5	0.91630770	0.91817160	0.90305064
k_6	0.90179636	0.90407502	0.92289377
k_7	0.87260013	0.87548326	0.87429778
k_8	0.84831091	0.85167208	0.85020312
k_9	0.83525601	0.83846278	0.83094840
k_{10}	0.82888577	0.83181008	0.83727213
k_{11}	0.80167342	0.80503211	0.80423848
k_{12}	0.78321471	0.78753893	0.78579037
k_{13}	0.76450511	0.76914195	0.76725934
k_{14}	0.73978934	0.74406155	0.74224522

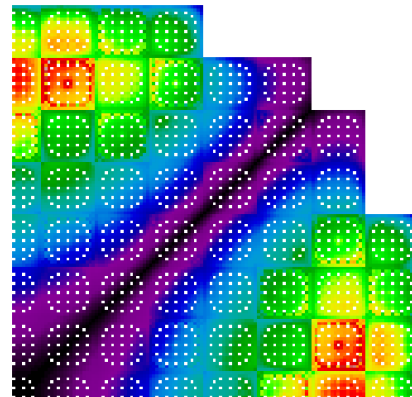
For the sake of completeness, the eigenvectors corresponding to the first sixteen largest eigenvalues are shown in figs. 7.2(a) to 7.2(h) and 7.3(a) to 7.3(g).

Figure 7.2: The eigenvectors corresponding to eigenvalues k_0 to k_7 .

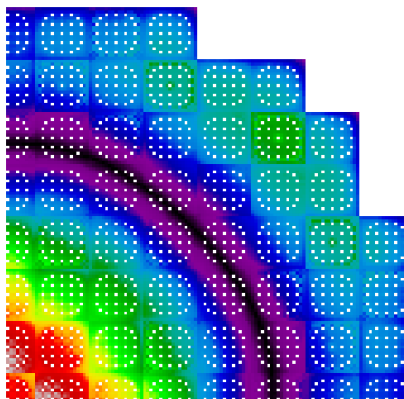
(a) $k_0 = 1.00633682$



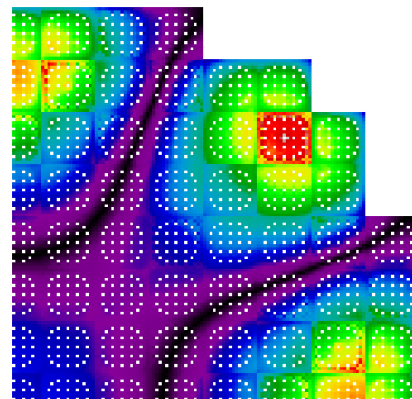
(b) $k_1 = 0.98776299$



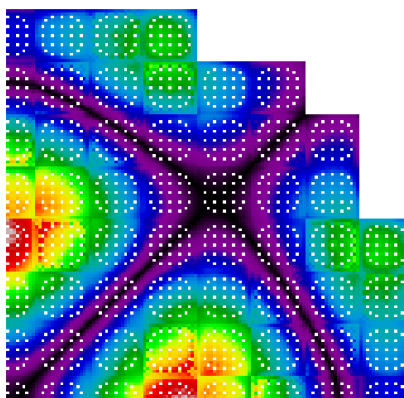
(c) $k_2 = 0.97891091$



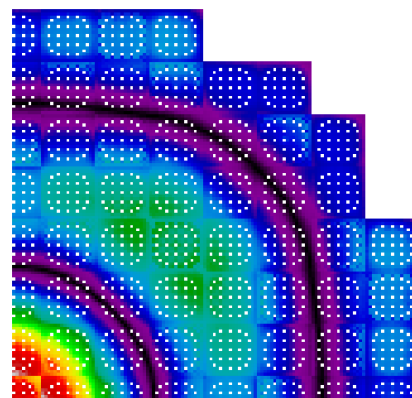
(d) $k_3 = 0.95495717$



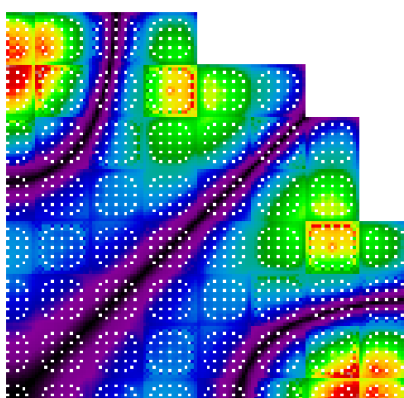
(e) $k_4 = 0.92374119$



(f) $k_5 = 0.91817160$



(g) $k_6 = 0.90407502$



(h) $k_7 = 0.87548326$

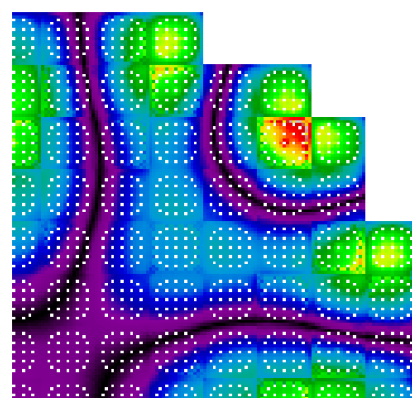
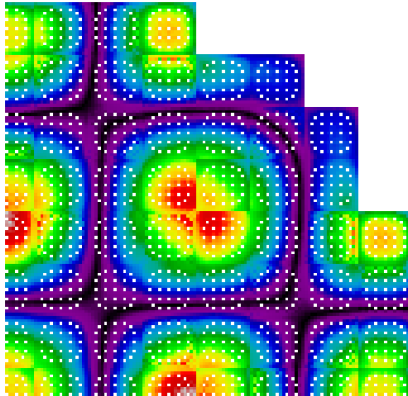
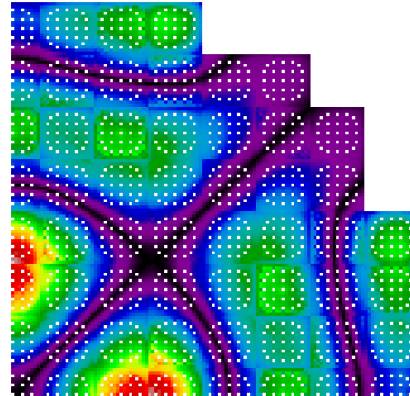
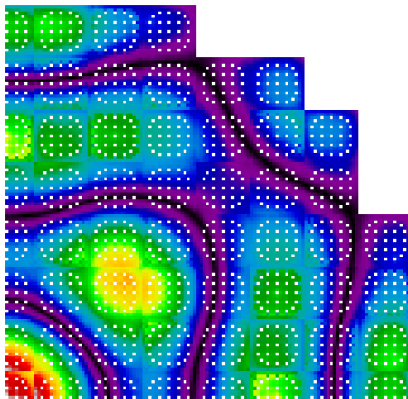
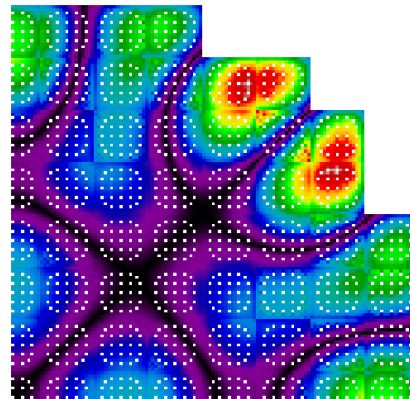
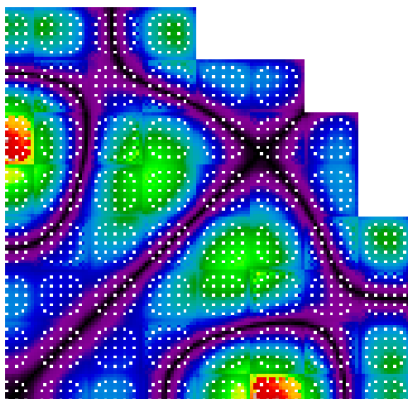
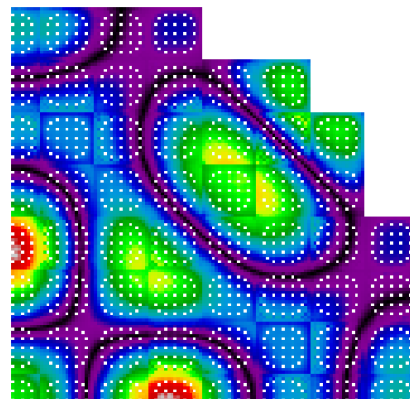
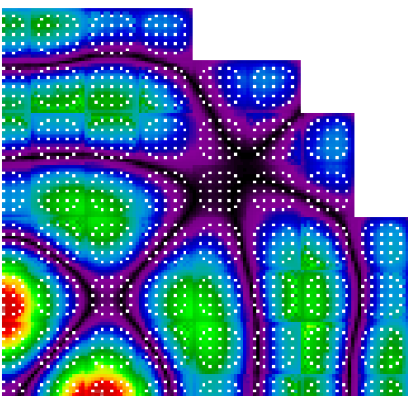
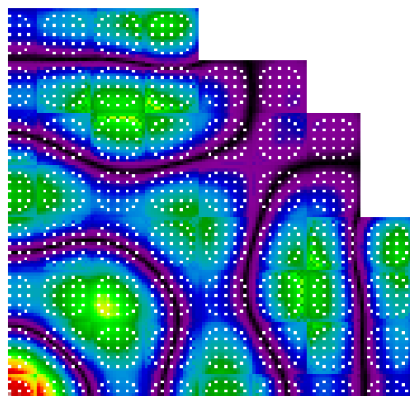


Figure 7.3: The eigenvectors corresponding to eigenvalues k_8 to k_{15} .(a) $k_8 = 0.85167208$ (b) $k_9 = 0.83846278$ (c) $k_{10} = 0.83181008$ (d) $k_{11} = 0.80503211$ (e) $k_{12} = 0.78753893$ (f) $k_{13} = 0.76914195$ (g) $k_{14} = 0.74406155$ (h) $k_{15} = 0.74312169$ 

Only the fundamental mode eigenvector fig. 7.2(a) has direct physical interpretation. The convergence of the power iteration scheme to the fundamental eigenmode solution involves iterating until the higher eigenmodes are small enough to be neglected. The standard power iteration in both the deterministic and the Monte Carlo cases converges to the fundamental mode eigenvalue rather slowly. Precisely to overcome this deficiency the Wielandt acceleration was implemented in **MCNP**. The effect of the Wielandt acceleration on the convergence of the Monte Carlo power iteration will be presented in the next section.

7.4 The Wielandt acceleration and its effect on the Monte Carlo power iteration

According to the description of the Wielandt acceleration, the system becomes more tightly coupled by increasing the length of the neutron histories. In the classical Monte Carlo transport the neutrons are removed from the transport calculation once they cause fission and the histories of the neutrons newly produced are started during the subsequent cycle. Thus fission is treated as capture. Using the Wielandt acceleration following each fission event a number of neutrons are stored in the particle bank and their histories are continued in the same cycle. This can be effectively demonstrated using the fission matrix. In contrast to the sparse structure observed in fig. 7.1, the fission matrix corresponding to the calculation with Wielandt shift is dense fig. 7.4. This shows that the spread of the matrix indices, denoting the start and the end regions of each history have much larger spread. Or in other words, distinct regions have significantly increased chance of exchanging neutrons.

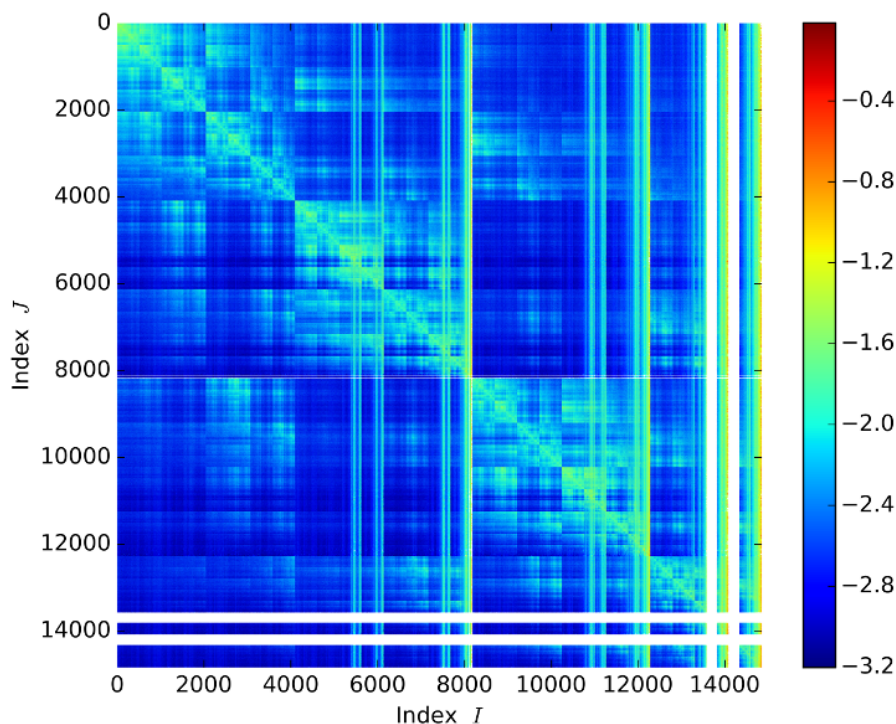


Figure 7.4: Plot of the fission matrix $\log_{10} \mathbf{H}_{i,j}$. The abscissa and the ordinate of the plot represent the matrix indices i and j .

The theory of the Wielandt acceleration shows that the power iterations are accelerated by reducing the dominance ratio. This effect is shown in table 7.4 for two dimensional geometry. The second column of the table shows the Wielandt shifted eigenvalues, the third column is the back transformed values and in the last column, the reference analog eigenvalues are

shown. The calculation shows that the dominance ratio for the shifted spectrum is $\lambda_{\text{Wielandt}} = 0.5182$. The reference analog value is $\lambda_{\text{analog}} = 0.9815$. Due to the reduced dominance ratio, the power iteration in the case of the shifted operator is significantly improved. Using the back transformation formula $\frac{1}{k_{\text{Wiel}}} = \frac{1}{k_{\text{eff}}} - \frac{1}{k_e}$ it is possible to recover all the eigenvalues of the original spectrum as the theory suggests. To increase the fidelity of the calculation, the fission matrix with single pin resolution was used.

Table 7.3: Fission matrix eigenvalues with shift (two dimensional case)

Case	Shifted eigenvalues	Back-transformed	Analog calculation
k_0	43.84717401	1.00635992	1.00633682
k_1	22.72174319	0.98533380	0.98776299
k_2	17.89174532	0.97393223	0.97891091
k_3	12.31823398	0.95052132	0.95495717
k_4	8.37390612	0.91718518	0.92374119
k_5	7.96613385	0.91207156	0.91817160
k_6	7.59842687	0.90704595	0.90407502
k_7	6.13117778	0.88185398	0.87548326
k_8	4.84414158	0.84939489	0.85167208
k_9	4.59598843	0.84142869	0.83846278
k_{10}	4.27345593	0.82996063	0.83181008

The eigenvalues spectrum for three dimensional calculations were also computed and the results are shown in table 7.4. For tallying the fission matrix $X = 64 \times Y = 64 \times Z = 20$ mesh was used. Both cases have a high dominance ratio close to unity. The first two columns show the eigenvalues corresponding to the coupled PWR MOX-UO2 benchmark described in [63],[64]. The second two columns show the eigenvalues corresponding to the case summarized in table 6.4. Having computed the dominance ratio, the large asymmetries of the fission heat deposition shown in table 5.2 can be explained. The dominance ratio for both the cases is above 0.98. Therefore, many iterations are needed before the higher mode eigenvalues are damped. In the analog case due to the decoupling of the system many more iterations are needed. Since the large tilt in power is still present, tallying was done at a stage when the source distribution was still ill converged. This situation was not detected by the source entropy. To resolve this problem the number of criticality cycles should have been significantly increased. According to (5.14) for eigenvalue shift of $k_e = k_{\text{eff}} + 2 \times 10^{-2}$ and $k_{\text{eff}} = 1.15099$ about 60 extra neutrons are produced and to a large extent, tally results obeying the symmetry of the problem are obtained. Since the analog calculation runs with the original high dominance ratio, more than 60 extra histories would be needed to achieve the same quality of results. This can be explained by the fact that in the analog calculation the locality is preserved and the increase of the particle population will not be as effective as

in the case when the Wielandt acceleration is used.

Table 7.4: Fission matrix eigenvalues with shift (three dimensional case)

	Shifted eigenvalues	Back-transformed	Shifted eigenvalues	Back-transformed
	$\frac{k_1}{k_0}=0.56892$	$\frac{k_1}{k_0}=0.98521$	$\frac{k_1}{k_0}=0.49732$	$\frac{k_1}{k_0}=0.98385$
k_0	50.47995806	0.99979804	70.87623553	1.15099970
k_1	28.71921661	0.98501589	35.24794216	1.13241139
k_2	27.96514844	0.98410576	20.57907311	1.10705939
k_3	26.40712812	0.98206675	13.80865722	1.07860997
k_4	18.87507174	0.96770564	9.24478054	1.03856180
k_5	18.70897967	0.96726539	8.90365601	1.03411090
k_6	17.66129405	0.96430793	7.25299170	1.00748055
k_7	17.20757142	0.96292163	7.09321651	1.00433812
k_8	15.44619338	0.95681600	6.09896472	0.98167882
k_9	14.52331122	0.95306446	5.28202365	0.95783401
k_{10}	13.31685938	0.94743181	4.83469176	0.94202826

Reducing the variance of the Monte Carlo criticality calculations

In chapter 4 a method for accelerating the flux and fission heat tallying is presented. This method relies on optimizing the coding of **MCNP**. Having fast tallying solves only partially the problem of local fission heat estimation, since the tallies still have large statistical uncertainties. In this thesis the fission heat deposition is tallied at a pin by pin resolution and supplied to the subchannel code. To reduce the statistical uncertainties, a novel highly efficient variance reduction method, uniform fission site, was implemented in **MCNP** and its effectiveness was compared against the well established variance reduction methods available in **MCNP**. It is shown in particular, that variance of less than 1.4 % can be obtained for local fission heat estimates even when simulating large LWR core geometry. The most important part of the newly implemented uniform fission site method is that it does not slow down the criticality calculation. Reducing the variance is essential for reaching convergence of the coupled system system **MCNP** - SCF. Practical calculations showed that supplying power distributions with large statistical uncertainties results in failed convergence of the subchannel code.

In Monte Carlo simulations the expectation value $\langle x \rangle$ for a certain event x is sampled

$$\langle x \rangle = \int xp(x)dx. \quad (8.1)$$

This is done by sampling individual random particle walks and assigning a score x_i to each random walk. In general, the probability density $p(x)$ is not known and the integral (8.1) can not be computed analytically. Therefore, the law of large numbers is used and this integral is approximated by

$$\int xp(x)dx = \lim_{N \rightarrow \infty} \frac{1}{N} \sum_{i=1}^N x_i, \quad (8.2)$$

thereby estimating the expectation value $\langle x \rangle$ or the true mean by the sample mean \bar{x} . The unbiased estimator for the standard deviation after applying the Bessel correction and

replacing N with $N - 1$ is given by

$$S^2 = \frac{1}{N-1} \sum_{i=1}^N (x_i - \bar{x})^2 \approx \overline{x^2} - \bar{x}^2. \quad (8.3)$$

The estimated variance of \bar{x} , $S_{\bar{x}}$ is given by (8.4)

$$S_{\bar{x}} = \frac{S}{\sqrt{N}}. \quad (8.4)$$

In Monte Carlo codes each Monte Carlo estimate is reported with the corresponding relative error defined by (8.5)

$$R = \frac{S_{\bar{x}}}{\bar{x}} \quad (8.5)$$

The aim of the different variance reduction techniques is to make $S_{\bar{x}}$ as small as possible. The essence of the variance reduction techniques can be readily understood by taking into account the expression for the expectation value. Using variance reduction, $p(x)$ is modified so that the spread from the mean is reduced.

Reducing the variance is especially important in the case of coupled calculations. A power distribution that has large local statistical uncertainties, has in general a non-smooth shape. This significantly complicates the convergence of the thermal hydraulic solution and might result in convergence failure. As shown in practice, simple brute force increase of the particle population is very inefficient. Due to the nonuniform distribution of the fission power, only a minor influence is exerted on the low power regions. Having in mind that the relative error in Monte Carlo calculations is inversely proportional to the square root of the number of histories $r = \frac{\sigma}{\sqrt{N_{\text{hist}}}}$, simple increase of N_{hist} would result in unacceptable run-times. Therefore, one has to run nonanalog transport. A nonanalog Monte Carlo technique will have the same expected tallies as an analog technique if the expected weight executing any given random walk is preserved. Non analog transport can significantly reduce the tally variance by sampling naturally rare events with increased frequency and weighting the tallies appropriately. In the particular case of the power estimate in a heterogeneous loosely coupled system, a variance reduction technique capable of homogenizing the relative error distribution is needed. In the ideal case, if homogenized relative error was achieved, one would be able to reduce the relative error proportionally in all parts of the domain.

8.1 The Global Variance Reduction Technique

To reduce the variance of the power estimate a Global Variance Reduction (GVR) technique has been proposed [49]. The idea relies on the Weight-Windows capability that has been implemented in **MCNP** [25]. The Weight-Window (WW) technique consists of defining a mesh of upper and lower particle weight bounds. These weight bounds are user defined, and can be made to encompass the entire particle phase space. Particles having weights exceeding the upper weight-window bound, are split into N individual particles. The weights of the

newly created particles are reduced so that they fit in the WW boundaries. Particles having weights smaller than the lower WW bound are either killed or have their weight increased to a predefined survival weight W_S based on a stochastic selection mechanism. The concept is illustrated in the following fig. 8.1.

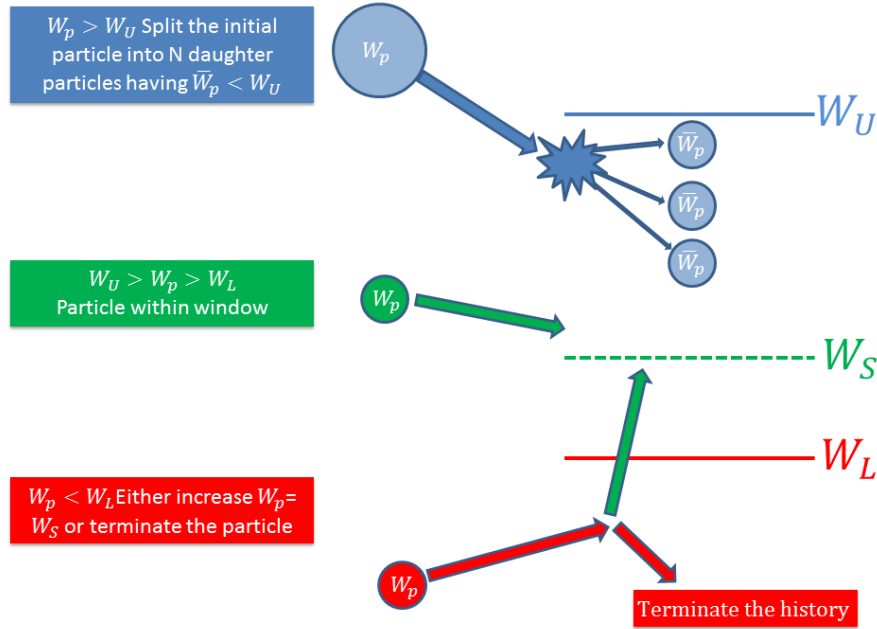


Figure 8.1: Principle of the Weight Windows technique.

In **MCNP** both W_S and W_U are integer multiples C_S and C_U of the lower bound W_L . The basic idea of GVR is to obtain a uniform nonanalog particle density. The analog particle density in a particular volume V is given by (8.7)

$$n_k = \frac{\phi_k}{V} \approx m_k \bar{w}_k. \quad (8.6)$$

$m_k \bar{w}_k$ is the product of the nonanalog particle density times the average weight. By setting (8.7)

$$\bar{w}_k \propto \phi_k, \quad (8.7)$$

the nonanalog particle density will be approximately constant. Therefore, a weight window mesh is set over the geometry. The lower bound of the weight window in this case is (8.8)

$$W_L = \left(\frac{\beta + 1}{2} \right) \frac{\phi_k}{\max_k \phi_k}. \quad (8.8)$$

Therefore in this thesis, a special optimized routine was implemented in **MCNP** with the aim

to tally the fluxes simultaneously with the power density. This was achieved by including an additional dimension to the tally array. This was done because the power distribution is needed as a boundary condition for the thermal hydraulics code. The track length estimator was used for tallying. For the upper bound the standard options $W_U = 5W_L$ and $\beta = 5$ were unaltered. The particle weights are selected such, so that the total source weight of each cycle is a constant N . That is, the weight of each source particle is (8.9)

$$w_0 = \frac{N = \text{Nominal Source Size}}{M = \text{Actual number of neutrons started in the current cycle}}, \quad (8.9)$$

so all normalizations occur as if N rather than M particles are started in each cycle. Usually $w_0 \approx 1$. According to the definition of the weight windows method and using (8.8), the regions having very low flux estimates will have very low W_U and, therefore, the density of the nonanalog particles m_k will be significantly increased. In this manner more nonanalog particles are created in the regions of interest reducing the statistical uncertainty. Due to (8.7) both the eigenvalue and eigenvector estimates remain unbiased.

To implement this scheme, an initial run is needed to estimate the cell fluxes ϕ_k . The most promising results were obtained when the mesh WW mesh was defined to overlap precisely the pin cell mesh. One can run several iterations obtaining ever better tally estimates. The special WW input files were written with an internal subroutine to avoid potential I/O errors and to minimize the code - user interaction. It was observed that using the GVR technique significantly slows down the calculation, often resulting in more than two fold computational time increase. This can be easily understood by making the following observation. Formula (8.8) tells us that for the cells having $\phi_k \approx \max_k \phi_k$ the population will remain unaltered, on the contrary cells satisfying $\phi_k \ll \max_k \phi_k$ large number of additional particles will be produced. Thus to improve the variance, additional particles are created in low populated regions. Following the histories of the extra particles slows down the execution. An additional drawback is the necessity to run the code twice. This drawback is diminished when running coupled iterations with the thermal hydraulic code. In this case, the flux estimate from the previous iteration might be used for generating the WW mesh.

8.2 The Uniform Fission Site method

Having in mind the drawback of GVR, the decision was made to implement a less computationally expensive variance reduction technique - the Uniform Fission Site method (UFS) [10]. The basic idea of this method is to redistribute the fission source so that artificially more fission neutrons are created in low power regions. The calculation is kept unbiased by reducing the initial source weight of the fission neutrons. The additional number of neutrons is obtained by redistributing the fission source from the high-power regions. Since the total number of neutrons remain unaltered, no additional computational time is lost. The idea behind the method is again ensuring uniform nonanalog particle density. This is done by directly redistributing the fission source rather than splitting the particles. In contrast to the GVR technique, implementing the UFS method requires significant modification to the source code.

When a fission event is sampled, N_f neutrons are stored in the fission bank (8.10)

$$N_f = w \frac{\nu \Sigma_f}{\Sigma_t k_{\text{eff}}}. \quad (8.10)$$

Since the aim of the method is increasing the number of fission neutrons in low-power cells, the number of neutrons produced per fission is modified by multiplying it with a coordinate dependent factor $\lambda(\mathbf{r})$

$$N_f^{\text{mod}} = \lambda(\mathbf{r}) \times w \frac{\nu \Sigma_f}{\Sigma_t k_{\text{eff}}}. \quad (8.11)$$

To compute $\lambda(\mathbf{r})$, a source mesh was implemented in **MCNP**. This mesh comprises the entire domain where fissionable material is present. In each mesh element, the fraction of fission source s_k is stored. The coordinate function $\lambda(\mathbf{r})$ is accumulated during the inactive cycles, according to (8.12)

$$\lambda(\mathbf{r})^{-1} = \frac{s_k}{\langle s_k \rangle}. \quad (8.12)$$

Thus, using UFS the inactive cycles are effectively used in the calculation. To keep the transport unbiased, the starting weight (8.9) of all the neutrons produced according to (8.11) is modified to

$$w_{\text{ufs}} = \frac{N}{\Lambda}. \quad (8.13)$$

This is related to the fact that the starting weights of the **MCNP** calculation are not equal to unity but are selected such so that the total source weight is constant. Here Λ is the total starting weight of the neutrons in the current cycle and N is the nominal source size. In the standard **MCNP** calculation Λ is equal to the actual number of particles that have started in

the current cycle i.e. M from equation (8.9). If UFS is used, it is computed by summing the weight of the neutrons located in the current batch of the fission source

$$\Lambda = \sum_{i \in \text{current batch}} \frac{1}{\lambda(\mathbf{r}_i)}. \quad (8.14)$$

In addition, equation (8.14) has to be divided by the local value of $\lambda(\mathbf{r})$. The parameter $\lambda(\mathbf{r})$ has to be stored together with the fission energy and the coordinates \mathbf{r} of the fission site. The additional information was stored in the fission bank array. This information is retrieved during the next cycle, when the histories of the fission neutrons are initiated and simulated. Some w_{ufs} might be lower than the predefined default minimum weight and will therefore be forced to play 'Russian roulette'. That is, the particle is either killed or survives with probability $\frac{w}{w_{\text{surv}}}$, where w is the weight of the particle entering the 'Russian roulette'. w_{surv} is the user defined survival weight. The averaged particle weight after 'Russian roulette' is given by (8.15)

$$\langle w \rangle = w_{\text{surv}} \times \frac{w}{w_{\text{surv}}} + 0 \times \left(1 - \frac{w}{w_{\text{surv}}}\right) = w, \quad (8.15)$$

meaning that the process is unbiased. The weight-cutoff for the 'Russian roulette' must be smaller than the survival weight, that is

$$w_c < w_{\text{surv}}, \quad (8.16)$$

with a typical value $w_c = 0.5 \times w_{\text{surv}}$.

This would have negated the benefit of the UFS method, by the undesired modification of the particle weight. To minimize this undesired effect the default minimal weight, it was reduced to $w_c = 0.01$ and the survival weight w_{surv} correspondingly [10].

In addition to the method outlined above, it is possible to use the fundamental eigenvector of the fission matrix to estimate $\lambda(\mathbf{r})$.

8.3 Numerical performance of the variance reduction techniques

To estimate the efficiency of the variance reduction schemes described in the previous sections, the same quarter core with the same geometry as the one shown in fig. 5.1 was used. For the GVR scheme, a mesh having the resolution of single pin cell was used. In the case of UFS, each assembly was split into 16 subvolumes. A total of 1×10^9 histories were simulated. Each calculation simulated 1000 criticality cycles, with 200 of them inactive. Since neither density nor temperature distributions were modeled, the power profile was axially symmetric. The power distribution was calculated using the optimized power tallying subroutines described in chapter 4.

Two dimensional plots of the pin power relative error is shown in fig. 8.2 and fig. 8.3. As expected, the relative error homogeneity is significantly improved in the UFS case. This effect is most pronounced in the lower-most core slice and at the core periphery.

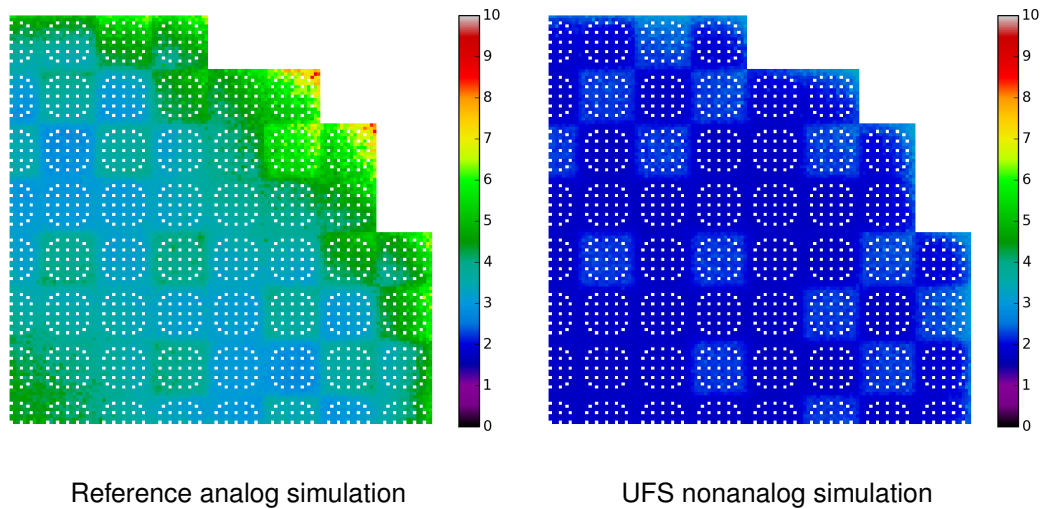


Figure 8.2: Two dimensional plot of the relative error of the fission heat deposition distribution in %. Each point represents the value of the relative error for a single fuel pin.

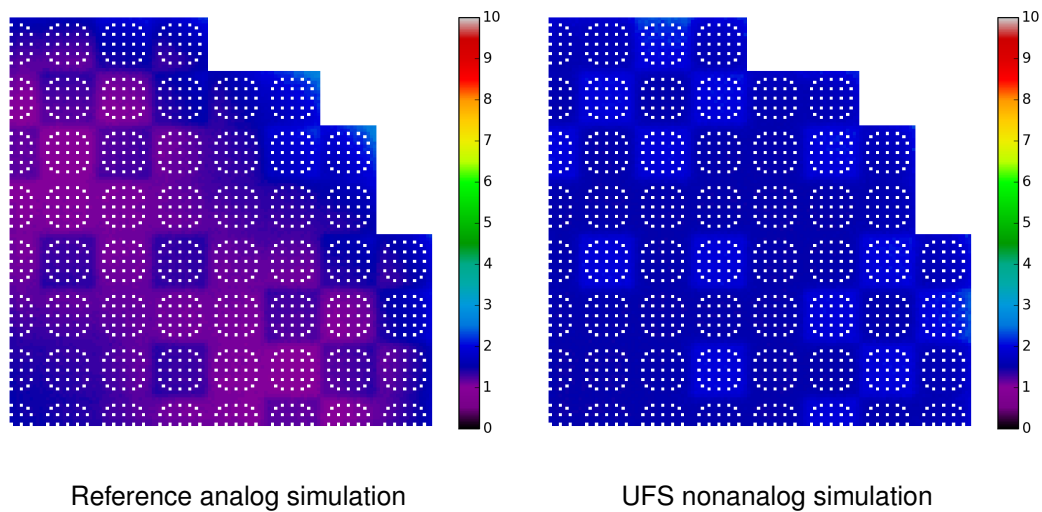


Figure 8.3: Two dimensional plot of the relative error of the fission heat deposition distribution in %. Each point represents the value of the relative error for a single fuel pin.

As expected, the GVR produced relative errors lower than the UFS in fig. 8.4. Due to the large number of additional particles produced by the WW splitting, this is a misleading comparison. The large number of additional particles, caused three times longer execution time in the case of GVR. Judging based on the run-time, the actual number of particles being simulated during GVR is at least 2.5 times larger than in the UFS case. Therefore, comparing the magnitude of the relative errors and the wall clock time separately is not a conclusive comparison. To investigate the quality of the simulation, comparison of the figures of merit is necessary

(5.16).

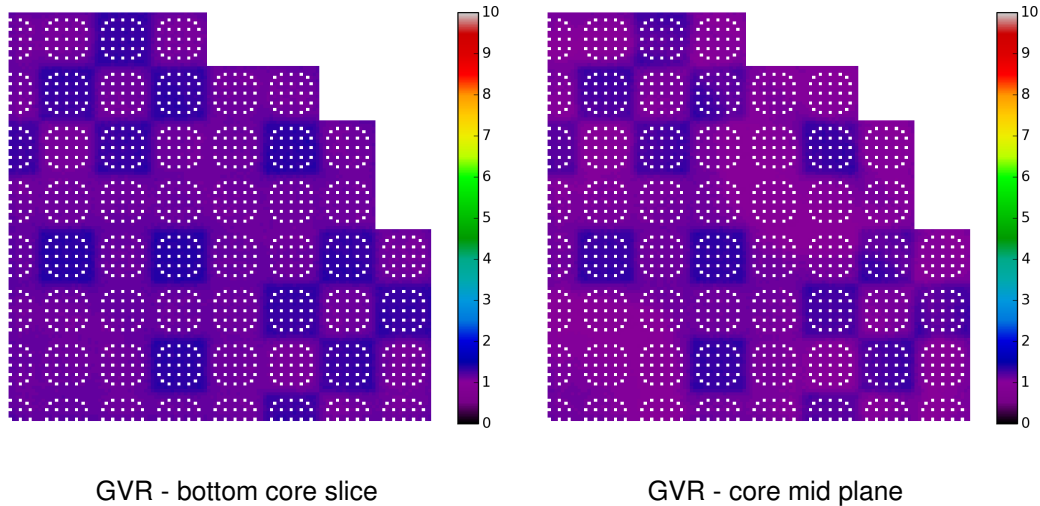


Figure 8.4: Two dimensional plot of the relative error of the fission heat deposition distribution in %. Each point represents the value of the relative error for a single fuel pin.

All the runs are summarized in table 8.1. According to the relative error distribution, the GVR scheme manages to reduce the relative errors and to homogenize their distribution throughout the core. Due to the additional histories followed, the computational time is significantly increased. Since UFS only redistributes the fission source, it adds an insignificant amount to the total run time. The effect of the source redistribution can be clearly seen in fig. 8.3. Since part of the source particles are taken and shifted to improve the statistics in regions with low power, the variance in the case of the UFS is higher in the center of the core when compared to the analog simulation. But in contrast to the analog calculation, in the case of UFS, the error is uniformly distributed, meaning that by increasing the number of histories the relative errors in the entire geometry are reduced uniformly. In contrast, due to the heterogeneous distribution of the relative error in the analog simulation, mostly the high power regions will be effected by increasing the number of histories, leaving the periphery almost unaffected. In the case of the homogeneous error, one can easily estimate of the number of histories needed N_{target} to reach a target statistical uncertainty σ_{target} . Due to the statistical uncertainty being inversely proportional to the square root of the number of particles one has

$$N_{\text{target}} = \sqrt{\frac{\sigma_{\text{old}}}{\sigma_{\text{target}}}} N_{\text{old}}. \quad (8.17)$$

Comparing the figures of merit, UFS outperforms GVR since it maximizes the figure of merit. Moreover, since GVR operates in automatic mode it makes it much easier to use, and

it requires no additional input files.

Table 8.1: Performance summary of the variance reduction techniques. 750 active cycles with 1×10^6 histories per cycle.

Calculation	Eigenvalue k_{eff}	FOM	run time (min)
Analog	1.15100 (2)	29.09	81.70
GVR	1.15096 (3)	33.15	240.32
UFS	1.15100 (3)	36.80	85.03

Being an integral quantity k_{eff} , is not a sensitive enough comparison parameter. Therefore, to ensure the consistency of the method, the fission heat deposition tallies were compared for the entire geometry. One additional run, with 1.3×10^6 histories per cycle, was done in the case of UFS. Results from the comparison are shown in table 8.2, where the additional run is given is summarized in the last row of the table and is colored red.

Table 8.2: Performance summary of the variance reduction techniques. 750 active cycles with 1×10^6 histories per cycle were run together with an additional run using 1.3×10^6 particles per cycle.

Calculation	Eigenvalue k_{eff}	FOM	Max. Difference from GVR %	run time (min)
GVR	1.15096 (3)	33.15		240.32
UFS	1.15100 (3)	36.80	8.5	85.03
UFS	1.15102 (3)	41.6	3.4	109.6

As shown in table 8.2 increasing the number of histories ensures the convergence of UFS to the power values computed via the GVR. Nevertheless, the UFS method runs more than twice faster than the GVR.

Since the UFS, the GVR and Wielandt shift reduce the relative error it is interesting to see whether they produce the same results. For the twenty axial nodes, the absolute value of the maximum difference in the estimated fission heat deposition was computed. The same notation as in table 5.3 is used. For the comparison, the UFS is run with 1.3×10^6 histories. The results are shown in table 8.3. As shown in table 8.3 both methods produce results that are very close. The statistical uncertainty of $|\Delta_k|$ was estimated using partial derivatives. The notation uses the formulas given in (5.21) and (5.20). The maximum difference for all the axial nodes is larger than the associated statistical uncertainty. As predicted by theory and as presented later in this thesis, the Wielandt shift modifies the dominance ratio of the system. This is the reason why it is difficult to achieve the same degree of fidelity using the standard power iteration. Unfortunately the large increase in run time makes it impractical to run Wielandt calculations using small k_e . Besides the large maximum differences, the values in the table clearly show that both methods deliver results that are on average close to each other. This is shown by the small mean $\mu(\Delta_{i,j}^k)$ and the small standard deviation $\sigma(\Delta_{i,j}^k)$. The small standard deviation makes the average departure from the mean small. Therefore, the large maximum differences are rare events. This comparison motivates the decision to use the Wielandt shift only to converge the fission source and disable it during the active

cycles. Running the Wielandt shift method over the active cycles will be computationally expensive and will in essence try to improve statistically rare events that contribute little to the final result. This strategy was used when running coupled calculations. Doing otherwise would have resulted in massive run times, and would have made the coupled calculation rather impractical. The other strategy of reducing the run time is by using larger shifts quickly deteriorates the performance of the Wielandt method as $k_e - k_{\text{eff}}$ becomes large. The fact that tree methods having different numerical background converge to the same result further proves their correctness.

Table 8.3: Difference between the Wielandt shift method ($k_e = 1.16$) the GVR and the UFS schemes.

Axial node k	UFS				GVR			
	$\ \Delta_k\ $	$\mu(\Delta_{i,j}^k)$	$\sigma(\Delta_{i,j}^k)$	Uncertainty $\ \Delta_k\ $	$\ \Delta_k\ $	$\mu(\Delta_{i,j}^k)$	$\sigma(\Delta_{i,j}^k)$	Uncertainty $\ \Delta_k\ $
1	7.95	1.55	1.16	2.30	7.10	1.11	0.84	1.54
2	8.87	1.31	1.00	1.79	5.26	0.99	0.75	1.33
3	6.49	1.24	0.95	1.78	4.69	0.95	0.71	1.58
4	7.60	1.24	0.95	1.78	4.98	0.94	0.70	1.14
5	6.97	1.22	0.94	2.14	4.97	0.89	0.68	1.29
6	7.34	1.18	0.90	1.54	5.01	0.86	0.67	1.37
7	6.63	1.15	0.89	1.70	5.38	0.88	0.67	1.65
8	6.25	1.15	0.89	1.67	5.16	0.88	0.67	1.25
9	6.69	1.23	0.94	1.59	5.79	0.90	0.69	1.51
10	6.13	1.27	0.96	1.78	4.60	0.87	0.67	1.37
11	6.80	1.20	0.92	1.81	6.03	0.88	0.66	1.32
12	6.11	1.11	0.85	1.66	4.59	0.88	0.68	1.24
13	7.40	1.09	0.84	1.94	5.59	0.93	0.71	1.74
14	6.05	1.09	0.84	1.69	4.64	0.92	0.71	1.38
15	6.32	1.14	0.89	1.47	5.05	0.90	0.69	1.31
16	8.50	1.22	0.94	1.83	4.41	0.89	0.67	0.96
17	7.03	1.33	1.01	1.76	5.55	0.88	0.67	1.18
18	7.91	1.36	1.02	1.74	5.02	0.87	0.67	1.25
19	8.03	1.36	1.04	2.16	5.08	0.87	0.67	1.39
20	8.37	1.58	1.23	2.73	5.19	1.01	0.77	1.25

Coupled Monte Carlo - thermal hydraulics calculations

Coupled Monte Carlo/thermal hydraulics code systems have been developed and applied as reference calculation tools [2],[65],[14]. However, a close inspection of the work done reveals that all those coupled systems have been applied to either small problems or in the case of [13], a coarse mesh thermal hydraulics model. This can be easily explained with the fact that in all these systems, the codes exchange information via the input files. Increasing the resolution of the thermal hydraulic model leads to massive inputs that can take hours for **MCNP** to process. This is a very large penalty in terms of the run-time, and clearly an unacceptable option. To overcome the limitations and to pave the way for high fidelity full core simulations at pin level resolution, innovations were developed in this thesis. Namely the thermal hydraulic feedback is interchanged via the memory, and the macroscopic cross sections are computed by taking into account coordinate dependent temperature and density fields. This approach simplifies the entire strategy of thermal hydraulic feedback immensely, and since the materials are dynamically assigned, the user must provide only proper geometry dimensions.

In addition to the effective scheme for providing the thermal hydraulic feedback, a methodology to accelerate the convergence of the coupled system was developed. The new convergence acceleration scheme is based on the stochastic approximation method due to Robbins and Monro. Using this methodology it was possible to reach uniform convergence within a limited number of iterations. The theoretical description of the acceleration technique is presented hereafter.

9.1 Fundamentals of the stochastic approximation method

The steady state neutron transport equation with no external sources can be transformed into integral form (9.1), the complete derivation can be found in [53].

$$\phi(\zeta) = \int_{\Gamma} K(\zeta, \zeta') \phi(\zeta') d\zeta' \quad (9.1)$$

Here Γ denotes the integration domain of the phase space and ζ represents the phase space variables. This is a Fredholm integral equation. The precise form of the kernel is described in Chapter 3. Being a fixed point problem the existence of the solution is determined by the Banach fixed point theorem [66],[67]:

Theorem 1: Let \mathcal{M} be a complete metric space with distance between two points A and B given by $\rho(A, B)$. Moreover, let $\mathcal{L} : \mathcal{M} \rightarrow \mathcal{M}$ be a contraction operator, for which there exists $k \in (0, 1)$ such that for all $A, B \in \mathcal{M}$, $\rho(\mathcal{L}(A), \mathcal{L}(B)) \leq k\rho(A, B)$. Then, there exists a unique $A \in \mathcal{M}$ such that $\mathcal{L}(A) = A$. The point A , can be generated by the iteration $L(A_{n-1}) = A_n$, with A_0 being arbitrary.

Here the distance is defined to have the following properties: For all $A, B, C \in \mathcal{M}$, $\rho(A, A) = 0$, $\rho(A, B) \geq 0$, $\rho(A, B) = \rho(B, A)$ and $\rho(A, B) \leq \rho(A, C) + \rho(B, C)$. These important properties of the space \mathcal{M} allow us to define convergence. In fact, the proof of the theorem is based on showing that $\rho(A_n, A_m)$ for $A_n, A_m \in \mathcal{M}$ is a Cauchy sequence converging due to the metric space \mathcal{M} being complete by definition. Therefore, the following limit exists (9.2)

$$\begin{aligned} \lim_{n \rightarrow \infty} A_n &= \lim_{n \rightarrow \infty} L(A_{n-1}) \\ A_* &= L(A_*) \end{aligned} \quad (9.2)$$

The Banach fixed point theorem gives an important insight into the solutions of (9.1) and the space they reside on. It should be noted that to fulfill the conditions of a contraction operator, the kernel of the integral transport equation should be bounded and continuous [66]. As pointed out in [67], the estimation of the power profile distribution results in the solution of the following generalization of (9.1)

$$\phi = G(T(\phi), H(\phi)), \quad (9.3)$$

where $H(\phi)$ and $T(\phi)$ are the density and temperature distributions and the value of the functional $G(T(\phi), H(\phi))$ is estimated by the Monte Carlo codes with superimposed statistic noise ξ . This noise has zero mean and the oscillations are symmetric around the mean. The Monte Carlo estimate of the left hand side of (9.3) is defined as (9.4)

$$Y(\phi) = G(T(\phi), H(\phi)) + \xi \quad (9.4)$$

The problem given by (9.4) can be in principle solved by an iterative scheme, consecutively updating $H(\phi)$ and $T(\phi)$. However, this is a very inefficient method. Moreover, the convergence will be limited by the magnitude of ξ . Therefore, in order to achieve convergence one must run a large number of iterations and applying a huge number of particle histories. Based on this, it is recommended to use an acceleration scheme. In the past a relaxation scheme acting on the thermal hydraulic parameters only was used [2]. The old relaxation scheme is described by the equation set (9.5), where i is the iteration step number.

$$\begin{aligned}
T_{\text{fuel},i+1}^{\text{weighted}} &= (1 - \omega)T_{\text{fuel},i-1} + \omega T_{\text{fuel},i}^{\text{actual}} \\
T_{\text{H}_2\text{O},i+1}^{\text{weighted}} &= (1 - \omega)T_{\text{H}_2\text{O},i-1}^{\text{actual}} + \omega T_{\text{H}_2\text{O},i}^{\text{actual}} \\
\rho_{\text{H}_2\text{O},i+1}^{\text{weighted}} &= (1 - \omega)\rho_{\text{H}_2\text{O},i-1}^{\text{actual}} + \omega\rho_{\text{H}_2\text{O},i}^{\text{actual}}
\end{aligned} \tag{9.5}$$

This scheme accelerates the solution. Unfortunately, the convergence rate is still correlated to the statistical noise. If the Fission heat deposition $P(\text{pin}, z)$ within a certain volume V around $z \in \mathbb{R}$ corresponding to a particular pin is tallied by a Monte Carlo code, the associated variance is propagated to the hydraulic distributions. To illustrate this effect, consider the variation of the fuel temperature over two consecutive coupled iterations (9.6)

$$\max_{\text{pin}, z} \left| \frac{T_{\text{fuel},P(\text{pin},z)}^{i+1} - T_{\text{fuel},P(\text{pin},z)}^i + \delta_{T_{\text{fuel},P(\text{pin},z)}^{i+1}} - \delta_{T_{\text{fuel},P(\text{pin},z)}^i}}{T_{\text{fuel},P(\text{pin},z)}^{i+1} + \delta_{T_{\text{fuel},P(\text{pin},z)}^{i+1}}} \right|. \tag{9.6}$$

Clearly if the variation of the hydraulic parameters is used as convergence estimator, it is affected by the induced variance $\delta_{T_{\text{fuel},P(\text{pin},z)}}$. Therefore, to reach the desired convergence one has to reduce the variance of the fission heat deposition. The natural method of accelerating the convergence of (9.3) is to use the stochastic approximation technique. Although the same method of acceleration as in [67] is used, different reasoning concerning its applicability is applied. Namely, in [67] the function we wish to find root of is not directly considered but the gradient of another function, called the objective function, is. Here another approach is used by utilizing alternative formulation of the Robbins and Monro theorem [68], stated hereafter. The formulation of the theorem as well as the proof can be found in [69],[70]. The basic idea is that by observing random variables $Y(X_n)$ of an unknown distribution, roots of the unknown underlying distribution can be found. In the particular case this is the estimate of (9.4).

Consider the following formulation of the Robbins-Monro theorem [70]: Let the sequence (9.7) being an iterative estimate of the equation $\mathcal{K}(\theta) = \alpha$

$$X_{n+1} = X_n - \gamma_n(\alpha - Y(X_n)). \tag{9.7}$$

Where the following conditions on γ_n are imposed (9.8)

$$\sum_{n=1}^{\infty} \gamma_n = \infty, \sum_{n=1}^{\infty} \gamma_n^2 < \infty. \tag{9.8}$$

Theorem 2: If $\mathcal{K}(X)$ and $Y(X)$ fulfill the following conditions

$$\forall X \in \mathfrak{R} : |\mathcal{K}(X)| \leq A|X| + B, (A, B \in \mathfrak{R}), \tag{9.9}$$

$$E[(Y(X) - \mathcal{K}(X))^2] < \infty, \tag{9.10}$$

$$\forall \varepsilon \in (0, 1), \forall X : 1/\varepsilon > |X - \theta| > \varepsilon \Rightarrow \inf_X |\mathcal{K}(X) - \theta| > 0. \tag{9.11}$$

Then $\lim_{n \rightarrow \infty} E(X_n - \theta) = 0$, so that the random variable sequence X_n converges to θ in mean

square and hence in probability.

Since a fixed point of (9.3) is searched (9.7) transforms to

$$X_{n+1} = X_n - \frac{1}{n}(X_n - Y(X_n)), \quad (9.12)$$

with $\gamma_n = \frac{1}{n}$. The theorem has to be proven to be applicable to the particular case (9.3). Since a fixed point problem is being discussed, $\mathcal{K}(\theta) = \alpha$ translates to $\mathcal{K}(\theta) = \theta$. As already shown, Theorem 1 allows the definition metric on the solution space of (9.3) and $\lim_{n \rightarrow \infty} E(X_n - \theta)^2 = 0$ can be defined. Theorem 2, however, requires proving the additional conditions (9.9),(9.10),(9.11). Condition (9.9) holds since $G(T(\phi), H(\phi))$ has to be a contraction operator. According to Theorem 1, choosing any ϕ, ϕ' , one obtains (9.13)

$$|G(T(\phi), H(\phi)) - G(T(\phi'), H(\phi'))| \leq A|\phi - \phi'| \quad (9.13)$$

Since ϕ and ϕ' are arbitrary let $\phi' = 0$. If $\phi' = 0$ the integral on the LHS of (9.3) vanishes i.e. $G(T(\phi'), H(\phi')) = 0$. Then (9.10) follows, the real constant $B = 0$

$$|G(T(\phi), H(\phi))| \leq A|\phi| \quad (9.14)$$

The condition (9.11) holds since the counterparts of $\mathcal{K}(X)$ and $Y(X)$, $G(T(\phi), H(\phi))$ and $Y(\phi)$ are both bounded and they differ only by the stochastic noise ξ . The disc $1/\epsilon > |X - \theta| > \epsilon$ translates to compacts in the space of ϕ . Moreover $G(T(\phi), H(\phi))$ is continuous and $G(T(\phi), H(\phi)) \neq \phi$ for all $\phi \neq \phi_*$, where ϕ_* is the fixed point of interest. Therefore the minimum of $|G(T(\phi), H(\phi)) - \phi|$ is attained on a compact and $\inf_X |G(T(\phi), H(\phi)) - \phi| > 0$ follows.

As pointed out in [67] equation (9.7) can be further simplified. The notation in (9.7) is adapted for the case of the flux

$$\phi^{(n+1)} = \left(1 - \frac{1}{n}\right) \phi^{(n)} + \frac{1}{n} Y(\phi_n) \quad (9.15)$$

Equation (9.15) simplifies to (9.16)

$$\phi^{(n+1)} = \frac{1}{n} \sum_{i=1}^n Y(\phi_i) \quad (9.16)$$

This can be easily shown by induction, first assume (9.15) holds for n and then check if it holds for $n + 1$. Substituting (9.16) in (9.15) the following equation is obtained (9.17)

$$\phi^{(n+1)} = \left(1 - \frac{1}{n}\right) \frac{1}{n-1} \sum_{i=1}^{n-1} Y(\phi_i) + \frac{1}{n} Y(\phi_n) = \frac{1}{n} \sum_{i=1}^n Y(\phi_i) \quad (9.17)$$

Formula (9.16) gives us the explicit formulation of the relaxation scheme. The flux (power profile) in the next iteration is obtained to be the mean value of all iterations. Since in essence the tally estimates from all the runs are added together, simple error propagation with partial derivatives on (9.16) shows the error decreases when more coupled iterations are run. Moreover, from (9.16) follows that the power distributions from all the iterations are reflected in the final solution with weight of $1/n$. Thereby, improving the variance with each coupled iteration. Therefore, any desired convergence parameter (9.6) can be achieved if enough iterations are run. This is still possible even at low number of histories. Never the less, the number of histories and the number of inactive cycles should be chosen adequate to ensure the fission source is converged. Moreover, the effect of increasing the number of histories in the old scheme is achieved by running a large number of iterations in the new scheme.

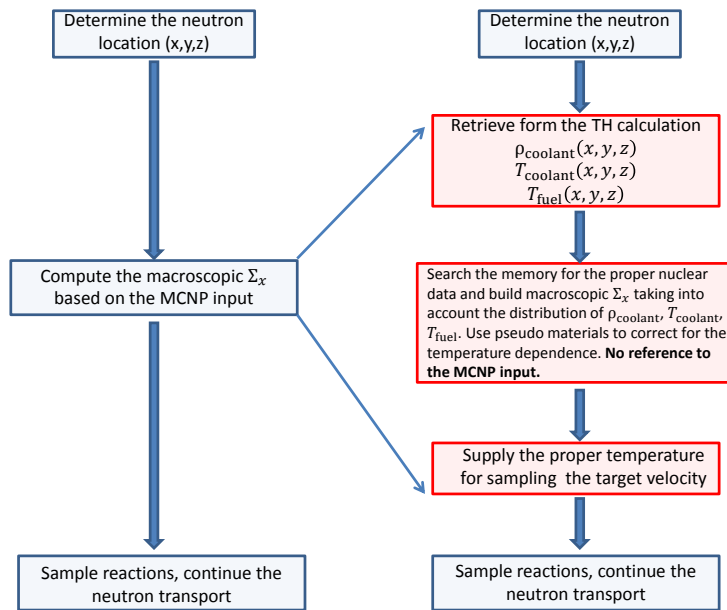
9.2 The internal coupling between Monte Carlo transport and thermal hydraulics

Due to the small mean free path of the neutrons in a typical LWR core, providing precise geometric description of the core components is essential. Therefore refining both the thermal hydraulic and the neutron meshes is essential.

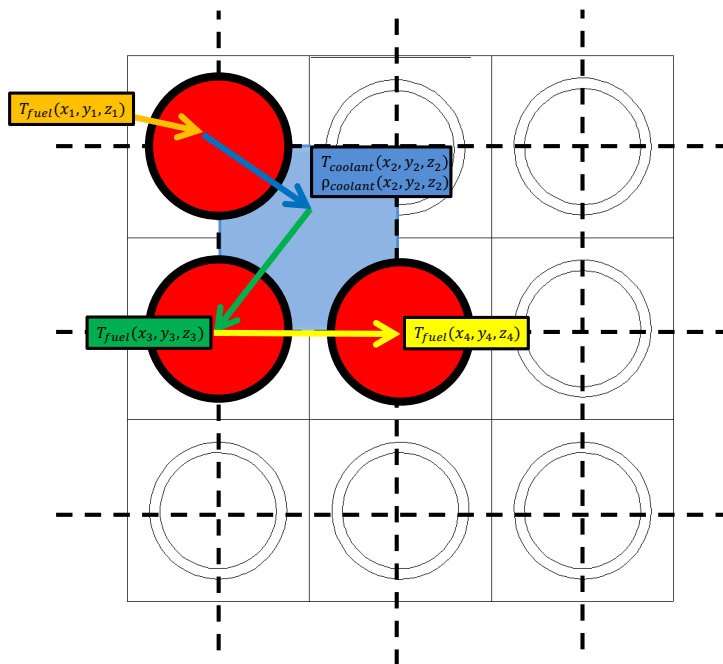
The MCNP code does not support the definition of thermal hydraulic distributions. This fact is a source of major inconvenience when the thermal hydraulic feedback is modeled. The subchannel (SC), thermal hydraulic codes provide detailed distributions of density and temperature. Using the standard methods, these distributions can be introduced in MCNP by subdividing the geometry in a large number of subunits. In each of those subunits, one has to provide distinct material and temperature, this is done by supplying the proper Doppler broadened neutron cross section data and the proper energy corresponding to the most probable velocity of the Maxwell distribution. Following this approach, one can easily generate massive inputs, which can take a significant time for MCNP to process.

Therefore the method of internal code coupling and on-the-fly material definition is suggested as an efficient alternative. It should be taken into account that one also needs a fast running TH code, capable of modeling steady state solutions. Moreover, the thermal hydraulic code of choice should be able to model the coolant flow, the lateral mixing effects and provide results at pin by pin resolution. Subchannel codes seem to be the ideal compromise between precision and run time and are therefore used in the current study. Changing the thermal hydraulic feedback affects the microscopic nuclear cross sections via the Doppler effect and the macroscopic cross sections via the density. As a result, the behaviour of the neutrons in the core changes, and this is subsequently reflected in the flux distribution. Therefore, providing realistic thermal hydraulic conditions to MC calculations is a more accurate description of the physical reality. The material distribution present in the MCNP input, instructs the code how to build the macroscopic cross sections present in the different parts of the geometry. This opens up a possibility for a very elegant treatment of the thermal hydraulic feedback. Instead of relying on the initial input, one can build the macroscopic cross sections according to the distributions obtained from the thermal hydraulic calculation [1],[71],[72]. In this manner the feedback effects are introduced on the fly as the neutron explores the geometry. The methodology is illustrated in fig. 9.1(a).

The necessary nuclear data, both single and double differential, is preloaded into the memory. This includes all the nuclides of interest evaluated at different temperature covering the temperature range defined by the thermal hydraulic run. Subsequently a routine retrieves the data and builds the proper macroscopic cross sections using the correct temperature evaluations to perform pseudo material mixing [73], [74]. For the single differential data the JEFF 3.1.1 nuclear data library was used [75]. The thermal scattering data [43] was used for describing the scattering from bound scatters. Depending how fine the temperature interpolation grid is, the amount of memory needed might vary. However, in all our cases, the required memory never exceeded 1GB. Note how in fig. 9.1(b) the neutron is receiving the



(a) Calculation flow of the coupled system. In red the modified part of MCNP is shown.



(b) On-the-fly feedback interchange.

Figure 9.1: The internal coupling scheme

material distribution at each collision during the trajectory, making the material identification dynamic. The effect of the dynamic material distribution can be demonstrated by making an example with the total cross section. If just the standard code features are used, the total macroscopic cross section $\Sigma_t(\mathbf{r}, E, T_{\text{input}})$ at position \mathbf{r} located in a material consisting of N isotopes is computed as follows (9.18)

$$\Sigma_t(\mathbf{r}, E, T_{\text{input}}) = \rho_{\text{input}}(\mathbf{r}) \cdot \sum_{k=1}^N f_k \cdot \sum_x^R \sigma_{x,k}(\mathbf{r}, E, T_{\text{input}}). \quad (9.18)$$

The microscopic cross section has the temperature defined via the input. The density is also given by the value specified in the input. Using the dynamic material definition the following expression (9.19) is computed when the neutron enters a new cell

$$\Sigma_t(\mathbf{r}, E, T_{\text{TH}}) = \rho_{\text{TH}}(\mathbf{r}) \cdot \left\{ \begin{aligned} & \left(\frac{T_{\text{TH}} - T_{\text{low}}}{T_{\text{high}} - T_{\text{low}}} \right) \cdot \sum_{k=1}^N f_k \cdot \sum_x^R \sigma_{x,k}(\mathbf{r}, E, T_{\text{low}}) + \\ & + \left(1 - \frac{T_{\text{TH}} - T_{\text{low}}}{T_{\text{high}} - T_{\text{low}}} \right) \cdot \sum_{k=N+1}^{2N} f_k \cdot \sum_x^R \sigma_{x,k}(\mathbf{r}, E, T_{\text{high}}) \end{aligned} \right\}. \quad (9.19)$$

Note that in this case the temperature and the density are taken from the thermal hydraulics code as computed in the current coupled run. This is indicated by the subscript TH. Microscopic cross sections having temperatures bracketing the temperature computed by the thermal hydraulic code, have replaced the microscopic cross section defined in the input. The pseudo material mixing also alters in the procedure for selecting the interaction nucleus. The probability to interact with a certain nuclide is given by the atomic fraction f_k . As evident from equation (9.19), each isotope in the case of pseudo material is listed twice, therefore the neutrons interact with one isotope evaluated at two distinct temperatures with probabilities depending on the temperature mixing factors. The combined effect of this interaction corrects for the temperature dependence. Note that this is a purely stochastic effect, relying on the Monte Carlo methodology of sampling the interaction nuclei. The pseudo material mixing also effects in addition the various estimators, for instance, the track length estimator for the multiplication factor now reads (9.20)

$$k_{\text{eff}} = \sum_{i=1}^{\text{Trajectories}} \frac{w_i \rho_{\text{TH}}(\mathbf{r}_i) d_i}{N} \left\{ \begin{aligned} & \left(\frac{T_{\text{TH}} - T_{\text{low}}}{T_{\text{high}} - T_{\text{low}}} \right) \cdot \sum_{k=1}^N \bar{\nu}_k f_k \cdot \sigma_{f,k}(\mathbf{r}_i, E, T_{\text{low}}) + \\ & + \left(1 - \frac{T_{\text{TH}} - T_{\text{low}}}{T_{\text{high}} - T_{\text{low}}} \right) \cdot \sum_{k=N+1}^{2N} \bar{\nu}_k f_k \cdot \sigma_{f,k}(\mathbf{r}_i, E, T_{\text{high}}) \end{aligned} \right\}. \quad (9.20)$$

The flow of the coupled calculation is shown in fig. 9.1. Another major issue is the cell tracking in MCNP. A number of numerical tests showed that the most efficient method is to work directly with the neutron coordinates. To interchange the thermal hydraulic, feedback

a special mesh is superimposed over the computational geometry. This new feature was introduced as an additional procedure in the source code of MCNP. Since the neutron coordinates are known at every instance, the local thermal hydraulic data can be readily retrieved from the superimposed thermal hydraulics mesh. The utilization of the additional feature has a negligible effect on the total run time.

Different codes have been already coupled with MCNP via the input files. This method, although simple is very inefficient, due to the resulting massive inputs. For instance, a MCNP input describing 9 PWR assemblies with subchannel level thermal hydraulics and 20 axial nodes requires more than one million lines of input. This input takes 1.5 hours for MCNP to process. On the contrary, loading the input and the necessary nuclear data for the quarter PWR core using the internal coupling strategy described in this paper takes about 7 minutes, where most of the time is lost reading the cross sections. Therefore, coupling via the inputs is not practical for realistic (large) geometries. It should be clearly understood that the on-the fly material definition is completely equivalent to the MCNP input and should produce identical results. This was tested on various geometries and in all the cases the methodology was confirmed.

In [12] similar to the presented here idea, was implemented. Simplified coarse mesh thermal hydraulics was used, which introduces a significant degree of averaging. Due to the lack of adequate variance reduction methodology, the authors have also used a coarse mesh for estimating the power distribution. A potential pitfall is the use of tallies for tracing the particle location. This method is computationally expensive and was not used in this work. Instead a custom build tallying subroutine with bin structure optimized for dealing with reactor core lattices was developed and particle location was tracked directly using the absolute coordinates. Therefore, the standard tallying subroutines and bin structures in MCNP were not used. The differences between the standard and modified MCNP input reported in [12], under normal circumstances should not be present. According to the authors the scheme was applied to a problem consisting of multiple assemblies, however, each assembly is treated as a single channel, therefore, simplifying the coupled calculation immensely by both reducing the number of tally bins and using a simplified thermal hydraulics model.

An internal thermal hydraulics module was implemented in [15]. Unfortunately the MC21 Monte Carlo reactor physics code is not available for use outside the Knolls Atomic Power laboratory.

Application of the internal coupling scheme to the quarter core PWR UOX-MOX benchmark problem

10.1 Validation of the geometry modeling with the benchmark reference solutions

To verify that no mistakes were done when modeling the material and the geometry distributions, the 2D HZP benchmark exercise was done. In this case, reflective boundary conditions are imposed on the axial bounding planes and the geometry cut planes. Vacuum boundary conditions are imposed on the lateral surfaces. The thermal hydraulic conditions are held fixed. The entire core has a homogeneous temperature of 560 K. The moderator density is 0.75206 g/cm^3 and the soluble boron concentration is 1000 ppm. An analog MCNP calculation with total of 2×10^9 histories was run. The results were compared against the benchmark data. Namely: **DeCART** 47 energy groups heterogeneous transport solution provided by the Seoul National University and KAERI, Korea (last update: February 1, 2006) and **DORT** 16 energy groups heterogeneous transport solution, provided by GRS, Germany (last update: February 1, 2006) [63],[64], [76], [77]. Unfortunately the **MCNP** data provided by the benchmark participants contains information only about the eigenvalue.

The core loading pattern is shown in the following figure fig. 10.2. To prevent power peaking in the pins at the boundary between MOX and UOX fuel elements, pins of different enrichment are used. The power peaking is caused by the different spectra, this is illustrated in fig. 10.1. In particular, the flux depression due to the large absorption resonance of ${}_{94}^{240}\text{U}$ at 1eV is clearly seen.

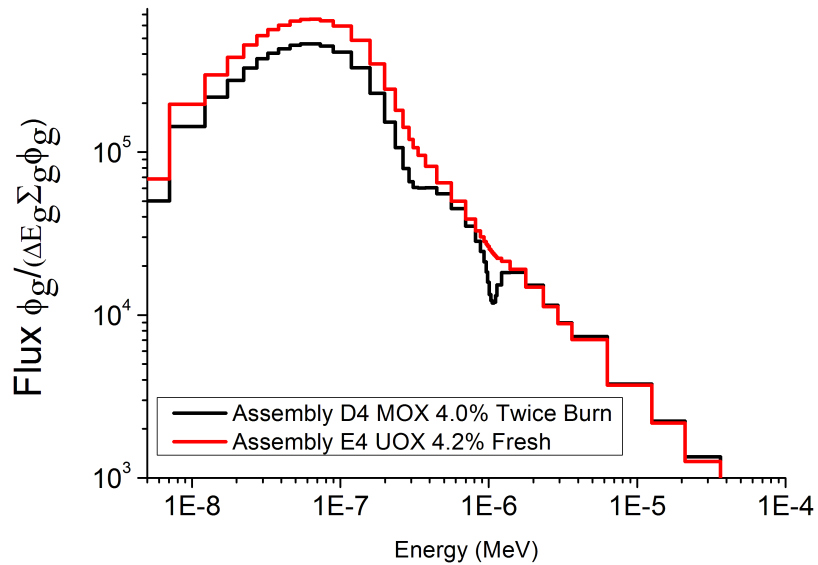


Figure 10.1: Neutron spectrum in the twice burn MOX assembly **D4** and the fresh UOX assembly **E4** plotted as function of energy.

The large thermal cross sections of the plutonium isotopes cause a clear shift in the spectrum. If pins with uniform enrichment were used, large power peaking in the MOX pins located at the periphery would have been observed.

	1	2	3	4	5	6	7	8
A	U 4.2% (CR-D) 35.0	U 4.2% (CR-A) 0.15	U 4.2% (CR-A) 22.5	U 4.5% (CR-A) 0.15	U 4.5% (CR-SD) 37.5	M 4.3% (CR-SD) 17.5	U 4.5% (CR-C) 0.15	U 4.2% (CR-C) 32.5
B	U 4.2% (CR-A) 0.15	U 4.2% (CR-A) 17.5	U 4.5% (CR-C) 32.5	M 4.0% (CR-C) 22.5	U 4.2% (CR-SD) 0.15	U 4.2% (CR-SB) 32.5	M 4.0% (CR-B) 0.15	U 4.5% (CR-B) 17.5
C	U 4.2% (CR-A) 22.5	U 4.5% (CR-A) 32.5	U 4.2% (CR-C) 22.5	U 4.2% (CR-C) 0.15	U 4.2% (CR-SD) 22.5	M 4.3% (CR-SD) 17.5	U 4.5% (CR-B) 0.15	M 4.3% (CR-B) 35.0
D	U 4.5% (CR-C) 0.15	M 4.0% (CR-C) 22.5	U 4.2% (CR-B) 0.15	M 4.0% (CR-B) 37.5	U 4.2% (CR-SD) 0.15	U 4.5% (CR-SC) 20.0	M 4.3% (CR-B) 0.15	U 4.5% (CR-B) 20.0
E	U 4.5% (CR-SD) 37.5	U 4.2% (CR-A) 0.15	U 4.2% (CR-C) 22.5	U 4.2% (CR-C) 0.15	U 4.2% (CR-D) 37.5	U 4.5% (CR-SD) 0.15	U 4.2% (CR-SA) 17.5	
F	M 4.3% (CR-SD) 17.5	U 4.2% (CR-SB) 32.5	M 4.3% (CR-C) 17.5	U 4.5% (CR-SC) 20.0	U 4.5% (CR-SD) 0.15	M 4.3% (CR-SD) 0.15	U 4.5% (CR-SD) 32.5	
G	U 4.5% (CR-C) 0.15	M 4.0% (CR-B) 0.15	U 4.5% (CR-B) 0.15	M 4.3% (CR-B) 0.15	U 4.2% (CR-SA) 17.5	U 4.5% (CR-SD) 32.5	Assembly Type CR Position Burnup [GWd/t]	
H	U 4.2% (CR-SD) 32.5	U 4.5% (CR-A) 17.5	M 4.3% (CR-C) 35.0	U 4.5% (CR-SD) 20.0			Fresh Once Burn Twice Burn	

CR-A Control Rod Bank A
 CR-B Control Rod Bank B
 CR-C Control Rod Bank C
 CR-D Control Rod Bank D
 CR-SA Shutdown Rod Bank A
 CR-SB Shutdown Rod Bank B
 CR-SC Shutdown Rod Bank C
 CR-SD Shutdown Rod Bank D
 O Ejected Rod

Figure 10.2: The PWR MOX-UOX core loading pattern as given by [63].

The eigenvalues computed by **MCNP** and **DeCART** showed good agreement. In the case of **DORT** the observed difference was larger shown in table 10.1. Since Monte Carlo transport provides an accurate solution with almost no approximations, differences between the stochastic and the deterministic solutions are to be expected. In general, the **DeCART** has higher fidelity when compared to **DORT**. **DeCART** does not involve a priori homogenized few-group constant generation, but uses online cross section generation. In order to deal with the heterogeneity at the pin cell level, the method of characteristic (MOC) is used and the multigroup cross section data is obtained directly from a cross section library that is normally used in lattice transport codes [78],[79],[80]. In the case of **DORT** pin cell homogenized with 16 energy groups and P_1 scattering expansion was used. S_{1-4} quadrature was used for representing the angular dependence.

Table 10.1: Eigenvalue estimates

MCNP	1.05858 (2)	Continuous energy
DeCART	1.05852 (0)	47 Energy groups MOC
DORT	1.06036 (0)	16 Energy groups S_n

In addition, the assembly averaged power and the pin power distributions for the diagonal assemblies, for which the data is available, was compared. The results are shown in table 10.2 and table 10.3. In both the cases **MCNP** predicted higher power towards the core periphery. The differences in the assembly power are of the same order of magnitude for both comparisons and follow similar patterns. These differences might be explained by the fact that in the **MCNP** calculation the reflector was modeled precisely by the defining reflector water volume and separate steel baffle.

Table 10.2: Assembly power relative difference between **DeCART** and **MCNP** given in %.

	1	2	3	4	5	6	7	8
A	3.77	4.08	3.20	1.81	0.08	-1.50	-2.42	-2.19
B	4.11	3.97	2.99	1.05	0.26	-1.54	-2.76	-2.00
C	3.20	3.01	2.26	1.04	-0.50	-2.17	-2.76	-2.72
D	1.86	1.10	1.11	-0.13	-0.76	-2.01	-2.83	-1.72
E	0.13	0.20	-0.41	-0.66	-1.87	-2.15	-2.09	
F	-1.38	-1.63	-2.05	-1.97	-2.09	-2.33	-1.58	
G	-2.34	-2.75	-2.82	-2.74	-2.02	-1.54		
H	-2.36	-2.14	-2.61	-1.96				

It should be taken into account that the maximum statistical uncertainty for the entire set of tally bins accumulated during the **MCNP** calculation was less than 1%. Therefore, the differences between the stochastic and the deterministic calculations are not due to poor variance. To ensure proper convergence of the fission source, the initial run was done and the accumulated fission source was used for the final calculation. As shown by the fission matrix calculations carried out in chapter five, the dominance ratio of the system under consideration is high and special care should be taken to avoid bias due to an ill converged initial source distribution. Close observation of the relative errors listed in table 10.2 and table 10.3

reveals that they have a symmetric distribution, proving that the solution is symmetric when comparing the values across the diagonal.

Table 10.3: Assembly power relative difference between **DORT** and **MCNP** given in %.

	1	2	3	4	5	6	7	8
A	2.82	2.16	1.65	0.87	0.41	-1.43	-1.82	-1.41
B	2.19	1.97	1.67	0.71	-0.03	-0.71	-2.47	-1.77
C	1.65	1.69	1.18	0.66	0.04	-1.27	-1.52	-1.59
D	0.91	0.76	0.73	0.91	-0.09	-0.82	-2.02	-1.31
E	0.47	-0.02	0.13	0.00	0.16	-0.89	-0.96	
F	-1.31	-0.70	-1.14	-0.70	-0.84	-1.45	-0.40	
G	-1.75	-2.46	-1.58	-1.94	-0.89	-0.36		
H	-1.61	-1.92	-1.49	-1.25				

In addition to the assembly averaged powers, the pin power distribution for the diagonal assemblies are shown in fig. 10.3 and fig. 10.4. In the case of **DORT** the difference has definite a structured pattern. In the case of **DeCART** a tilt of the pin power distribution is observed, this is most notable in assemblies **C3** , **D4** and **E5** .

In general, the agreement with the benchmark results is fairly good and it can be safely assumed that the geometry and the material modeling was properly done. Due to the difference in the mathematical modeling of the neutron transport, differences are to be expected.

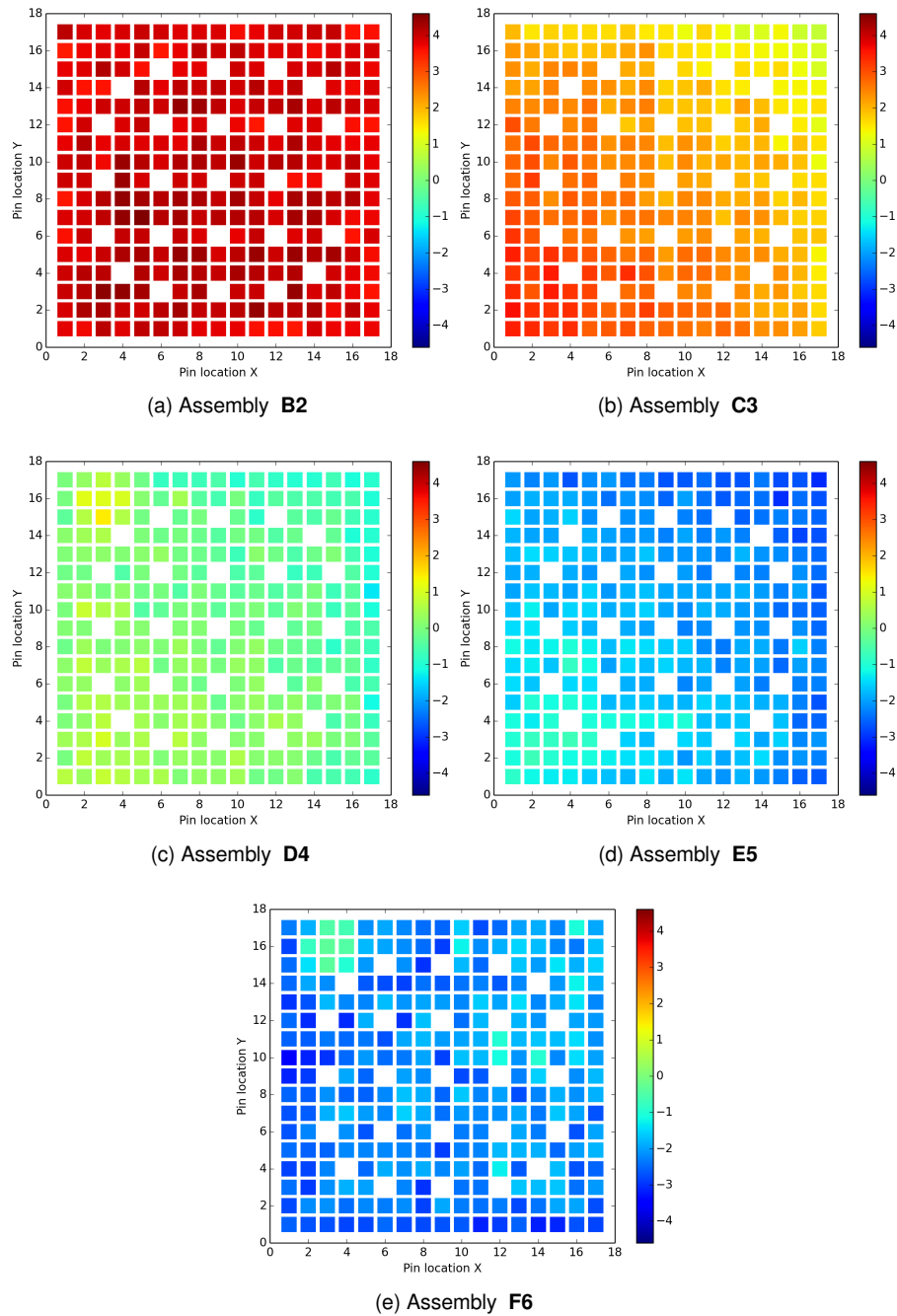


Figure 10.3: Relative difference of the pin power distribution of the diagonal assemblies between **DeCART** and **MCNP** given in %.

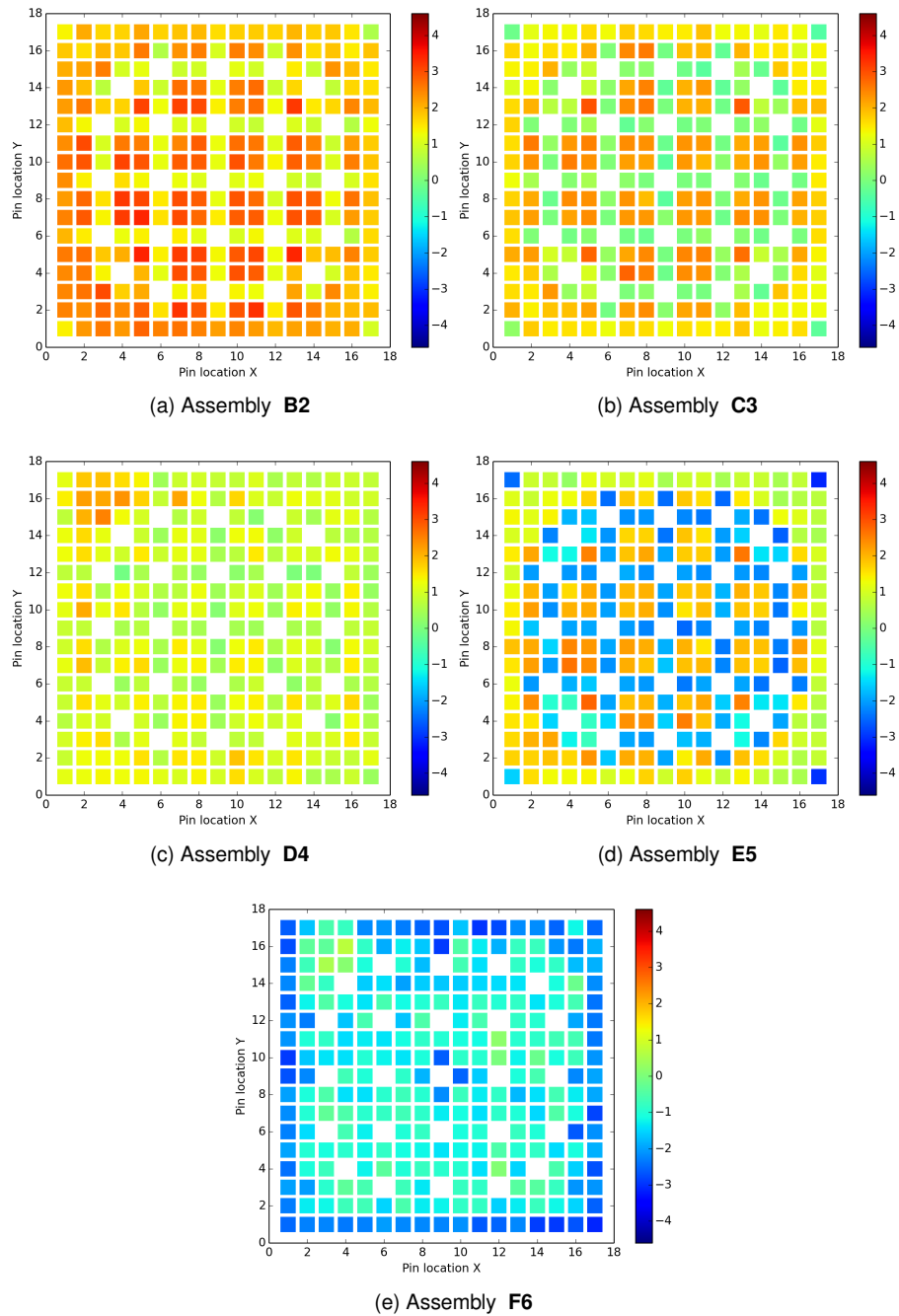


Figure 10.4: Relative difference of the pin power distribution of the diagonal assemblies between **DORT** and **MCNP** given in %.

10.2 Simulation of the PWR MOX-UO₂ benchmark with the internal coupling MCNP - SUBCHANFLOW

The internal coupling was applied to the hot full power case of the PWR MOX/UO₂ benchmark [63]. The full definition of the benchmark was used and no approximations were assumed. To avoid user induced mistakes, the material specifications and the geometry data of the benchmark was processed with the PIRS preprocessor for **MCNP** [81]. Pin by pin thermal hydraulics was coupled to the three dimensional Monte Carlo neutron transport. To tally the fission heat deposition each pin was subdivided into twenty equally sized volumes. **JEFF3.1.1** Doppler- broadened data prepared at 50K increments was used and the temperature dependence of the single differential data was corrected using the pseudo material mixing approach. The temperature dependence of the thermal scattering data was corrected using on-the-fly direct interpolation. The variance of the power estimate was improved using the UFS method. The UFS mesh with resolution of quarter of an assembly was used. The fission source redistribution function (8.11) was tallied over the inactive cycles. To speed up the calculations the Wielandt acceleration was used only to converge the fission source distribution and was disabled during the active cycles. The shift parameter k_e can be effectively estimated using the eigenvalue from the previous coupled iteration, since the eigenvalue of the coupled system computed in the current iteration is close to the eigenvalue computed during the previous iteration. The fission source convergence according to the Shannon entropy criterion was met within 20 criticality cycles for all the **MCNP** runs. Disabling the Wielandt acceleration restores the original dominance ratio of the system. Using the stochastic approximation technique, this effect is corrected and results in no negative effects in contrast to the standalone calculations. The final estimate of the power profile is the combination of all the power profile estimates during the N coupled iterations, taken with weight $1/N$. Therefore, the combined power profile has the combined statistics from all the runs and does not suffer from the deficiencies of the usual standalone criticality calculations. This result is a unique consequence of the relaxation scheme, that further justifies its effectiveness. Moreover, in the chapter on variance reduction it shown that by using the UFS scheme it is possible to reach results that are on average close to the ones obtained by using the Wielandt method.

This coupled calculation would have been impossible if coupling via the input files had been used. This would have resulted in millions of lines of **MCNP** input. These massive inputs take unacceptably long time for **MCNP** to process. For comparison, a nine assembly **MCNP** input having the same resolution as the one used for the current model takes three hours to be processed. In contrast the internal coupling takes about six minutes to set up the problem, where most of the time is lost reading the cross section data. To further improve the file I/O the cross section data was stored in binary format.

Each coupled iteration was run with a total of 1×10^9 histories and an ensured maximal variance of 1.9% over all tally bins. This quality of the tally estimates would have been difficult to achieve if analog transport had been used, especially taking into account that approximately

3×10^5 tally bins were accumulated. In principle, since the power profile in the current run is a weighted sum of the power profiles from the previous runs, any desired convergence can be achieved and the utilization of the UFS scheme at first glance might seem unnecessary. In practice, to suppress the large statistical uncertainties a significant number of coupled iterations would be needed. The variance reduction has the effect of reducing the propagated uncertainties from equation (9.6). Numerical tests on smaller models showed that improving the variance using UFS in addition to the stochastic approximation scheme reduces the number of coupled iteration needed by more than a half before the same degree of convergence is reached.

The coupled calculation was stopped after reaching $\epsilon = 0.16\%$ and completing $N = 23$ coupled iterations. The value of ϵ should be regarded as an additional uncertainty on the power estimate. As evident from fig. 10.5 the convergence parameter behaves as N^{-1} , as expected by the theory of stochastic approximation. The same figure also shows the pin power distribution.

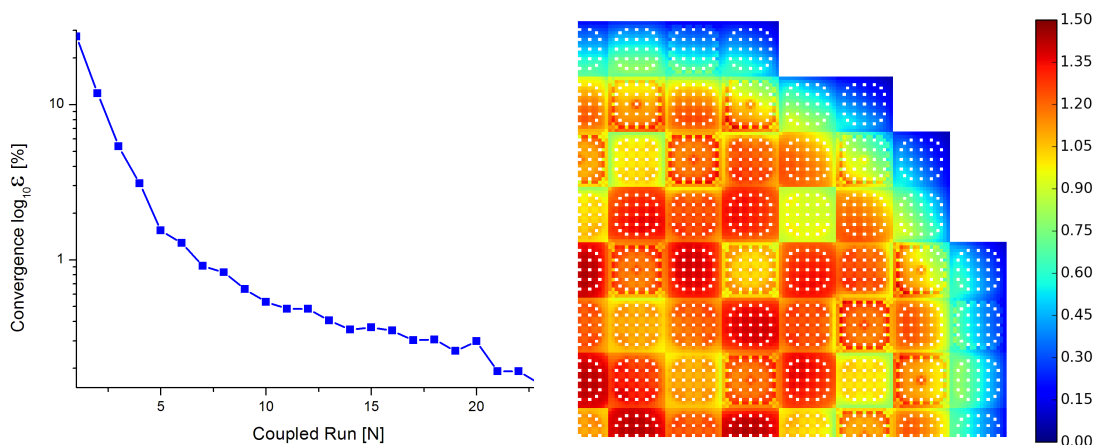


Figure 10.5: Convergence ϵ as a function of the coupled iteration N and two dimensional pin power distribution.

The results from the internal coupling between **MCNP** and **SUBCHANFLOW** were compared against the PARCS two energy groups nodal diffusion solution provided by the Purdue University, USA (last update: February 1, 2006) and the SKETCH-INS two energy groups nodal diffusion solution provided by JNES, Japan (last update: February 1, 2006). For comparing the axial averaged power profile, the eight and the two energy groups PARCS solutions were used. The eight energy groups PARCS solution does not provide pin by pin data, only the total assembly power was compared.

The comparison of the axial core averaged power distributions and the core averaged fuel temperature distributions is shown in fig. 10.7. Both parameters show good agreement with the data available from the benchmark. Due to the high pressure in the system of 15.5 MPa, the axial variation of the coolant density was limited. Therefore the change of the moderation in the coolant was not strong enough to induce strong power shift towards the core inlet.

The situation would have been much different if a **BWR** geometry had been simulated. An example of a large power shift due to boiling in the upper plenum are shown in [2]. The three dimensional fuel temperature and coolant density are shown in fig. 10.6.

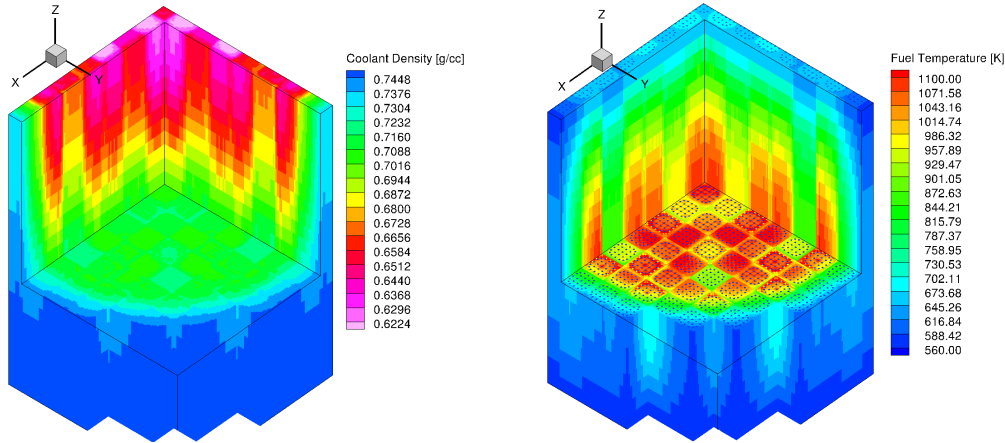


Figure 10.6: Three dimensional coolant density and fuel temperature distributions, having single fuel pin resolution, computed by the coupled system **MCNP - SUBCHANFLOW** .

It is interesting to note that the fuel temperature predicted with SKETCH-INS does not coincide by the values provided by **MCNP - SUBCHANFLOW** and PARCS-8G, where the power shows very good agreement. This also holds for the regions having the lowest power i.e. the lower and uppermost core slices, which suggests that different thermal conduction models were most probably used in SKETCH-INS.

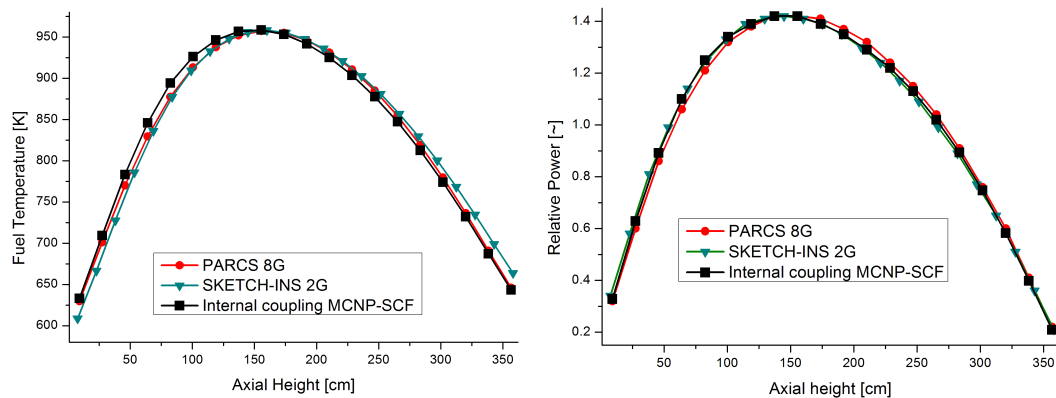


Figure 10.7: Core averaged fuel Doppler temperature and power distributions plotted as functions of the core height.

The comparison of the pin and assembly power distributions is shown in table 10.4, figs. 10.8(a) to 10.8(f), table 10.5, table 10.6 and figs. 10.9(a) to 10.9(f). In all the cases, the differences increase approaching the core periphery. One possible explanation is the anisotropic effect present near reflectors that violates the assumptions of diffusion theory. In addition, to fulfill the condition of a low leakage core once and twice burned assemblies

are located at the core periphery. The difference between PARCS 2 and 8 groups and **MCNP** is smaller than the difference between **MCNP** and **SKETCH-INS 2G**. These differences are to be expected since a very precise and very approximate solution are compared. Never the less, the differences are not large. This fairly good agreement might be explained with the fact that no control rods are inserted and the core represents a standard PWR core loading. The absence of control rods and heterogeneities typical for the modern designs, such as generation four reactors, ensures that the conditions for applying the diffusion approximation hold. For instance, if a reduced moderated **PWR** having axial and radial breeding blankets [82] was considered. The differences with respect to the reference deterministic calculations provided by the benchmark participants are shown hereafter and are computed using the following formula

$$\text{Difference} = 100 \times \frac{\text{Daterminisitc case} - \text{MCNP}}{\text{Daterminisitc case}} \quad (10.1)$$

Table 10.4: Assembly power relative difference between **SKETCH-INS 2G** and **MCNP** given in %.

	1	2	3	4	5	6	7	8
A	-3.59	-3.92	-2.95	-1.48	-0.13	1.94	3.61	3.45
B	-3.91	-3.36	-2.27	-1.32	-0.73	1.19	2.58	3.81
C	-2.93	-2.26	-2.14	-1.08	-0.42	0.47	3.45	3.73
D	-1.51	-1.37	-1.09	0.14	-0.74	0.27	1.24	2.41
E	-0.27	-0.86	-0.51	-0.79	-0.31	1.01	1.49	
F	1.71	1.06	0.39	0.22	0.98	-1.51	-0.01	
G	3.53	2.49	3.40	1.19	1.49	0.05		
H	3.39	3.79	3.65	2.36				

Table 10.5: Assembly power relative difference between **PARCS 2G** and **MCNP** given in %.

	1	2	3	4	5	6	7	8
A	-1.99	-2.27	-1.37	-0.66	0.34	0.61	1.37	2.01
B	-2.26	-2.01	-0.90	-0.15	0.01	1.09	0.50	1.97
C	-1.35	-0.89	-0.74	-0.18	0.06	0.52	1.55	2.71
D	-0.69	-0.20	-0.19	0.71	-0.04	0.19	-0.13	1.35
E	0.20	-0.12	-0.02	-0.08	0.29	-0.12	0.00	
F	0.37	0.96	0.44	0.14	-0.15	-1.13	0.13	
G	1.29	0.41	1.48	-0.18	-0.01	0.19		
H	1.95	1.95	2.63	1.30				

Table 10.6: Assembly power relative difference between **PARCS 8G** and **MCNP** given in %.

	1	2	3	4	5	6	7	8
A	-0.65	-1.32	-0.52	-0.18	0.83	-0.17	0.80	1.55
B	-1.31	-1.05	-0.08	-0.18	0.27	1.19	-0.99	1.38
C	-0.50	-0.07	-0.04	0.26	0.43	-0.25	0.98	1.72
D	-0.21	-0.23	0.24	0.93	0.18	0.16	-1.59	1.24
E	0.69	0.14	0.35	0.14	0.70	-0.32	-0.06	
F	-0.41	1.06	-0.32	0.11	-0.35	-2.52	0.20	
G	0.72	-1.08	0.93	-1.64	-0.06	0.26		
H	1.49	1.36	1.64	1.19				

The final estimated value for the eigenvalue was $k_{\text{eff}} = 0.99981$ at 1600 ppm of soluble boron concentration. The pin power distribution also shows a difference with respect to the benchmark data. These differences are in most of the cases within $\pm 3\%$ and are in good agreement with the benchmark data. It should be taken into account that the pin power distributions are tallied directly by **MCNP**. Whereas in the case of deterministic codes the pin power distribution is reconstructed using the data from the nodal calculation and the data available from the lattice calculation used to produce the homogenized cross sections [83], [84]. The pin data is normalized by dividing by the mean. Using this normalization to obtain the pin power one should multiply the corresponding pin power value by the corresponding assembly power.

The pin powers have different magnitudes but close observation shows a similar pattern. This can be explained with the fact that the both deterministic codes used similar pin power reconstruction methodology for calculating the pin powers.

In addition to the power distribution data, the distributions of the assembly averaged fuel temperature, the assembly averaged coolant temperature and the coolant densities were compared. For the latter two quantities no comparison is shown because the difference is less than 1.0% for all the values. In the case of the internal coupling **MCNP** - SCF the assembly averaged quantities were computed by computing the average of the heterogeneous data obtained from the subchannel calculation. In the case of **PARCS** and **SKETCH-INS 2G** coarse mesh thermal hydraulics was used. The comparison is shown in table 10.7, table 10.9, table 10.9. Good agreement was found in all the cases compared.

Table 10.7: Assembly averaged fuel temperature relative difference between **SKETCH-INS 2G** and **MCNP** given in %.

	1	2	3	4	5	6	7	8
A	-0.88	-1.02	1.21	-1.91	0.16	-2.22	1.55	1.89
B	-1.02	-2.42	0.06	-3.66	1.62	2.76	-2.19	-4.17
C	1.23	0.06	1.11	-0.05	0.44	-2.06	1.89	0.64
D	-1.92	-3.69	-0.06	-5.83	2.14	1.94	-5.60	7.03
E	0.09	1.55	0.39	2.11	4.62	0.42	-9.36	
F	-2.37	2.69	-2.11	1.91	0.41	3.80	11.95	
G	1.51	-2.24	1.85	-5.63	-9.36	11.96		
H	1.87	-4.18	0.61	7.03				

Table 10.8: Assembly average fuel temperature relative difference between **PARCS 2G** and **MCNP** given in %.

	1	2	3	4	5	6	7	8
A	-0.63	-0.13	-0.13	0.87	0.68	-2.43	1.41	0.69
B	-0.12	-0.35	0.03	-3.02	1.06	1.04	-2.49	0.81
C	-0.11	0.03	0.22	1.05	0.77	-2.57	1.47	-0.67
D	0.86	-3.05	1.04	-2.31	0.99	0.78	-2.80	0.38
E	0.60	0.98	0.72	0.96	0.59	0.54	0.09	
F	-2.58	0.96	-2.63	0.75	0.52	-3.00	0.04	
G	1.37	-2.55	1.44	-2.84	0.08	0.05		
H	0.68	0.80	-0.70	0.37				

Table 10.9: Assembly averaged fuel temperature relative difference between **PARCS 8G** and **MCNP** given in %.

	1	2	3	4	5	6	7	8
A	0.25	0.61	0.48	1.29	1.02	-2.85	1.13	0.57
B	0.61	0.35	0.57	-2.95	1.31	1.15	-3.33	0.63
C	0.49	0.58	0.73	1.43	1.08	-2.99	1.20	-0.97
D	1.27	-2.98	1.42	-2.11	1.22	0.84	-3.57	0.37
E	0.95	1.23	1.03	1.19	0.87	0.49	0.11	
F	-3.00	1.09	-3.05	0.80	0.47	-3.64	0.07	
G	1.09	-3.39	1.17	-3.61	0.11	0.08		
H	0.55	0.62	-1.00	0.36				

As seen from table 10.7, there are insignificant differences in the fuel temperature between **MCNP - SUBCHANFLOW** and **SKETCH-INS 2G**. There are similarly large differences between the benchmark reference solution of **PARCS 8G** and **SKETCH-INS 2G**. The comparison is shown in table 10.10 and table 10.11.

Table 10.10: Assembly power relative difference between **SKETCH-INS 2G** and **PARCS 8G** given in %.

	1	2	3	4	5	6	7	8
A	-3.03	-2.68	-2.52	-1.40	-1.07	2.01	2.73	1.83
B	-2.68	-2.40	-2.29	-1.25	-1.11	-0.10	3.44	2.35
C	-2.52	-2.29	-2.21	-1.44	-0.96	0.61	2.39	1.94
D	-1.40	-1.25	-1.44	-0.90	-1.03	0.01	2.68	1.08
E	-1.07	-1.11	-0.96	-1.03	-1.12	1.22	1.44	
F	2.01	-0.10	0.61	0.01	1.22	0.88	-0.31	
G	2.73	3.44	2.39	2.68	1.44	-0.31		
H	1.83	2.35	1.94	1.08				

Table 10.11: Assembly averaged fuel temperature relative difference between **SKETCH-INS 2G** and **PARCS 8G** given in %.

	1	2	3	4	5	6	7	8
A	-0.77	-1.17	0.51	-2.29	-0.58	0.42	0.29	0.80
B	-1.17	-1.94	-0.35	-0.47	0.23	1.09	0.76	-2.91
C	0.51	-0.35	0.27	-1.06	-0.46	0.63	0.47	0.96
D	-2.29	-0.47	-1.06	-2.45	0.66	0.78	-1.31	4.03
E	-0.58	0.23	-0.46	0.66	2.54	-0.05	-5.72	
F	0.42	1.09	0.63	0.78	-0.05	4.79	7.17	
G	0.29	0.76	0.47	-1.31	-5.72	7.17		
H	0.80	-2.91	0.96	4.03				

These differences can not be easily explained because the details of the thermal hydraulic modeling in **SKETCH-INS 2G** are not available. The overall behavior of the difference is similar to table 10.7. Close observation also shows that the difference in fuel temperature in some cases does not exactly match the difference in power. This is due to the different heat conduction models used for the fuel by the thermal hydraulic codes.

In this comparison the results of the newly developed coupled code system **MCNP - SUB-CHANFLOW** were compared to the international PWR UOX-MOX benchmark. Since low order diffusion approximation, where the angular dependence is ignored is compared to high resolution transport, one can ask whether the validation is credible. To answer this question, one has to understand in detail the main idea of the internal coupling. Namely, that the methodology of introducing the thermal hydraulic feedback is completely identical to the standard **MCNP** input. This was proven in special research paper [71]. Meaning, that the internal coupling is an advanced method of introducing internal mesh, which delivers the same results as the standard **MCNP** input by supply the information via the memory and avoiding using external input. Therefore, the accuracy and the physics of the validated general purpose Monte Carlo code **MCNP** is not altered. Or alternatively formulated, the same results could have been obtained at the expense of creating massive input files, containing explicitly defined pseudo materials, and waiting many hours for **MCNP** to process them and to load the information in the memory.

Since the internal coupling is not the sole code modification, one might argue that the newly implemented UFS method, the Wielandt acceleration or the thermal scattering data are introducing errors. The Wielandt method was extensively verified by comparing it to the standard **MCNP** calculation and it was proven to be consistent in all the cases. Moreover, since the Wielandt acceleration is used only during the inactive cycles of the coupled calculation, even if it was erroneous the final results would have not been biased, because the inactive initial cycles used to converge the fission source are not reflected in the final estimate and the source distribution is continuously updated after each criticality cycle. The only problem would have been a not sufficiently converged fission source distribution and an error message from **MCNP** regarding the standard deviation of the Shannon entropy. No such error messages were detected.

Since the pseudo material mixing performed by the internal coupling is completely equivalent to the standard pseudo material mixing done via the input files, no errors are possible. The pseudo Material mixing is a standard technique used in **MCNP** and is well accepted and validated with respect to experimental data [74]. The only potential error might come from the new methodology for interpolating the thermal scattering data. This methodology is extensively tested and consistent results are reported in both Chapter 4 and in [85].

The tally subroutine is a highly optimized equivalent of the standard **MCNP** tallies and was proven to deliver completely identical values as the standard **MCNP** tallies. Regarding the introduction of nonanalog transport, the consistency of the newly implemented UFS method was validated against the GVR scheme. The maximum difference observed over all the 3×10^5 tally bins was 3%. The eigenvalues were identical and the absolute difference was less than the statistical uncertainty table 8.2.

Therefore, each step of the coupled calculation can be verified and proven correct both as single units and as an integrated system. Much can be said about the quality of the results by taking into account the precise nature of the code modifications. The difference between the deterministic and the Monte Carlo solutions of the benchmark are therefore due to the much less accurate deterministic solution. Since the test problem is precisely formulated so that the assumptions utilized by the deterministic code are valid, the deterministic solution is close to the full transport Monte Carlo solution. The situation would have been much different if heterogeneous core with control rods inserted or an advanced design with breeding blankets and seed assemblies was used. For this case, the anisotropy assumption would no longer be true and the deterministic codes are known to fail in the regions where strong anisotropy exists. Nevertheless, as part of a future study the scheme can be compared with respect to experimental data, but this goes beyond the scope of this thesis and is not an urgent issue.

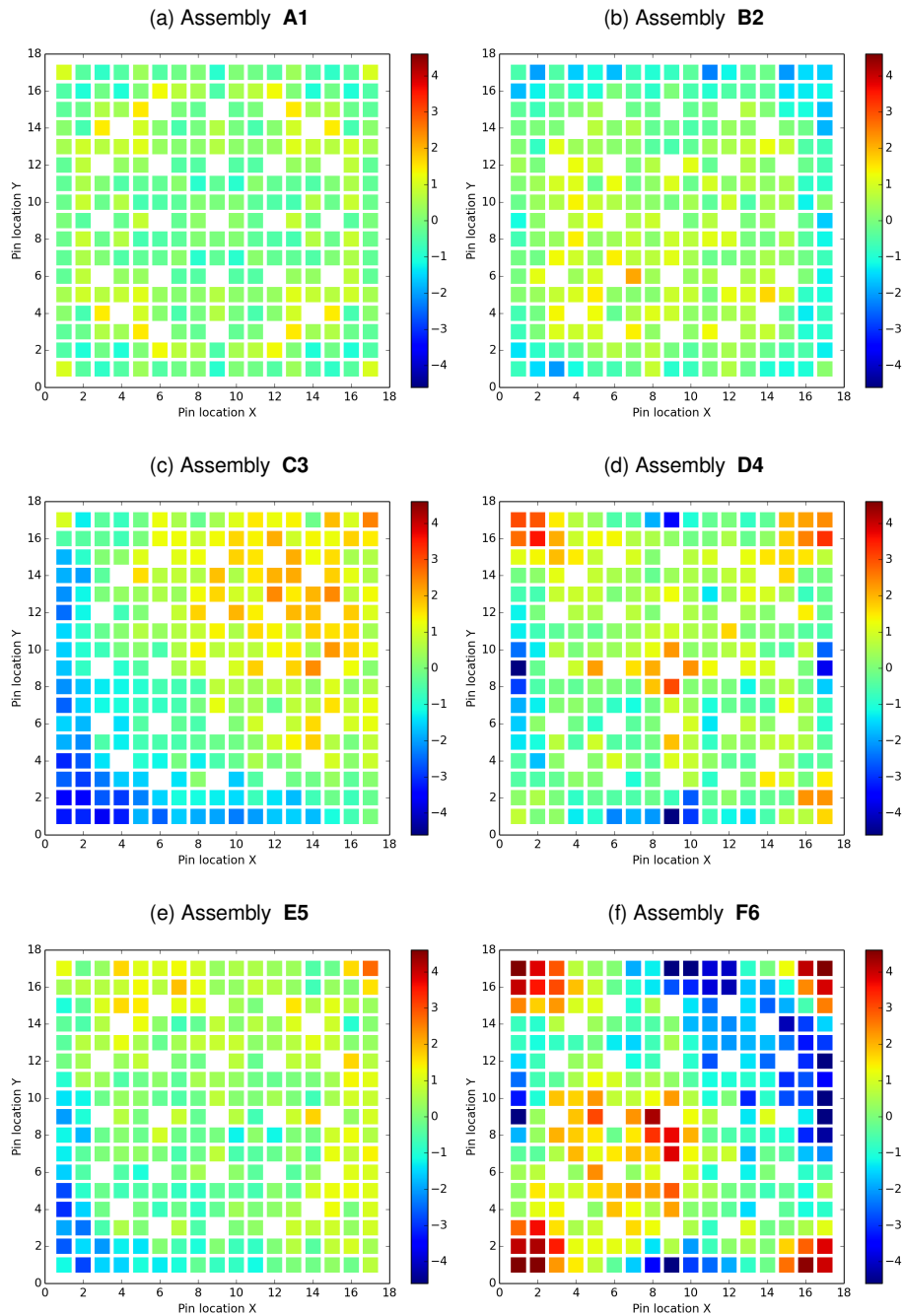
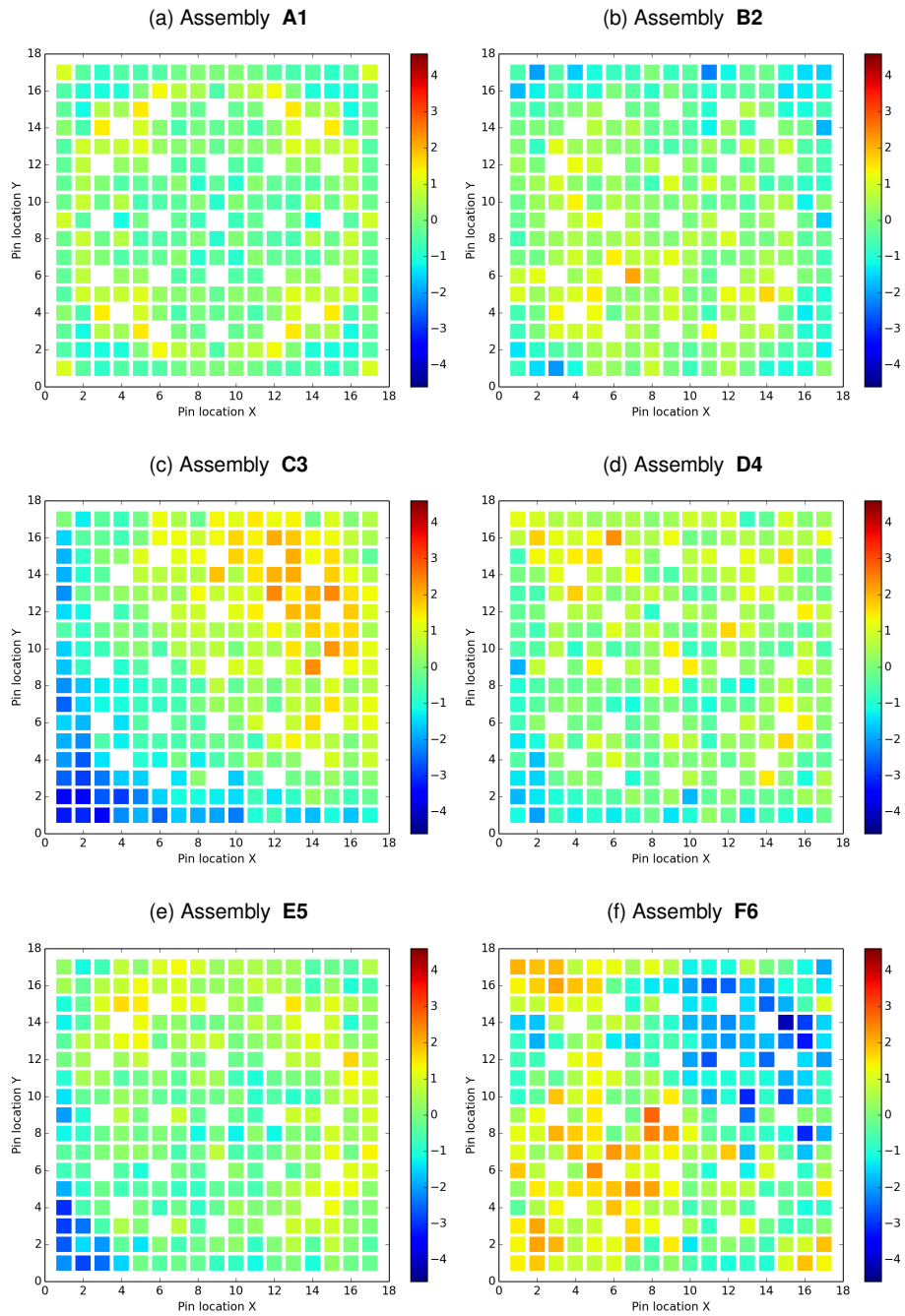
Figure 10.8: Relative difference of the pin power distribution between **SKETCH-INS 2G** and **MCNP** given in %.

Figure 10.9: Relative difference of the pin power distribution between **PARCS 2G** and **MCNP** given in %.



Monte Carlo based depletion calculations

Monte Carlo codes have been linked to depletion modules [16], [17], [18], [19], [20], [21] and [22]. Those coupled systems use either external depletion codes or internal modules. The depletion capability significantly broadens the scope of Monte Carlo codes by simulating the time dependence of nuclear inventories using accurate estimates of the neutron flux distribution. The main disadvantage Monte Carlo based depletion calculations have been the significant computational effort to obtain accurate estimates of the neutron flux distribution and the reaction rates needed by the depletion modules. Therefore, application of those codes has been limited to problems of modest complexity. Another major issue that has prohibited the wide application of Monte Carlo based depletion systems is the numerical stability of the algorithms used for solving the depletion equation system [86]. This is especially problematic when simulating three dimensional depletion problems [87], [23]. This instability is due to solving the depletion equation system by explicit methods [88], [89] and [90]. This problem results in an inaccurate flux distribution and is not due to the variance of the Monte Carlo flux estimate. The stability of the explicit schemes can be in principle improved by using fine discretization i.e. small depletion steps. Due to the significant computational effort required by Monte Carlo this is not a very efficient strategy. Another problem is the efficient information exchange between the stochastic transport code and the depletion modules. Both the stability of the depletion calculation and the efficient code to code data interchange are addressed in this thesis. The backward Euler method is used as an alternative to the explicit schemes. Being an unconditionally stable, the method can be used to increase the depletion step size and ensure accurate solution. The stochastic approximation scheme was applied to solve the non linear equations arising when applying the backward Euler method. This strategy has been shown to stabilize the depletion calculation even when using depletion steps larger than one month [91].

11.1 Fuel depletion calculations

The long term reactor evolution is governed by the changes in composition due to fuel depletion and the manner in which these are compensated. The objective of the depletion calculation is to determine the evolution of the isotope field $n_i(\mathbf{r}, t)$ as a function of time. The spatial dependence of the nuclide field subsequently determines the distribution of the neutron flux both as a function of energy and coordinates. Each fission event usually produces two intermediate mass nuclei, in addition to releasing two or three neutrons. The mass spectrum of the fission products is determined by the double peak distribution having a maxima at about 100 and 140 amu. The fission products are neutron rich and have a large probability of undergoing β^+ or β^- decay. Some of the fission products like ^{135}Xe and ^{149}Sm have large thermal absorption cross sections and strongly effect the reactivity. The general equations [31] governing the production and destruction of a fission product “i” are given by

$$\frac{dn_i(\mathbf{r}, t)}{dt} = \gamma_i \Sigma_i + \sum_i (\lambda^{j \rightarrow i} + \sigma^{j \rightarrow i} \phi) n_i(\mathbf{r}, t) - (\lambda^i + \sigma_a^i \phi) n_i(\mathbf{r}, t). \quad (11.1)$$

The above equations can be written in compact matrix form [91]

$$\frac{\mathbf{N}(\mathbf{r}, t)}{dt} = \mathbb{M}(\phi) \mathbf{N}(\mathbf{r}, t), \quad (11.2)$$

with

$$\mathbb{M}(\phi) = \int_0^\infty \phi(\mathbf{r}, E, t) \mathbb{X}(T(\mathbf{r}, t)) dE + \mathbb{D}. \quad (11.3)$$

Where \mathbb{X} is the cross section and fission yield matrix, \mathbb{D} is the decay matrix and $T(\mathbf{r}, t)$ is the temperature field. According to the theory [86] (11.2) is solved by

$$\mathbf{N}(\mathbf{r}, t) = \mathbf{N}_0(\mathbf{r}) \exp(\mathbb{M}(\phi) \Delta t) \quad (11.4)$$

Different methods have been implemented to compute the matrix exponential (11.4). The most recent implemented technique is the Chebyshev rational approximation method [92]. This method has been implemented in the **SERPENT** continuous energy Monte Carlo code. Equation (11.4) gives the nuclide concentration at the end of the depletion step. The most simple scheme is to use the the beginning of time constant flux approximation (**BOT**) given by algorithm 2.

Algorithm 2 Beginning of time constant flux approximation scheme.

```

1:  $\mathbf{N}(\mathbf{r}, t_0)$  ▷ Initial nuclide concentration
2: for  $\mathbf{n} \leftarrow 0:N$  do
3:    $\phi_n \leftarrow \phi_{\mathbf{B}}(\mathbf{N}(\mathbf{r}, t_n))$ 
4:    $\mathbf{N}(\mathbf{r}, t_{n+1}) \leftarrow \mathbf{N}(\mathbf{r}, t_n) \exp(\mathbb{M}(\phi_n) \Delta t_n)$ 
5: end for

```

Where $\phi_{\mathbf{B}}$ is the fundamental mode solution. Since the **BOT** scheme does not take into account the changes of the flux and the nuclide field that occur over the depletion step Δt_n , this method is conditionally stable, where the stability strongly depends on the depletion step size. This method was implemented in [18]. The strategy of the method can be readily illustrated by considering the following ordinary differential equation problem

$$\frac{dy}{dt} = f(t, y). \quad (11.5)$$

The **BOT** in this case would be similar to the explicit Euler method

$$y_{n+1} = y_n + f(t_n, y_n) \Delta t. \quad (11.6)$$

Other methods have been developed with the aim of enabling larger depletion steps, by correcting for the changes that occur over the depletion step. Integrating (11.5) from t_n to t_{n+1}

$$\int_{t_n}^{t_{n+1}} \frac{dy}{dt} dt = \int_{t_n}^{t_{n+1}} f(t, y) dt. \quad (11.7)$$

The above integral is solved using trapezoidal rule to obtain

$$\frac{y_{n+1} - y_n}{\Delta t} = \frac{f(t_n, y_n) + f(t_{n+1}, y_{n+1})}{2} + \mathcal{O}(\Delta t^2). \quad (11.8)$$

This is the Euler predictor-corrector method (**PC**), being an implicit method because information at step $n+1$ is needed to evaluate the right hand side. Instead of using $f(x_{n+1}, y_{n+1})$ a predictor value is used

$$\begin{aligned} \text{Predictor step: } y_* &= y_n + f(t_n, y_n) \Delta t + \mathcal{O}(\Delta t^2) \\ \text{Corrector step: } y_{n+1} &= y_n + \frac{(f(t_n, y_n) + f(t_*, y_*)) \Delta t}{2} + \mathcal{O}(\Delta t^2) \end{aligned} \quad (11.9)$$

The **PC** method has been implemented in many Monte Carlo based depletion systems [16], [20] and [93]. The following algorithm 3 is used.

Algorithm 3 The predictor-corrector scheme.

- 1: $\mathbf{N}(\mathbf{r}, t_0)$ ▷ Initial nuclide concentration.
 - 2: **for** $\mathbf{n} \leftarrow 0 : \mathbf{N}$ **do**
 - 3: $\phi_n \leftarrow \phi_{\mathbf{B}}(\mathbf{N}(\mathbf{r}, t_n))$
 - 4: $\mathbf{N}^*(\mathbf{r}, t_{n+1}) \leftarrow \mathbf{N}(\mathbf{r}, t_n) \exp(\mathbb{M}(\phi_n) \Delta t_n)$ ▷ Predictor step.
 - 5: $\phi_n \leftarrow \phi_{\mathbf{B}}(\mathbf{N}^*(\mathbf{r}, t_{n+1}))$
 - 6: $\mathbf{N}(\mathbf{r}, t_{n+1}) \leftarrow \mathbf{N}(\mathbf{r}, t_n) \exp(\mathbb{M}(\phi_n) \Delta t_n)$ ▷ Corrector step.
 - 7: $\mathbf{N}(\mathbf{r}, t_{n+1}) \leftarrow \frac{\mathbf{N}^*(\mathbf{r}, t_{n+1}) + \mathbf{N}(\mathbf{r}, t_{n+1})}{2}$ ▷ Combining the predictor and the corrector.
 - 8: **end for**
-

Although, both the above methods have been shown to give wrong results when applied to three dimensional depletion problems [23]. It is well known from the theory of the ordinary differential equations that the step size limitation can be lifted by using an implicit scheme. One such choice is the backward Euler method. At first glance it is similar to (11.6) besides one crucial modification, the right hand side is evaluated at time $n + 1$

$$y_{n+1} = y_n + f(t_{n+1}, y_{n+1}) \Delta t. \quad (11.10)$$

This modification changes the scheme completely. To obtain y_{n+1} in the general case, one has to solve a non linear problem. This can be done using different methods. In [91] it has been proposed to use a similar to the backward Euler method called the Stochastic Implicit Euler method **SIE**. Equation (11.4) can be transformed to nonlinear problem by noting that

$$\phi_{n+1} = \phi_{\mathbf{B}}(\mathbf{N}(\mathbf{r}, t_{n+1})). \quad (11.11)$$

Substituting (11.11) in (11.4) one obtains

$$\mathbf{N}(\mathbf{r}, t_{n+1}) = \mathbf{N}(\mathbf{r}, t_n) \exp(\mathbb{M}(\phi_{\mathbf{B}}(\mathbf{N}(\mathbf{r}, t_{n+1}))) \Delta t). \quad (11.12)$$

This equation is similar to the solution of the nonlinear problem that arises when using the backward Euler method (11.10). The root of the nonlinear equation can be estimated by the Stochastic Approximation Scheme. The depletion scheme corresponding to the **SIE** scheme with relaxation of the nuclear field is shown in algorithm 4.

Algorithm 4 The **SIE** implicit scheme with relaxation of the nuclide field.

```

1:  $\mathbf{N}(\mathbf{r}, t_0)$  ▷ Initial nuclide concentration.
2:  $\phi_0 \leftarrow \phi_{\mathbf{B}}(\mathbf{N}(\mathbf{r}, t_0))$ 
3: for  $i \leftarrow 0:N$  do
4:    $\bar{\mathbf{N}}^0(\mathbf{r}, t_{i+1}) \leftarrow \mathbf{N}(\mathbf{r}, t_i) \exp(\mathbb{M}(\phi_i) \Delta t)$ 
5:   for  $n \leftarrow 1:C$  do
6:      $\phi_{i+1}^n \leftarrow \phi_{\mathbf{B}}(\bar{\mathbf{N}}^{n-1}(\mathbf{r}, t_{i+1}))$ 
7:      $\mathbf{N}^n(\mathbf{r}, t_{i+1}) \leftarrow \mathbf{N}(\mathbf{r}, t_i) \exp(\mathbb{M}(\phi_{i+1}^n) \Delta t)$ 
8:      $\bar{\mathbf{N}}^n(\mathbf{r}, t_{i+1}) \leftarrow \frac{1}{n} \sum_{j=1}^n \mathbf{N}^j(\mathbf{r}, t_{i+1})$  ▷ Relaxation of the nuclide fields.
9:   end for
10:   $\mathbf{N}(\mathbf{r}, t_{i+1}) \leftarrow \bar{\mathbf{N}}^C(\mathbf{r}, t_{i+1})$ 
11:   $\phi_{i+1} \leftarrow \frac{1}{n} \sum_{j=1}^C \phi_{i+1}^j$ 
12: end for

```

According to the above algorithm, the **SIE** scheme is very similar to the scheme used in the coupled thermal hydraulics calculations where the power estimate is relaxed. The difference here is that the nuclide field is relaxed. As claimed in [87] the scheme allows longer time steps. Tests cases have been run with time steps of 60 days. The method of relaxing the

nuclide field is considered unstable because the fuel is depleted with the flux which might have large statistical errors [91]. In general, the effect of the large variances on the credibility of the calculation is not known. Therefore, a modified algorithm relaxing the neutron flux is proposed in algorithm 5. In this case the variance of the neutron flux is reduced with the number of inner iterations and every subsequent depletion calculation is run with an improved flux distribution.

Algorithm 5 The **SIE** implicit scheme with relaxation of the neutron flux.

```

1:  $\mathbf{N}(\mathbf{r}, t_0)$  ▷ Initial nuclide concentration.
2:  $\phi_0 \leftarrow \phi_{\mathbf{B}}(\mathbf{N}(\mathbf{r}, t_0))$ 
3: for  $i \leftarrow 0:N$  do
4:    $\bar{\mathbf{N}}^0(\mathbf{r}, t_{i+1}) \leftarrow \mathbf{N}(\mathbf{r}, t_i) \exp(\mathbb{M}(\phi_i) \Delta t)$ 
5:   for  $n \leftarrow 1:C$  do
6:      $\phi_{i+1}^n \leftarrow \phi_{\mathbf{B}}(\bar{\mathbf{N}}^{n-1}(\mathbf{r}, t_{i+1}))$ 
7:      $\bar{\phi}_{i+1}^n \leftarrow \frac{1}{n} \sum_{j=1}^n \phi_{i+1}^j$  ▷ Relaxation of the neutron flux.
8:      $\mathbf{N}^n(\mathbf{r}, t_{i+1}) \leftarrow \mathbf{N}(\mathbf{r}, t_i) \exp(\mathbb{M}(\bar{\phi}_{i+1}^n) \Delta t)$ 
9:   end for
10:   $\mathbf{N}(\mathbf{r}, t_{i+1}) \leftarrow \bar{\mathbf{N}}^C(\mathbf{r}, t_{i+1})$ 
11:   $\phi_{i+1} \leftarrow \frac{1}{n} \sum_{j=1}^C \phi_{i+1}^j$ 
12: end for

```

11.2 Xenon buildup and oscillations

Since the stability of the depletion scheme is to be tested by searching for unphysical xenon oscillations. The theoretical description of the ^{135}Xe oscillations is presented hereafter. ^{135}Xe has an extremely large thermal absorption cross section of approximately 2.6×10^6 barns and a high cumulative fission yield. Following the initial start up, a rapid buildup of ^{135}Xe follows. Within 30 to 40 hours an equilibrium concentration is reached at constant power. ^{135}Xe is produced directly from fission and is a product of the β^- decay chain $^{135}\text{Te} \rightarrow ^{135}\text{I} \rightarrow ^{135}\text{Xe}$. The direct fission yield is about 0.2% while the combined yield of the precursors is about 5.8 %. The ^{135}Xe concentration is governed by the following system of equations [31]

$$\frac{C(^{135}\text{I})}{dt} = \gamma^{135}\text{I} \Sigma_f \phi - \lambda^{135}\text{I} C(^{135}\text{I}) \quad (11.13)$$

$$\frac{C(^{135}\text{Xe})}{dt} = \gamma^{135}\text{Xe} \Sigma_f \phi + \lambda^{135}\text{I} C(^{135}\text{I}) - (\lambda^{135}\text{Xe} + \sigma_a^{135}\text{Xe} \phi) C(^{135}\text{Xe}).$$

The large absorption in ^{135}Xe fig. 11.1, strongly affects the spatial distribution of the neutron flux. ^{135}Xe is depleted through the reaction $^{135}\text{Xe}(n, \gamma)^{136}\text{Xe}$. ^{136}Xe has a thermal absorption cross section of only few barns, and has only limited influence on the flux distribution. In fact, ^{136}Xe has the highest probability of undergoing elastic scattering. If the flux level in some region are changed, the immediate effect is in the high flux regions and the ^{135}Xe is depleted, whereas in regions with low flux level ^{135}Xe builds up via the β^- decay of ^{135}I . The latter corresponds to removing the flux terms from (11.13). These changes reinforce the flux level shift, which subsequently leads to even larger changes. Eventually saturation is reached and the process turns over. In the regions of high flux levels, the ^{135}Xe concentration starts to increase and the power flux shift is reversed. These oscillations are eventually damped and an equilibrium ^{135}Xe concentration is reached. The equilibrium $C(^{135}\text{Xe})_{\text{eq}}$ and $C(^{135}\text{I})_{\text{eq}}$ concentrations can be obtained from (11.13)

$$C(^{135}\text{Xe})_{\text{eq}} = \Sigma_f \phi \frac{\gamma^{135}\text{I} + \gamma^{135}\text{Xe}}{\lambda^{135}\text{Xe} + \sigma_a^{135}\text{Xe} \phi}, \quad (11.14)$$

$$C(^{135}\text{I})_{\text{eq}} = \frac{\gamma^{135}\text{I} \Sigma_f \phi}{\lambda^{135}\text{I}}$$

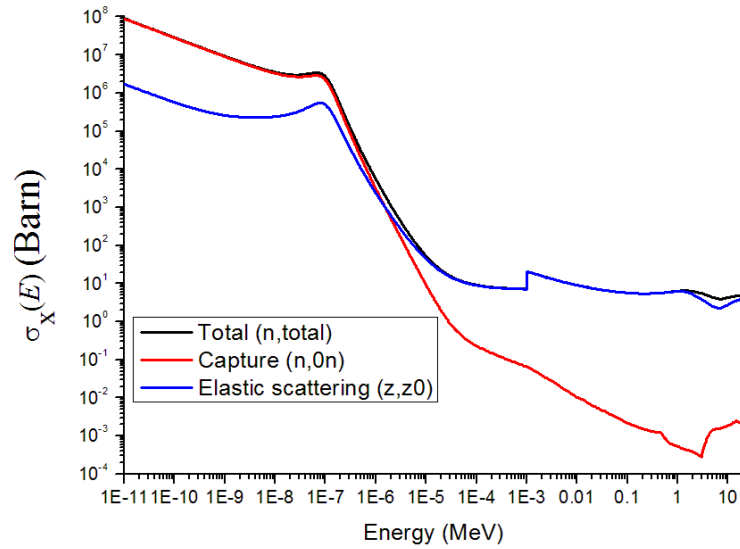


Figure 11.1: Neutron cross sections of ^{135}Xe as a function of incident neutron energy.

The coupling between the neutron flux level and the ^{135}Xe concentration is obtained with the **MCNP - KORIGEN** system, as shown in the following figures fig. 11.2. The geometry and material data are taken from [2]. The fuel is depleted with depletion steps of 0.5 MWd/t. Initially no ^{135}Xe is present in the system and the flux level is high. After the first depletion step ^{135}Xe begins to build and the flux level is depressed. Subsequently through the reaction $^{135}\text{Xe}(n, \gamma)^{136}\text{Xe}$, ^{135}Xe is depleted and the flux rises again. This cycle continues over the next steps.

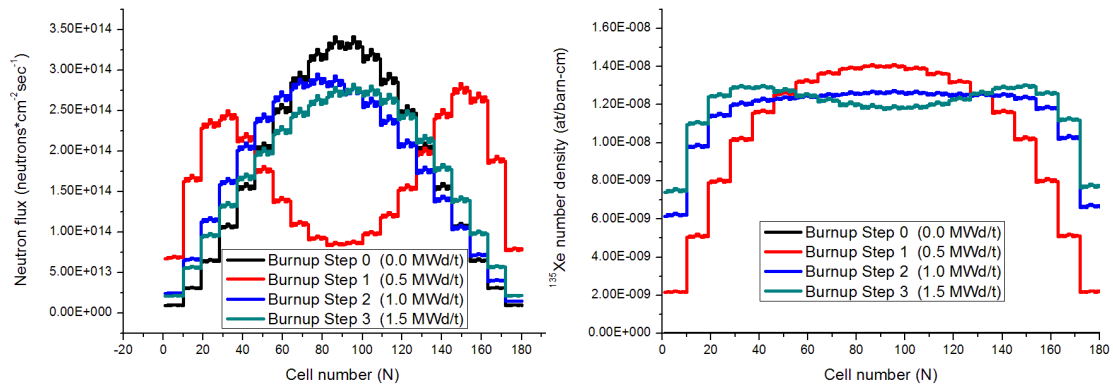


Figure 11.2: Flux distribution and ^{135}Xe concentration for different depletion steps showing the instability of the depletion calculation.

These oscillations are due to the large time step. One should take into account that the oscillations occur at a constant power and significantly after the time needed for ^{135}Xe to reach equilibrium and are purely due to the explicit coupling scheme. One might be misled into believing that these oscillations will be damped, unfortunately this is not the case. Since the time constant of the ^{135}Xe oscillations is much smaller than the depletion step size, the

concentration of xenon should be reached within the depletion step. Moreover, from (11.14) follows that the equilibrium concentration should have the symmetry of the flux distribution. Therefore, the ^{135}Xe oscillations and the unphysical flux tilts observed in Monte Carlo depletion calculations are a purely numerical effect related to the stability of the depletion scheme. To dampen these oscillations, deterministic core solvers usually impose equilibrium xenon concentration obtained by multiple neutronics solutions [94]. The equilibrium xenon concentration has been implemented in the Monte Carlo depletion systems. An optimized algorithm has been implemented in [95] the skipped cycles of the criticality calculation are divided into a number of xenon update cycles. Each xenon update cycle encompasses a number of criticality power iterations, during which the relevant reaction rates are tallied. At the end of each xenon update cycle they are used to recalculate $C(^{135}\text{Xe})_{\text{eq}}$. Another option is to use implicit depletion scheme [91].

11.3 The coupling between MCNP and KORIGEN

To perform the depletion analysis, **MCNP** was coupled to the depletion module **BURNUP** of the in house development code **KANEXT**, via the interface **MCBURN** [96]. Where **KANEXT** is the successor of **KAPROS-E** [97], [98]. The depletion module of **KANEXT** is based on the **KORIGEN** code [99],[100]. It have been validated using experimental data [98]. The new material compositions are computed after each depletion step and supplied via the internal coupling. To do this a coordinate and irradiation dependent composition vector, having components $\rho_k(\mathbf{r}, \text{BT})$ is introduced and supplied via the internal coupling

$$\Sigma_t(\mathbf{r}, E, T_{\text{input}}) = \sum_{k=1}^N \rho_k(\mathbf{r}, \text{BT}) \cdot \sum_{x=1}^R \sigma_{x,k}(\mathbf{r}, E, T_{\text{input}}), \quad (11.15)$$

where **BT** denotes the irradiation level. The internal coupling once again takes the feedback (in this case the depleted compositions) on-the-fly during the transport calculation and no artificial splitting of the geometry into sub volumes is necessary. By replacing the number densities supplied by the MCNP input $\rho_{\text{cell}} \cdot f_k$ with the number densities provided by the depletion calculation $\rho_k(\mathbf{r}, \text{BT})$ in (9.19). The thermal hydraulic feedback can be also taken into account using the internal coupling.

Since the depletion calculations need one group transmutation cross sections. These can be in principle tallied directly by the Monte Carlo code. This approach results in several times computational time increase and was not considered practical. Therefore, a multigroup approach was used for generating the one group transmutation cross sections. The 350 group library structure developed for **KANEXT** [101] was used. The neutron spectrum distribution from **MCNP** is subsequently used to collapse the 69 group library to the problem dependent one group transmutation cross sections.

Since tallies in **MCNP** are normalized per one source neutron, the neutron flux should be scaled to the user specified power level [16],[102]. Denoting the energy released per fission by Q_{fiss} , the fission reaction in a system having power output P_{tot} produces $\frac{\bar{\nu} P_{\text{tot}}}{E_{\text{fiss}}}$ neutrons. Therefore, the value of the flux normalized to the system power is given by (11.16)

$$\phi \left[\frac{\text{n}}{\text{cm}^2 - \text{s}} \right] = \frac{\bar{\nu} \times P_{\text{cell}} \left[\frac{\text{J}}{\text{s}} \right]}{1.602 \times 10^{-13} \times \left[\frac{\text{J}}{\text{MeV}} \right] \times Q_{\text{fiss}} [\text{MeV}] \times k_{\text{eff}}} \phi_n. \quad (11.16)$$

Where ϕ_n is the tallied track length flux estimate as provided by **MCNP**. Since the cell averaged fluxes are needed for the depletion calculation, the power output of the cell of interest needs to be computed. This is done by multiplying the total system power by the ratio of the fission heat deposition in the cell of interest by the total fission heat deposition in the entire geometry (11.17)

$$P_{\text{cell}} = P_{\text{tot}} \times \frac{\int_0^{\infty} \int_{V_{\text{cell}}} Q_{\text{fiss}}(\mathbf{r}, E) \Sigma_F(\mathbf{r}, E) \phi(\mathbf{r}, E) dE d\mathbf{r}}{\int_0^{\infty} \int_{V_{\text{total}}} Q_{\text{fiss}}(\mathbf{r}, E) \Sigma_F(\mathbf{r}, E) \phi(\mathbf{r}, E) dE d\mathbf{r}}. \quad (11.17)$$

In practice, both the flux and the fission heat deposition are needed. Since in all the calculations the Wieland shift was used to accelerate the fission source convergence, k_{eff} (11.17) is replaced by the shifted eigenvalue computed by the Wieland shift k_w .

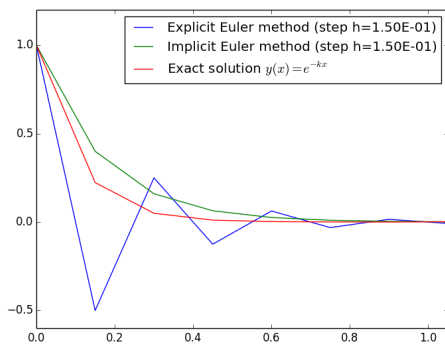
The properly normalized fluxes and the spectra for the individual depletion cells are subsequently supplied to **KORIGEN** via specially designed interface. Since all the depletion calculations are independent of each other, they are run as independent **MPI** jobs. This helps to accelerate the depletion part of the calculation. Since there is no data interchange between the depletion calculations almost a linear speedup was obtained.

11.4 Practical analysis of the stochastic implicit Euler method

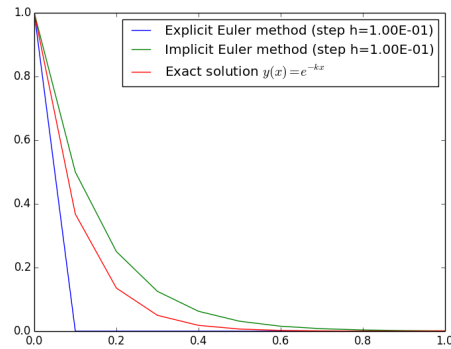
According to the general theory of the backward (implicit) Euler method, stability does not guarantee convergence to the true solution and in general deviates significantly as the step h becomes large. Consider the ordinary differential equation

$$\frac{dy}{dx} = -ky. \quad (11.18)$$

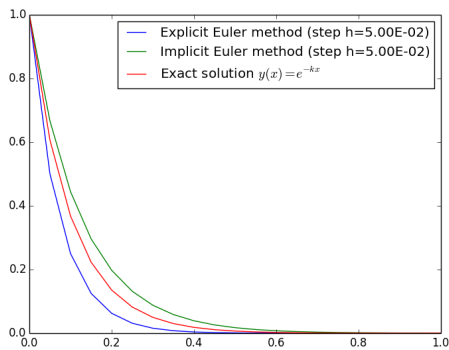
The solution of this problem for $k = 10$ is shown in below. As evident from fig. 11.3 although the stable implicit solution deviates significantly from the analytic solution for large step size.



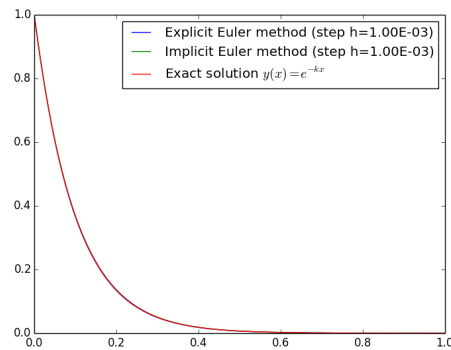
(a) Step $h = 1.50E - 1$



(b) Step $h = 1.00E - 1$



(c) Step $h = 5.00E - 2$



(d) Step $h = 1.00E - 3$

Figure 11.3: Deviation from the analytic solution as a function of step size, showing that stability does not guarantee convergence to the true solution.

For the case of the stochastic implicit Euler method with a timestep of 60 days, 14 internal iterations were run, where each **MCNP - KORIGEN** coupled run took 2.5 hours to complete. Although the solution remained stable, there were some discrepancies when it was compared with a refined explicit solution using time step of 2 hours. Suggesting that the timestep has

to be reduced. This is a significant computational penalty for practical calculations, since a typical operation cycle of a conventional PWR takes 12 months. To avoid these practical deficiencies a state of the art method proposed in [95] was implemented in the coupled system **MCNP - KORIGEN** . The method and the implementation are shown in the following section.

11.5 Monte Carlo estimation of the equilibrium ^{135}Xe concentration

In general, the rapid change of the ^{135}Xe concentration, at the beginning of the fuel cycle can be properly estimated by running very fine time steps. After the initial large reactivity drop due to the build up of xenon, the reactivity change is significantly reduced. Besides the rapid change of the ^{135}Xe and ^{135}I concentrations the overall isotope fractions remain largely in tact. Therefore, the balance equations (11.14) can be used to estimate the equilibrium concentrations. This step saves the large number of initial steps needed otherwise during the initial xenon build up stage. Consider the equilibrium ^{135}Xe values, written in detail the expectation values of the unbiased estimators for the reaction rates read

$$\begin{aligned}\langle \gamma^{135}\text{I}\Sigma_f\phi \rangle &= \frac{1}{V} \int_V \int_0^\infty \gamma^{135}\text{I}(E)\Sigma_f(\mathbf{r}, E) \phi(\mathbf{r}, E) dE d\mathbf{r} \\ \langle \gamma^{135}\text{Xe}\Sigma_f\phi \rangle &= \frac{1}{V} \int_V \int_0^\infty \gamma^{135}\text{Xe}(E)\Sigma_f(\mathbf{r}, E) \phi(\mathbf{r}, E) dE d\mathbf{r} \\ \langle \sigma_a^{135}\text{Xe}\phi \rangle &= \frac{1}{V} \int_V \int_0^\infty \sigma_a^{135}\text{Xe}(E)\phi(\mathbf{r}, E) dE d\mathbf{r}.\end{aligned}\quad (11.19)$$

The estimators (11.19) are reaction rates that can be tallied directly in **MCNP**. A special equilibrium xenon subroutine was implemented. There is an important question that has to be properly addressed. In the language of the Monte Carlo calculation the equilibrium ^{135}Xe concentrations from (11.20) involve ratio of random variables. The equilibrium concentrations are now given by the estimators

$$\begin{aligned}\langle C(^{135}\text{Xe}) \rangle_{\text{eq}} &= \frac{\langle \gamma^{135}\text{I}\Sigma_f\phi \rangle + \langle \gamma^{135}\text{Xe}\Sigma_f\phi \rangle}{\lambda^{135}\text{Xe} + \langle \sigma_a^{135}\text{Xe}\phi \rangle}, \\ \langle C(^{135}\text{I}) \rangle_{\text{eq}} &= \frac{\langle \gamma^{135}\text{I}\Sigma_f\phi \rangle}{\lambda^{135}\text{I}}\end{aligned}\quad (11.20)$$

Therefore, it is not easy to find an unbiased estimator for the equilibrium ^{135}Xe concentration. In [95] it has been shown that $\langle C(^{135}\text{Xe}) \rangle_{\text{eq}}$ and $\langle C(^{135}\text{I}) \rangle_{\text{eq}}$ are indeed unbiased estimators.

The necessary fission yield data needed in (11.19) was taken from the JEFF 3.1.1 [103]. The reaction rates were tallied using spatially written for the purpose routine and using continuous energy nuclear data. The reaction rates (11.19) are tallied directly in the code by efficiently utilizing the cross sections computed by **MCNP** and adapting the energy grid to match the

discretization used by the fission yields data of JEFF 3.1.1. One particular problem was that the flux estimates had to be scaled to the reactor power. To achieve this, formula (11.17) is used. This introduces a significant level of complication, because besides the production rates, the fission heat generation $\nu \Sigma_f \phi$ has to be tallied simultaneously. This was done by estimating an average number of neutrons released per fission by the subroutine used for tallying the ^{135}Xe production rates. To normalize the flux the number of neutrons produced per fission is also needed. In the normal case, its value is computed at the end of each **MCNP** run. At the stage when the equilibrium xenon is computed, the number of fission neutrons is not directly available. To compute ν , the total weight produced from the source $w_{t,s}$ and lost to fission $w_{t,f}$ was accumulated during the transport calculation. Using this values the averaged number of neutrons produced per fission can be computed using (11.21). Where $\langle k \rangle$ is the averaged eigenvalue from all the completed criticality cycles.

$$\nu = \langle k \rangle \frac{w_{t,s}}{w_{t,f}}. \quad (11.21)$$

Although, the number of source neutrons per cycle are chosen to provide a representative sample of the global fission source, it is often not sufficient to produce well converged results for local reaction rates. These large uncertainties can have a significant impact on the estimators (11.20) and might lead to erroneous and biased results. Therefore, the equilibrium concentrations are estimated over the batches of source update cycles. The ^{135}Xe concentrations are estimated during the inactive cycles of the criticality calculation. Using this methodology, the I initial criticality cycles are split into M batches containing containing $P = \frac{I}{M}$ cycles of N histories each. For each of those batches the mean was estimated using

$$x_j = \frac{1}{PN} \sum_{j=1}^M x_j. \quad (11.22)$$

After each batch, the ^{135}Xe concentration is updated. The number of histories according to the nominal source size as specified by the **MCNP** input is used to normalize the reaction rate estimators per one starting source neutron. As with the fission source iterations, some allowance must be done to disregard early estimates of (11.20). At the beginning of the Monte Carlo Power iteration, the fission source is far from its stationary value and tallying produces biased results. When running standard criticality calculations, no tallying is done at that stage. This is unfortunately impossible in the case of the equilibrium ^{135}Xe and ^{135}I calculation. In this case the reaction rates that are needed (11.19) are part of the feedback calculation itself. Therefore, to avoid contaminating the final equilibrium concentrations with biased results, after an initial number of skipped batches (usually 5) the estimators are reset after each update. Following this initial stage, the tallies are no longer reset, allowing the estimators to accumulate over a few batches. To obtain a reliable estimate of the ^{135}Xe concentration, 30 concentration updates were done.

Since the equilibrium concentration of the neutron poisons are calculated as the derivatives of the flux at the equilibrium values, (11.20) no oscillations are possible. Explicit calculations

showed that the equilibrium concentrations are reached after 30 hours from the beginning of the cycle. Therefore, the other isotope concentrations change only by a small amount and in principle the equilibrium ^{135}Xe calculation can be done with the concentrations of the fuel isotopes from the beginning of the cycle. However, the best agreement with the explicit fine step calculation is obtained using the concentrations at the time ^{135}Xe reaches equilibrium [95].

11.6 Numerical results

As discussed in the introductory chapter, rapid buildup of ^{135}Xe follows the reactor startup. This is illustrated in fig. 11.4. The calculation represents a pin cell depleted at constant power density of $0.2418 \frac{\text{kW}}{\text{g}}$. For the depletion calculation the 350 energy groups library of **KANEXT** was used. To verify the results the **SERPENT** continuous energy Monte Carlo depletion code was used [20]. As evident from the plots very good agreement was found. For the Monte Carlo transport simulation Jeff 3.1.1 data was used. This explains the small difference of only 40pcm for the fresh fuel calculation. Therefore, the difference of 200pcm in the eigenvalue at the end of the 5 day irradiation period is due to the different data used as input for the Bateman equations.

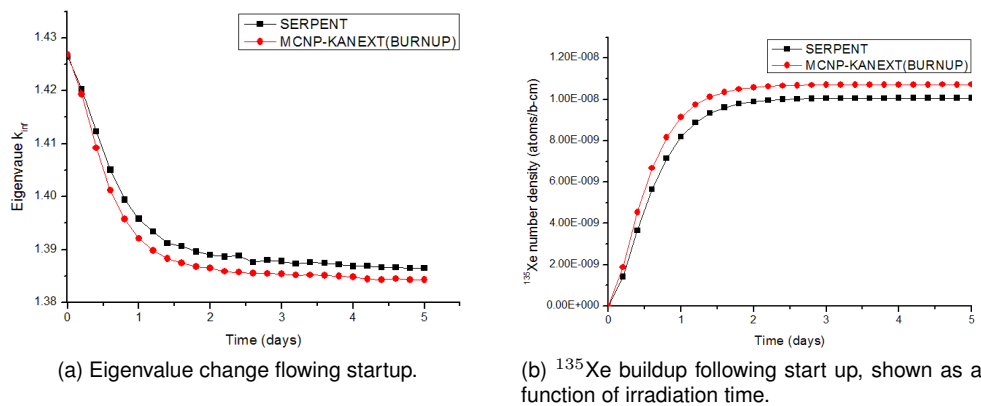


Figure 11.4: Pin cell depletion calculation showing the evolution of the eigenvalue and the ^{135}Xe concentration as a function of irradiation time as computed by

A corresponding three dimensional calculation illustrating the same effect is shown in figures fig. 11.5 and fig. 11.6.

The results are compared to a deterministic solution obtained by **DANTSYS** [104]. In this case the deterministic code replaces **MCNP** and computes the neutron flux distribution. The transport model used S_8 angular quadrature with P_1 scattering expansion and 69 energy groups. The deterministic system was used to study the general properties of the system. Since deterministic transport runs considerably faster than the corresponding Monte Carlo calculation and no stochastic variation of the fission heat deposition are present, the system was used as a 'low cost' comparison tool. As expected, the results are not completely identical. Since both codes use the same depletion module, the difference is due to the approximations used by the deterministic system. Moreover, the difference is observed also for the first depletion step where no depletion feedback is present. Both the calculations predict similar evolution of the eigenvalue and the ^{135}Xe buildup. As in the case of the pin cell calculation, following the initial accumulation of fission poison and drop in reactivity, the ^{135}Xe buildup reaches saturation. Due to the stochastic noise, the calculation become unstable after 20 coupled runs. This can be seen by observing the ^{135}Xe behavior during the last iterations shown in fig. 11.6.

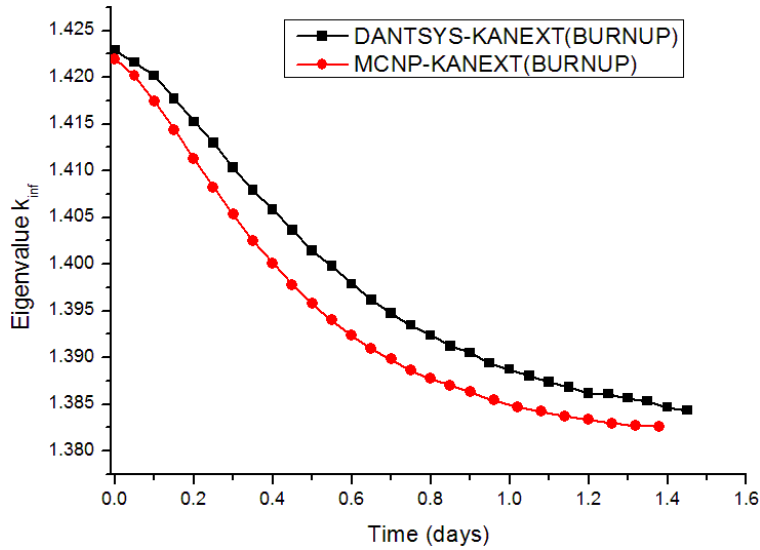


Figure 11.5: Eigenvalue change flowing startup, shown as a function of irradiation time.

Based on multiple trial runs, the stochastic noise and the bias due to the wrong estimated neutron source were determined as additional causes for the ^{135}Xe - flux oscillations. To reduce the stochastic noise and improve the convergence of the fission source, the Wielandt acceleration method presented in chapter 4 was used. The time step is also chosen small (0.05 days), so that the instability due to the explicit coupling scheme is prohibited. This made the calculation computationally expensive. To reduce the dominance ratio of the system, the spectral shift of the transport operator was kept small. According to (5.14) this large number of additional neutrons were produced within each cycle. To speedup the calculation, an analog computation with doubled number of histories was run. This strategy produced numerical oscillation within few cycles and was not proceeded further. Besides the extra precocious measures, the explicit calculation started oscillating after 20 depletion steps. This oscillation was purely numerical in nature, and was caused by the asymmetries of the flux distribution, caused by the Monte Carlo stochastic effects.

To test the equilibrium xenon concentration two calculations were run. The first was the pin cell calculation shown in fig. 11.4. Since no spatial oscillations are possible, the pin cell calculation was used as a validation tool to study the consistency of the new methodology. Using the simplified numerical model all the features of the new method can be tested, without interferences due to numerical effects. In the case of the pin cell no Wielandt acceleration was necessary. Equilibrium was assumed to occur after 5 days of irradiation, this assumption is confirmed further by fig. 11.4. It should be noted that after 5 days of irradiation, the isotopic content changes. To take this into account, the equilibrium ^{135}Xe concentration was run with the depletion compositions obtained after 5 days of irradiation. Otherwise, inconsistent results for the eigenvalue would have been produced, since the Monte Carlo code would have imposed equilibrium ^{135}Xe concentration using fresh fuel loading. In this case the eigenvalue would have been higher when compared to the explicit calculation [95].

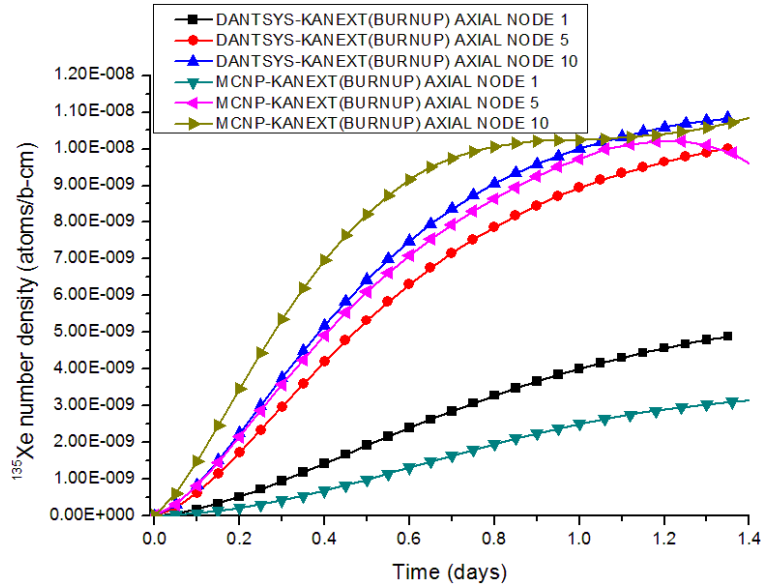


Figure 11.6: ^{135}Xe buildup following start up, shown as a function of irradiation time. Shown are deterministic and Monte Carlo solutions.

Table 11.1: Summary of the eigenvalues and equilibrium ^{135}Xe concentrations for a pin cell calculation computed by **SERPENT** and **MCNP**. The explicit solutions are used to validate the equilibrium ^{135}Xe computation.

Calculation	Eigenvalue k_{eff}	^{135}Xe (at/b-cm)	runs	time for one run (min)
Explicit SERPENT	1.38654 (14)	1.00595E-08	25	20
Explicit MCNP	1.38431 (12)	1.07115E-08	25	30
MC ^{135}Xe estimate	1.38396 (14)	1.07543E-08	1	33

As evident from table 11.1 the equilibrium values for the multiplication factor are about 250 pcm apart from each other, when comparing the **SERPENT** and **MCNP** calculations. The explicit calculation by **MCBURN** and the calculation, where the ^{135}Xe production was tallied by **MCNP**, show precise agreement. This agreement is kept also for the energy spectrum fig. 11.7. The large differences in the high energy region are due to poor tally statistics. The low number of neutrons having energies within this domain resulted in insufficient sampling and high statistical uncertainty. In this energy region, the ^{135}Xe effect plays no role and the uncertainties are numerical in nature. To indicate the underlying variance, the associated uncertainties of the flux estimates were propagated and plotted in fig. 11.7.

The eigenvalue predicted by the direct Monte Carlo tallying of the equilibrium ^{135}Xe concentration is computed using continuous energy fluxes, taking into account the precise geometry, whereas in the case of the explicit calculation, 350 energy group fluxes were used. Moreover, the nuclear data for the fission yields, fission cross sections and the decay constants from distinct libraries were used. In the case of the explicit calculation the data from the **KANEXT** libraries was used. Whereas in the case of the Monte Carlo ^{135}Xe estimate, JEFF 3.1.1 data was used. The main difference between the fission yield data used by the depletion module

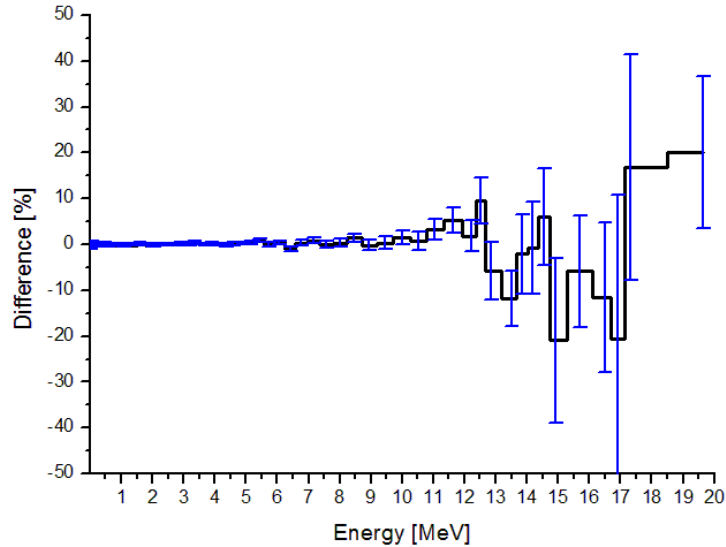


Figure 11.7: Neutron spectrum difference in the fuel pellet between the explicit depletion calculation and the new method as a function of neutron energy. The corresponding statistical uncertainties from the Monte Carlo calculation are propagated and shown together with the computed difference.

of **KANEXT** and **MCNP** is the fact that in the latter case, the fission yields are selected based on the neutron energy and no spectral weighting is used. Via the input of **KANEXT** is possible to define JEFF-based fission yields data as input. The spectral weighting Ansatz is used in all the cases. This was essential for making the depletion part of the calculation coherent. In spite of the different nuclear data, the explicit calculation and the Monte Carlo method for tallying the equilibrium ^{135}Xe concentration produced very close results, verifying the implementation. The differences observed are small for both the eigenvalue and the neutron spectrum. In general, it can be concluded that the Monte Carlo equilibrium ^{135}Xe concentration produces reasonable results. Meaning, that the method for normalizing the flux and the strategy for computing the reaction rates (11.19) were consistently implemented. This difference between **MCBURN** and **SERPENT** is also to be expected, since the codes use different methods for solving the Bateman equations and different nuclear data sets as input. Clarifying the differences due to the nuclear data goes beyond the scope of this thesis. In [95] identical set of data was used, and perfect agreement between the Monte Carlo equilibrium ^{135}Xe calculation and reference explicit calculation was found. This result was confirmed in this work when the same depletion code was used for solving the depletion equations.

Clearly the new method outperforms the explicit calculation, since the equilibrium concentrations were obtained within a single run, whereas in the case of the explicit calculation 25 runs were needed. This together with the fact that the oscillations are damped, since equilibrium ^{135}Xe concentration is always imposed, motivates the decision to implement the new methodology.

Conclusions and outlook

The primary goal of the research and development presented in this thesis is to enable Monte Carlo simulation of large scale reactor geometries, using detailed physics models. Accomplishing this goal involved numerous developments and implementations in the general purpose code **MCNP**, which are unique and original contributions. Questions related to the physics of neutron interactions, improving the efficiency of the Monte Carlo method and optimizing the computational scheme were addressed.

The first step in achieving the objective was to introduce varying material field properties, by both taking into account the thermal hydraulic feedback and by introducing depletion capability. A novel method of dynamic material definition, capable of taking into account detailed three dimensional temperature, density and isotopic compositions was introduced. Since the thermal hydraulic feedback is introduced via the thermal effects experienced by the nuclear cross sections, methods capable of correcting for temperature dependence of the nuclear data were implemented. Special attention was dedicated to the temperature dependence of the thermal scattering nuclear data. This is especially important since it governs the slowing down of the neutrons in the moderator. The new methodologies were validated against exact processed reference nuclear data.

Since large scale geometries were considered, significant improvements of the Monte Carlo eigenvalue calculation were needed. It was discovered that due to ill convergence of the power iteration the tallies had significant bias. This is most notable when the symmetry of the tallies was examined. To overcome this problem the Wielandt acceleration method was implemented. It was observed that in the limit where the shifted eigenvalue approaches the true eigenvalue of the system, significant improvement of the source entropy convergence can be achieved. The effect of the method on reducing the dominance ratio of the system was analysed by investigating the higher mode eigenvalues. For the analysis the fission matrix technique was implemented in **MCNP**. Significant developments were needed to accumulate the large sparse matrices produced by the fission matrix technique and to estimate their eigenvalues. The efficiency of the modified power iteration was studied using detailed two

and three dimensional models. The newly implemented Wielandt shift method was validated by numerical comparison.

The fission matrix technique implemented in **MCNP** has enabled for the first time to compute higher mode eigenvalues of the neutron transport operator at pin by pin resolution and taking into account the thermal hydraulic conditions in the core.

Since tallying the fission heat deposition using detailed spatial mesh was needed, novel variance reduction techniques were introduced. It was proven, that the global variance reduction technique is computationally expensive, and can not be used for practical calculations. Therefore, the state of the art uniform fission site method was implemented in **MCNP**. The results from both the variance reduction schemes were compared using a generalized definition of the figure of merit. It was proven that the uniform fission site method is capable of delivering results close to the global variance reduction scheme, at significantly lower computational cost. Since the global variance reduction scheme is standard available in **MCNP**, it was used to validate the newly implemented variance reduction scheme. In addition, a computational algorithm for efficiently storing the accumulated Monte Carlo estimators was developed.

Following the integration of the new developments, the stability of the coupled system **MCNP** - **SUBCHANFLOW** was investigated. To improve the convergence, the stochastic approximation technique was implemented. It represent a stochastic numerical scheme capable of finding fixed points by observing random values having unknown an underlying distribution. It was shown that this scheme is capable of ensuring uniform convergence within limited number of coupled iterations. Since the solution following each iteration of the coupled scheme shown to be a combination of all the previous runs, the scheme not only accelerates the convergence but improves the uncertainty of the Monte Carlo estimates for the fission heat deposition.

The coupled scheme was applied to the PWR UOX-MOX benchmark. This international benchmark exercise was used to validate the new methodologies. Since the coupled calculation combines all the developments related to improving the statistics, accelerating the criticality calculation, the fission heat deposition tallying and the temperature dependence of the nuclear data, it serves as an integral test for all the developments done in this thesis. Using the advanced code modifications it was possible for the first time to run a coupled Monte Carlo - thermal hydraulics problem at pin-by-pin resolution.

The internal coupling methodology was further extended to take into account fuel depletion. For the purpose, the coupling between **MCNP** and the in-house code **KORIGEN** was developed. Monte Carlo estimates of the neutron spectrum and flux level are used to prepare the reaction rates required as input for the fuel depletion equations. The new internal coupling greatly simplified the information exchange between the two codes. To overcome the instability of the Monte Carlo depletion calculation, a state of the art method of imposing equilibrium xenon concentrations was implemented. This method, uses the inactive cycles of the criticality calculation to compute the equilibrium xenon distribution for the given power and fuel irradiation level. Since, the xenon concretion is obtained as a function of the neutron flux, no

oscillations are possible. Moreover, the equilibrium concentrations are estimated within a single Monte Carlo run, which is a serious advantage in terms of the computing time needed for ruining the calculation. The consistency of the newly implemented depletion capability was verified by comparing it to deterministic and Monte Carlo reference solutions. For the first time depletion calculations were done using the improved power iteration technique, which shifts the eigenvalue spectrum via the Wielandt acceleration technique. This strategy helped to reduce the bias of the Monte Carlo flux estimate.

Additional topics remain to be further investigated in the future. For instance, the parallel scalability of the Monte Carlo criticality calculation can be further improved. In particular, the collection of the fission source by the Master process. It is also possible to eliminate the inter process communication completely by running independent Monte Carlo jobs. This strategy has already been proven effective by some of the currently available Monte Carlo codes.

The newly implemented methodology for computing the equilibrium xenon concentrations paves the way to stable large scale deterministic calculations. Due to time constraints, the accuracy of the new methodology is verified by code to code comparison. Therefore, it should be tested on a large scale three dimensional problem, for which the existing depletion systems are known to be unstable.

In principle, the coupled system as such, can only simulate steady state problems and lacks the ability to treat transient scenarios needed for reactor safety analysis. In the recent years there has been a significant effort towards the development of time dependent Monte Carlo reactor analysis codes. Therefore, the introduction of transient capability is currently under development. This computational tool will be able to run spacial kinetics problems, taking into account all the advantages of the Monte Carlo codes, breach the gap left over by deterministic tools.

An open question is the validation using experimental data. In this work the main focus fell on the development and implementation of new numerical methodologies aimed at solving the challenges of the high-fidelity large-scale reactor core simulations. The experimental validation was left as part of a future effort, since it goes beyond the scope of this thesis. Although the coupled system was verified using the PWR UOX-MOX benchmark, the comparison with measured data is important. Since the code numerical modifications were tested and proven correct by code to code comparison, experimental validation would mainly test the ability of the general purpose code **MCNP** and the newly implemented thermal hydraulics and depletion capabilities to capture the physics of large scale reactor core computations and test the validity of the physics models. Among others, this validation analysis will test not only the computational method but also the accuracy of the nuclear data and the thermal hydraulic models. Such comparisons should be done for both hot full power and cold zero power, to test the precise effect of the thermal hydraulic feedback on the neutron transport calculation. One particular example is the **BEAVRS** benchmark, recently published by **MIT** [105]. It would be also interesting to test the coupled system on a problem for which deterministic codes are known to experience problems, for instance, a Generation 4 design.

List of symbols

$\hat{\Omega}$	unit vector in the direction of neutron motion
\mathbf{r}	radius vector
\mathbf{n}	outward surface normal vector
∇	gradient differential operator
$\nabla \cdot$	divergence differential operator
$\langle \mathbf{a} \mathbf{b} \rangle$	scalar product of two vectors
$ \mathbf{a} $	norm of vector \mathbf{a}
\mathbf{I}	identity matrix
t	time variable
T	temperature
k	Boltzmann constant
E	neutron energy
A	isotope mass number
$\delta()$	Dirac delta distribution

\mathbf{v}	neutron vector velocity
$v = \mathbf{v} $	modulus of the neutron velocity
$\Psi(\mathbf{r}, E, \hat{\Omega})$	angular neutron flux
$S(\mathbf{r}, E, \hat{\Omega})$	neutron source
$d\mathbf{r}d\hat{\Omega}dE$	volume element in phase space
$\mathbf{P} = (\mathbf{r}, \hat{\Omega}, dE)$	coordinate point in phase space
$\chi(\mathbf{r}, \hat{\Omega}, E) d\mathbf{r}d\hat{\Omega}dE$	number of neutrons starting a flight path
$\xi(\mathbf{r}, \hat{\Omega}, E) d\mathbf{r}d\hat{\Omega}dE$	number of neutron entering a collision
$C(\hat{\Omega} \cdot \hat{\Omega}', E' \rightarrow E \mathbf{r})$	collision kernel
$T(\mathbf{r}' \rightarrow \mathbf{r} \hat{\Omega}, E)$	transport kernel
Σ_f	macroscopic fission cross section
σ_f	microscopic fission cross section
Σ_t	macroscopic total cross section
σ_t	microscopic total cross section
Σ_s	macroscopic scattering cross section
σ_s	microscopic scattering cross section
k_{eff}^C	collision eigenvalue estimate
k_{eff}^T	track length eigenvalue estimate
k_{eff}^A	absorption eigenvalue estimate
w_i	particle weight

\mathbf{E}	$(E, \hat{\Omega})$
$\xi(E)$	fission spectrum
H_{src}	Shannon entropy of the fission source
$Y_{l,m}$	Spherical harmonics
μ	directional cosine
$P_l(\mu)$	Legendre polynomials
$\psi(x, \mu)$	one-dimensional neutron flux
ϕ_g	group averaged neutron flux
$\Sigma_{f,g}$	group averaged fission cross section
$\Sigma_{s,gg'}$	group to group scattering cross section
Σ_g	group averaged total cross section
ξ_g	group emission spectrum
$\rho(\zeta)$	bound hydrogen oscillation spectrum
$\hat{\mathbf{H}}(\mathbf{r}' \rightarrow \mathbf{r})$	fission matrix
$\mathbf{H}_{n,m}$	discretised fission matrix
$\gamma^{135\text{I}}$	yield of ^{135}I
$\gamma^{135\text{Xe}}$	yield of ^{135}Xe
$\sigma_a^{135\text{Xe}}$	absorption cross section ^{135}Xe
$\lambda^{135\text{I}}$	decay constant of ^{135}I
$\lambda^{135\text{Xe}}$	decay constant of ^{135}Xe
$C(^{135}\text{I})$	concentration of ^{135}I

$C(^{135}\text{Xe})$	concentration of ^{135}Xe
$\langle \gamma^{135}\text{I} \Sigma_f \phi \rangle$	expectation value of the unbiased estimator for ^{135}I production
$\langle \gamma^{135}\text{Xe} \Sigma_f \phi \rangle$	expectation value of the unbiased estimator for ^{135}Xe production
$\langle \sigma_a^{135}\text{Xe} \phi \rangle$	expectation value of the unbiased estimator for absorption by ^{135}Xe

List of Figures

2.1	Pressurized water reactor core. source: J.R. Lamarsh and A. J. Baratta "Introduction to nuclear engineering".	29
3.1	Evolution of the Shannon entropy H_{src} vs. criticality cycle.	37
3.2	Evolution of the eigenvalue k_{eff} vs. criticality cycle.	38
4.1	Cross sections of ${}_{92}^{238}U$ as a function of the incident neutron energy.	48
4.2	Capture cross section for U_{92}^{238} evaluated at $600K$ and $1800K$ showing the effect of Doppler broadening.	49
4.3	Geometry of the fuel assembly used for the numerical tests. The color code of the figure indicates the different materials. For the calculation identical coolant was used inside the guide tube and in between the fuel pins.	50
4.4	Inelastic scattering cross sections for bound hydrogen as a function of the incident neutron energy.	56
4.5	Oscillation spectrum $\rho(\zeta)$ of the target nucleus as a function of the oscillator energy.	57
4.6	Material composition illustrating the pseudo material mixing for thermal scattering data.	58
4.7	Linear logarithmic plot of the neutron flux as a function of energy evaluated for two moderator temperatures: $573.6K$ and $623.6K$	59
4.8	Difference in the neutron flux spectrum evaluated using interpolated data and exact evaluated data for the case of coolant temperature of $573.6 K$	60
4.9	Difference in the neutron flux spectrum evaluated using interpolated data and exact evaluated data for the case of coolant temperature of $623.6 K$	61

4.10	Difference between the neutron moderator spectrum evaluated using the pseudo material mixing methodology and the direct evaluated thermal scattering data.	62
4.11	Difference between the neutron moderator spectrum evaluated using the on the fly thermal scattering interpolation and the direct evaluated thermal scattering data. The reference data is evaluated at 573.6K and 623.6K.	63
5.1	Quarter PWR core geometry loaded with MOX and UOX fuel assemblies, denoted by (MOX FA) and (UOX FA). The computational geometry is surrounded by water volume serving the role of neutron reflector.	69
5.2	H_{src} vs. criticality cycle for different values of k_e and H_{src} vs. criticality cycle for the cases $k_e = \infty$ and $k_e = 1.16$ illustrating the reduction of the cycles needed for converging the source entropy.	69
5.3	Two dimensional plot of the relative error of the fission heat deposition distribution in % for the case $k_e = \infty$. Each point represents the value of the relative error for a single fuel pin.	70
5.4	Two dimensional plot of the relative error of the fission heat deposition distribution in % for the case $k_e = 1.8$. Each point represents the value of the relative error for a single fuel pin.	72
5.5	Two dimensional plot of the relative error of the fission heat deposition distribution in % for the case $k_e = 1.16$. Each point represents the value of the relative error for a single fuel pin.	72
6.1	Z-ordering in \mathbb{R}^2 for a 8×8 lattice using the space filling technique according to Morton.	80
6.2	The strategy of splitting the arrays into chunks corresponding to the individual threads by offsetting the cell location index \mathbf{l}	81
7.1	Plot of the fission matrix $\log_{10} \mathbf{H}_{i,j}$. The abscissa and the ordinate of the plot represent the matrix indices i and j	85
7.2	The eigenvectors corresponding to eigenvalues k_0 to k_7	91
7.3	The eigenvectors corresponding to eigenvalues k_8 to k_{15}	92
7.4	Plot of the fission matrix $\log_{10} \mathbf{H}_{i,j}$. The abscissa and the ordinate of the plot represent the matrix indices i and j	94
8.1	Principle of the Weight Windows technique.	99
8.2	Two dimensional plot of the relative error of the fission heat deposition distribution in %. Each point represents the value of the relative error for a single fuel pin.	103

8.3	Two dimensional plot of the relative error of the fission heat deposition distribution in %. Each point represents the value of the relative error for a single fuel pin.	103
8.4	Two dimensional plot of the relative error of the fission heat deposition distribution in %. Each point represents the value of the relative error for a single fuel pin.	104
9.1	The internal coupling scheme	113
10.1	Neutron spectrum in the twice burn MOX assembly D4 and the fresh UOX assembly E4 plotted as function of energy.	117
10.2	The PWR MOX-UOX core loading pattern as given by [63].	117
10.3	Relative difference of the pin power distribution of the diagonal assemblies between DeCART and MCNP given in %.	120
10.4	Relative difference of the pin power distribution of the diagonal assemblies between DORT and MCNP given in %.	121
10.5	Convergence ϵ as a function of the coupled iteration N and two dimensional pin power distribution.	123
10.6	Three dimensional coolant density and fuel temperature distributions, having single fuel pin resolution, computed by the coupled system MCNP - SUB-CHANFLOW	124
10.7	Core averaged fuel Doppler temperature and power distributions plotted as functions of the core height.	124
10.8	Relative difference of the pin power distribution between SKETCH-INS 2G and MCNP given in %.	130
10.9	Relative difference of the pin power distribution between PARCS 2G and MCNP given in %.	131
11.1	Neutron cross sections of ^{135}Xe as a function of incident neutron energy.	138
11.2	Flux distribution and ^{135}Xe concentration for different depletion steps showing the instability of the depletion calculation.	138
11.3	Deviation from the analytic solution as a function of step size, showing that stability does not guarantee convergence to the true solution.	142
11.4	Pin cell depletion calculation showing the evolution of the eigenvalue and the ^{135}Xe concentration as a function of irradiation time as computed by	147
11.5	Eigenvalue change following startup, shown as a function of irradiation time.	148
11.6	^{135}Xe buildup following start up, shown as a function of irradiation time. Shown are deterministic and Monte Carlo solutions.	149

-
- 11.7 Neutron spectrum difference in the fuel pellet between the explicit depletion calculation and the new method as a function of neutron energy. The corresponding statistical uncertainties from the Monte Carlo calculation are propagated and shown together with the computed difference. 150

List of Tables

4.1	List of the geometry and material composition data for the fuel assembly geometry specified in fig. 4.3.	51
4.2	Comparison of the k_{∞} values computed using linear and square root (sqrt) pseudo material mixing against the exact broadened reference data for the UOX case.	51
4.3	Comparison of the k_{∞} values computed using linear and square root (sqrt) pseudo material mixing against the exact broadened reference data for the MOX case.	52
5.1	Performance of Wielandt acceleration method for different k_e showing the reduction of cycles needed to converge the fission source distribution.	68
5.2	Table showing the suppression of the unphysical tally asymmetry for the ten axial planes of the problem shown as a function of the shift eigenvalue k_e . Shown are the maximum tilt $\ \mathbf{T}_k\ $ its corresponding mean value $\mu(T_{i,j}^k)$ and standard deviation $\sigma(T_{i,j}^k)$ estimated over all pin cells having positions i and j for a certain axial level k	71
5.3	Maximal relative difference between analog and calculation and the Wielandt shift method.	74
6.1	Description of the indexes used to describe the location of a particular cell in the core geometry.	79
6.2	Z-ordering in three dimensional space. The integers representing the lattice indices are converted to binary form and used to determine the z-order by interleaving the binary representations.	79

6.3	Comparison of the z-ordering and the usual unrolled 3D array ordering, showing that the array storage is much more compact and is less likely to cause cache misses. I, J and K denote the coordinates used to describe the position in \mathbb{R}^3 .	80
6.4	Numerical performance of the improved tallying methodology applied to a quarter PWR core. The same geometry as the one used for testing the Wielandt method is used.	82
7.1	The coordinate storage format for sparse arrays. Each nonzero matrix element $a_{i,j}$ of the matrix (7.10) is stored by recording its value and its corresponding row i and column j indices.	86
7.2	Higher mode eigenvalues of the fission matrix as a function of the mesh resolution and the number of histories used for the simulation.	90
7.3	Fission matrix eigenvalues with shift (two dimensional case)	95
7.4	Fission matrix eigenvalues with shift (three dimensional case)	96
8.1	Performance summary of the variance reduction techniques. 750 active cycles with 1×10^6 histories per cycle.	105
8.2	Performance summary of the variance reduction techniques. 750 active cycles with 1×10^6 histories per cycle were run together with an additional run using 1.3×10^6 particles per cycle.	105
8.3	Difference between the Wielandt shift method ($k_e = 1.16$) the GVR and the UFS schemes.	106
10.1	Eigenvalue estimates	118
10.2	Assembly power relative difference between DeCART and MCNP given in %.	118
10.3	Assembly power relative difference between DORT and MCNP given in %.	119
10.4	Assembly power relative difference between SKETCH-INS 2G and MCNP given in %.	125
10.5	Assembly power relative difference between PARCS 2G and MCNP given in %.	125
10.6	Assembly power relative difference between PARCS 8G and MCNP given in %.	126
10.7	Assembly averaged fuel temperature relative difference between SKETCH-INS 2G and MCNP given in %.	127
10.8	Assembly average fuel temperature relative difference between PARCS 2G and MCNP given in %.	127
10.9	Assembly averaged fuel temperature relative difference between PARCS 8G and MCNP given in %.	127

10.10	Assembly power relative difference between SKETCH-INS 2G and PARCS 8G given in %.	128
10.11	Assembly averaged fuel temperature relative difference between SKETCH-INS 2G and PARCS 8G given in %.	128
11.1	Summary of the eigenvalues and equilibrium ^{135}Xe concentrations for a pin cell calculation computed by SERPENT and MCNP . The explicit solutions are used to validate the equilibrium ^{135}Xe computation.	149

Bibliography

- [1] A. Ivanov, V. Sanchez, R. Stieglitz, and K. Ivanov, "Internal multi-scale multi-physics coupled system for high fidelity simulation of light water reactors," *Annals of Nuclear Energy*, **66**, pp. 104–112 (2013).
- [2] A. Ivanov, V. Sanchez, R. Stieglitz, and K. Ivanov, "High fidelity simulation of conventional and innovative LWR with the coupled Monte-Carlo thermal-hydraulic system MCNP-SUBCHANFLOW," *Nuclear Engineering and Design*, **262**, pp. 264–275 (2013).
- [3] P. S. Brantley and E. Larsen, "The Simplified P3 Approximation," *Nuclear Science and Engineering*, **134**, pp. 1–12 (2000).
- [4] Y. A. Chao and A. Yamamoto, "The Explicit Representation for the Angular Flux Solution in the Simplified P_n (SP_n) Theory," *Proceedings of the PHYSOR 2012 conference*, Knoxville, Tennessee, April, 2012.
- [5] C. Beckert and U. Grundmann, "Entwicklung einer Transportnaeherung fuer das reaktordynamische Rechenprogramm DYN3D," Research Center Dresden-Rossendorf (2008).
- [6] T. Endo and M. Tatsumi, "Study on kinetic transport solvers for pin-by-pin core calculation," *Proceedings of PHYSOR 2008 conference*, 2008.
- [7] D. P. Weber et al., "High-Fidelity Light Water Reactor Analysis with the Numerical Nuclear Reactor," *Nuclear Science and Engineering*, **155**, 3, pp. 395–408 (2007).
- [8] P. K. Romano and B. Forget, "Parallel Fission Bank Algorithms in Monte Carlo Criticality Calculations," *Nuclear Science and Engineering*, **170**, pp. 125–123 (2012).
- [9] J. Hoogenboom, A. Ivanov, and V. Sanchez, "Maximum Efficiency in Massively Parallel Execution of Monte Carlo Criticality Calculations," *Proceedings ANS MC2015 - Joint International Conference on Mathematics and Computation (M&C), Supercomputing in Nuclear Applications (SNA) and the Monte Carlo (MC) Method* (2015).

- [10] D. J. Kelly, T. M. Sutton, and S. C. Wilson, "MC21 Analysis of the Nuclear Energy Agency Monte Carlo Performance Benchmark Problem," *Proceedings PHYSOR-2012, Knoxville, Tennessee, USA*, **CD ROM** (2012).
- [11] T. M. Sutton, "The MC21 Monte Carlo Transport Code," *Proceeding Joint Int. Topl. Mtg. Mathematics and Computation and Supercomputing in Nuclear Applications (M&C SNA)*, Monterey, California, United States (2007).
- [12] W. Bernnat, "Coupled Monte Carlo Neutronics and Thermal Hydraulics for Power Reactors," *Proc. Int. Conf. PHYSOR 2012, Knoxville, Tennessee, USA*, **CD-ROM** (2012).
- [13] D. Kotlyar, Y. Shaposhnik, E. Fridman, and E. Shwageraus, "Coupled neutronic thermo-hydraulic analysis of full PWR core with Monte-Carlo based BGCore system," *Nuclear Science and Engineering*, **241**, pp. 3777–3786 (2009).
- [14] F. P. Espel, M. Avramova, K. Ivanov, and S. Misu, *High Accuracy Modeling for Advance Nuclear Reactor Core Designs using Monte Carlo Based Coupled Calculations*, Invited paper for MC (2009).
- [15] B. R. Hanna, D. F. Gill, and D. P. Griesheimer, "Reactivity Effects of Spatial Homogenization of Thermal Feedback Regions in Monte Carlo Reactor Calculations," *Nuclear Technology*, **183**, 3, pp. 367–378 (2013).
- [16] D. Poston and H. Trelle, *Users Manual for MonteBurns*, Version 1.0. 2nd ed. (1999).
- [17] M. L. Fensin, J. S. Hendricks, and S. Anghaie, "The enhancements and testing for the MCNPX 2.6.0 depletion capability," *Nuclear Technology*, **170**, pp. 68–79 (2010).
- [18] R. L. Moore, B. G. Schnitzler, C. Wemple, R. Babcock, and D. Wessol, *MOCUP: MCNP-ORIGEN 2 Coupled Utility Program. Tech. Rep. INEL-95 0523*, Idaho National Engineering Laboratory. (1995).
- [19] W. Haeck and B. Verboomen, *ALEPH 1.1.2 A Monte Carlo Burn-up Code*, ISSN 1379 2407, Belgian Nuclear Research Centre, Mol, Belgium (2006).
- [20] J. Leppänen, *Serpent a Continuous energy Monte Carlo Reactor Physics Burnup Calculation Code*, http://montecarlo.vtt.fi/download/Serpent_manual.pdf (2013).
- [21] N. 1840, "SERPENT a Continuousenergy Monte Carlo Reactor Physics Burnup Calculation Code," 2010.
- [22] J. Cetnar, W. Gudowski, and J. Wallenius, *User Manual for Monte-Carlo Continuous Energy Burnup (MCB) Code-Version 1C.*, Royal Institute of Technology, Stockholm (2000).
- [23] J. Dufek and J. E. Hoogenboom, "Numerical Stability of Existing Monte Carlo Burnup Codes in Cycle Calculations of Critical Reactors," *Nuclear Science and Engineering*, **162 (3)**, pp. 307–311 (2009).

- [24] I. Lux and L. Koblinger, *Monte Carlo Particle Transport Methods: Neutron and Photon Calculations*, CRC Press, Inc. (1991).
- [25] X.-. M. C. Team, *MCNP - A General Monte Carlo N-Particle Transport Code, Technical Report LA-UR-03-1987. Volume I: Overview and Theory*, Los Alamos National Laboratory, Los Alamos, NM (2003).
- [26] F. Brown, *A Review of Best Practices for Monte Carlo Criticality Calculations*, Los Alamos National Laboratory, Los Alamos, NM (2009).
- [27] F. B. Brown, "On the Use of Shannon Entropy of the Fission Distribution for Assessing Convergence of Monte Carlo Criticality Calculations," *Proceedings PHYSOR-2006, Vancouver, Canada, CD-ROM*, pp. (2006).
- [28] R. Sanchez and N. McCormick, "A Review of Neutron Transport Approximations," *Nuclear Science and Engineering*, **80**, pp. 481–535 (1981).
- [29] C. E. Siewert and P. Benoist, "Multigroup Transport Theory," *Nuclear Science and Engineering*, **78**, pp. 311–314 (1981).
- [30] K. Smith, *Spatial Homogenization Methods for Light Water Reactor Analysis*, Ph.D. Thesis, Massachusetts Institute of Technology (1980).
- [31] W. M. Stacey, *Nuclear Reactor Physics*, John Wiley and Sons (2001).
- [32] J. Leppänen, "Diffusion Code Group Constant Generation Using the Monte Carlo Method," *In Proc. XII Meeting on Reactor Physics Calculations in the Nordic Countries* (2005).
- [33] J. Leppänen, "A New assembly level Monte Carlo neutron transport code for reactor physics calculations," *Proceedings MC 2005 Avignon, France* (2005).
- [34] E. E. Lewis and W. F. Miller, *Computational methods of neutron transport*, American Nuclear Soc. (1993).
- [35] R. McFarlane and D. Muir, *The NJOY nuclear data processing system*, Los Alamos National Laboratory, Los Alamos, NM (1993).
- [36] R. McFarlane and A. Kahler, "Methods for Processing ENDF/B-VII with NJOY," *Nuclear Data Sheets*, **111**, pp. 2739–2890 (2010).
- [37] J. Donnelly, "Interpolation of Temperature-Dependent Nuclide Data in MCNP," *Nuclear Science and Engineering*, **168**, pp. 180–184 (2011).
- [38] A. Ivanov, V. Sanchez, and K. Ivanov, "Optimization of a coupling scheme between MCNP5 and SUBCHANFLOW for high fidelity modeling of LWR reactors," *Proc. Int. Conf. PHYSOR 2012, Knoxville, Tennessee, USA, CD-ROM* (2012).
- [39] A. Ivanov, V. Sanchez, K. Ivanov, and J. Hoogenboom, "Single pin BWR Benchmark Problem for Coupled Monte Carlo - Thermal Hydraulics Analysis," *Proc. Int. Conf. PHYSOR 2012, Knoxville, Tennessee, USA, CD-ROM* (2012).

- [40] L. D. Landau and E. M. Lifshits, *Quantum Mechanics*, Butterworth-Heinemann (1977).
- [41] W. Marshall and S. W. Lovsey, *Theory of Thermal Neutron Scattering*, Oxford (1971).
- [42] S. H. Chen and S. Yip, *Spectroscopy in Biology and Chemistry, Neutron, X-ray and Laser*, Academic Press (1974).
- [43] M. Mattes and J. Keinert, *Thermal Neutron Scattering Data for the Moderator Materials H₂O, D₂O and ZrHx in ENDF-6 Format and as ACE Library for MCNP(X) Codes*, IAEA Nuclear Data Section, Wagramer Strasse 5, A 1400 VIENNA, INDC(NDS)-0470 (2005).
- [44] F. B. Brown, *The makssf Code with Doppler Broadening*, Technical Report LA-UR-06-7002, Los Alamos National Laboratory, Los Alamos, NM (2006).
- [45] F. Brown, "Wielandt Acceleration for MCNP5 Monte Carlo Eigenvalue Calculations," *Proc. Int. Conf. PHYSOR 2007, Monterey, California*, **CD-ROM** (2007).
- [46] T. Yamamoto and Y. Miyoshi, "Reliable Method for Fission Source Convergence of Monte Carlo Criticality Calculation with Wielandt's Method," *J. Nucl. Sci. Technology*, **41**, pp. 99–107 (2004).
- [47] H. Kim and C. Kim, "Tally efficiency analysis for Monte Carlo Wielandt method," *Annals of Nuclear Energy*, **36**, pp. 1694–1701 (2009).
- [48] A. Davis and A. Turner, "Compassion of global variance reduction techniques for Monte Carlo radiation transport simulation of ITER," *Fusion Engineering and Design*, **86**, pp. 2698–2700 (2011).
- [49] A. van Wijk, G. V. der Eynde, and J. Hoogenboom, "An easy to implement global variance reduction procedure for MCNP," *Annals of Nuclear Energy*, **38**, pp. 2496–2503 (2011).
- [50] G. M. Morton, *A computer Oriented Geodetic Data Base and a New Technique in File Sequencing*, Technical Report IBM Ltd, Ottawa, Canada (1966).
- [51] Message Passing Interface Forum, "MPI: A Message-Passing Interface Standard, Version 2.2," Specification (2009).
- [52] L. Dagum and R. Menon, "OpenMP: An Industry Standard API for Shared-Memory Programming," *Computational Science & Engineering, IEEE*, **5**, 1, pp. 46–55 (1998).
- [53] J. Spanier and J. M. Gelbard, *Monte Carlo Principles and Neutron Transport Problems*, Addison-Wesley (1969).
- [54] W. Wladimirov, *Generalized functions in mathematical physics*, Moscow Nauka Publishers (1979).
- [55] F. Brown, S. Carney, B. Kiedrowski, and W. Martin, "Fission Matrix Capability for MCNP Part I - Theory," *Proceedings Mathematics and Computation, Sun Valey, Idaho, United States*, **CD-ROM**, pp. (2013).

- [56] E. L. Kaplan, "Monte Carlo Methods for Equilibrium Solutions in Neutron Multiplication," *Lawrence Livermore National Laboratory*, **UCRL-5275-T** (1958).
- [57] S. Carney, F. Brown, B. Kiedrowski, and W. Martin, "Fission Matrix Capability for MCNP Part II - Applications," *Proceedings Mathematics and Computation, Sun Valey, Idaho, United States*, **CD-ROM**, pp. (2013).
- [58] MATLAB, *version 8.3.0.532 (R2014a)*, The MathWorks Inc., Natick, Massachusetts (2014).
- [59] W. E. Arnoldi, "The principle of minimized iterations in the solution of the matrix eigenvalue problem," *Quarterly of Applied Mathematics*, **9**, pp. 17–29 (1951).
- [60] G. H. Golub and C. F. V. Loan, *Matrix computations*, Johns Hopkins University Pr. (2013).
- [61] L. N. Trefethen and D. Bau, *Numerical Linear Algebra*, Philadelphia, Pa. SIAM (1997).
- [62] R. B. Lehoucq, D. C. Sorensen, and C. Yang, "ARPACK Users Guide: Solution of Large Scale Eigenvalue Problems by Implicitly Restarted Arnoldi Methods.," 1997.
- [63] T. Kozłowski and T. Downar, "PWR MOX/UO₂ Core Transient Benchmark - Final Report," <https://www.oecd-nea.org/science/wprs/MOX-UOX-transients>, **ISBN 92-64-02330-5** (2007).
- [64] T. Kozłowski and T. Downar, "OECD/NEA and U.S. NRC PWR MOX/UO₂ Core Transient Benchmark, Working Party of the Physics of Plutonium Fuels and Innovative Fuel Cycles," https://engineering.purdue.edu/PARCS/MOX_Benchmark, **OECD/NEA Nuclear Science Committee** (2003).
- [65] C. Tippayakul, M. Avramova, F. P. Espel, and K. Ivanov, "Investigations on Monte Carlo Based Coupled Core Calculations," *Proceedings of ICAPP 2007*, **Paper 7134** (2007).
- [66] A. Kolmogorov and S.V.Fomin, *Elements of the Theory of Functions and Functional Analysis*, Graylock Press (1963).
- [67] J. Dufek and W. Gudowski, "Stochastic Approximation for Monte Carlo Calculation of Steady-State Conditions in Thermal Reactors," *Nuclear Science and Engineering*, **152**, pp. 274–283 (2006).
- [68] H. Robbins and S. Monro, "A stochastic approximation method," *Annals of Mathematical Statistics*, **22**, 3, pp. 400–407 (1951).
- [69] M. Wasan, *Stochastic approximation*, Cambridge University Press (1969).
- [70] H. Bauer, *Wahrscheinlichkeitstheorie*, Walter deGruyter (1990).
- [71] A. Ivanov, V. Sanchez, and K. Ivanov, "High-Fidelity Coupled Monte-Carlo/Thermal-Hydraulics Calculations," *Proceedings MC+SNA Paris, France 2013* (2013).

- [72] A. Ivanov, V. Sanchez, R. Stieglitz, and K. Ivanov, "Large-Scale Monte Carlo Neutron Transport Calculations with Thermal Hydraulic Feedback," *Accepted for publication, Special issue on Multi-Physics Modelling of LWR Static and Transient Behaviour, Annals of Nuclear Energy*, **84**, pp. 204–219 (2015).
- [73] J. Donnelly, "Interpolation of Temperature-Dependent Nuclide Data in MCNP," *Nuclear Science and Engineering*, **168**, pp. 180–184 (2011).
- [74] S. van der Marck, R. Meulekamp, and A. Hogenbirk, *New Temperature Interpolation in MCNP*, Proceedings of M&C 2005 conference, Avignon, France (2005).
- [75] O. Cabellos, *Processing of the JEFF-3.1 Cross Section Library into Continuous Energy Monte Carlo Radiation Transport and Criticality Data Library*, NEA-NSC-DOC 18 (2006).
- [76] A. Seubert, S. Langenbuch, and W. Zwermann, "Solution of the Stationary State of the PWR MOX/UO₂ Core Transient Benchmark," *Proceedings PHYSOR 2006, Vancouver, BC, Canada* (2006).
- [77] W. A. Rhoades and R. L. Childs, "The DORT Two-Dimensional Discrete Ordinates Transport Code," *Nuclear Science and Engineering*, **99**, pp. 88 (1988).
- [78] H. Joo, J. Cho, K. K. Lee, and S. Zee, "Methods and Performance of a Three-Dimensional Whole-Core Transport Code DeCART," *Proc. Int. Conf. PHYSOR, Chicago, Illinois, CD-ROM* (2004).
- [79] Z. Zhong, T. J. Downar, H. G. Joo, and J. Y. Cho, "Benchmark Analysis of the DeCART MOC Code with the VENUS-2 Critical Experiment," *Proc. Int. Conf. PHYSOR, Chicago, Illinois, CD-ROM* (2004).
- [80] J. Y. Cho et al., "Parallelization of Three-Dimensional Whole Core Transport Code DeCART," *Proc. Int. Conf. SNA, Paris, France, CD-ROM* (2003).
- [81] A. Travleev, R. Molitor, and V. Sanchez, "Python-based framework for coupled MC-TH reactor calculations," *Proceedings MC+SNA Paris, France 2013* (2013).
- [82] C. H. M. Broeders, *Entwicklungsarbeiten für die neutronenphysikalische Auslegung von Fortschrittlichen Druckwasserreaktoren (FDWR) mit komplexen Dreiecksgittern in hexagonalen Brennelementen*, Number KfK 5072, KfK (1992), (available in German).
- [83] T. Downar, D. Lee, Y. Xu, T. Kozlowski, and J. Staudenmier, *PARCS v2.6 U.S. NRC Core Neutronics Simulator*, School of Nuclear Engineering Purdue University (2004).
- [84] T. Nakajima and A. Takeuchi, "Verification of the Coupled 3-D Neutronics and Thermal-Hydraulic Code SKETCH-INS/TRAC-P," *Proceedings PHYSOR 2006, Vancouver, BC, Canada* (2006).
- [85] A. Ivanov, V. Sanchez, R. Stieglitz, and K. Ivanov, "Large-Scale Monte Carlo calculations with thermal-hydraulic feedback," *Proc. Int. Conf. PHYSOR 2014, Kyoto, Japan* (2014).

- [86] G. I. Bell and S. Glasstone, *Nuclear Reactor Theory*, van Nostrand Reinhold (1970).
- [87] "Numerical Stability of the Predictor-Corrector Method in Monte Carlo Burnup Calculations of Critical Reactors,".
- [88] V. I. Arnold, *Ordinary Differential Equations*, The MIT Press (1978).
- [89] H. Keller, *Numerical Methods for Two-point Boundary Value Problems*, SIAM Philadelphia (1976).
- [90] J. Lambert, *Computational Methods in Ordinary Differential Equations*, Wiley (1991).
- [91] J. Dufek, D. Kotlyar, and E. Shwageraus, "The stochastic implicit Euler method - A stable coupling scheme for Monte Carlo burnup calculations," *Annals of Nuclear Energy*, **60**, pp. 295–300 (2013).
- [92] M. Pusa and J. Leppänen, "Solving Linear Systems with Sparse Gaussian Elimination in the Chebyshev Rational Approximation Method," *Nuclear Science and Engineering*, **175**, pp. 250–258 (2013).
- [93] Z. Xu and P. Hejzlar, *MCODE, Version 2.2: An MCNP-ORIGEN Depletion Program.*, MIT-NFC-TR-104 (2008).
- [94] A. E. Isotalo, J. Leppänen, and J. Dufek, "Preventing xenon oscillations in Monte Carlo burnup calculations by enforcing equilibrium xenon distribution," *Annals of Nuclear Energy*, **60**, pp. 78–85 (2013).
- [95] D. P. Griesheimer, "In-Line Xenon Convergence Algorithm for Monte Carlo Reactor Calculations," *PHYSOR 2010. Pittsburgh, Pennsylvania, USA*, **CD-ROM** (2010).
- [96] C. H. M. Broeders and A. Ivanov, "MCBURN," *Internal KANEXT Report KIT* (2014).
- [97] C. Broeders, R. Dagan, V. Sanchez, and A. Travleev, "KAPROS-E: A Modular Program System for Nuclear Reactor Analysis, Status and Results of Selected Applications," *KTG Düsseldorf* (2004).
- [98] Y. Cao, Y. Gohar, and C. H. M. Broeders, "MCNPX Monte Carlo burnup simulations of the isotope correlation experiments in the NPP Obrigheim," *Annals of Nuclear Energy*, **37**, pp. 1321–1328 (2010).
- [99] U. Fisher and H. Wiese, "Improved and Consistent Determination of the Nuclear Inventory of Spent PWR Fuel on the Basis of Time-Dependent Cell-Calculations with KORIGEN," Report KfK 3014, 1983.
- [100] U. Fisher and H. Wiese, "KORIGEN User's Guide,".
- [101] M. Becker, *Determination of Kinetic Parameters for Monitoring Source Driven Subcritical Transmutation Devices* (2014).
- [102] E. J. Parma, *BURNCAL: A Nuclear Reactor Burnup Code Using MCNP Tallies*, Sandia National Laboratories (2012).

- [103] M. Kellett, O. Bersillon, and R. Mills, *The JEFF-3.1/-3.1.1 radioactive decay data and fission yields sub-libraries*, Bn 978-92-64-99087-6 edition, JEFF Report 20.
- [104] W. A. Alcouffe et al., "DANTSYS 3.0 - A Diffusion-Accelerated, Neutral-Particle Transport Code System," , **LA-12969-M** (1995).
- [105] N. Horelik, B. Herman, B. Forget, and K. Smith, "Benchmark for Evaluation and Validation of Reactor Simulations (BEAVRS), v1.0.1.," *Proc. Int. Conf. Mathematics and Computational Methods Applied to Nuc. Sci. & Eng.*, (2013).

